6-29-2016 12:00 AM

The Mitochondrial Calcium Uniporter Is Autoregulated by Cation Binding to the β-Grasp-Like Matrix Domain

Samuel K. Lee
The University of Western Ontario

Supervisor
Dr. Peter Stathopulos
The University of Western Ontario

Graduate Program in Physiology and Pharmacology
A thesis submitted in partial fulfillment of the requirements for the degree in Master of Science

Abstract

Mitochondrial calcium (Ca^{2+}) uptake plays fundamental roles in various signaling processes. Entry of Ca^{2+} into the mitochondrial matrix is tightly controlled by the mitochondrial Ca^{2+} uniporter (MCU) in a higher order complex regulated by inter- and intra-molecular protein-protein interactions. However, the precise mechanisms controlling MCU function and regulation remain largely unknown. I identified a well-folded N-terminal MCU region from residues 72-189, and its crystal structure revealed a β-grasp-like fold with a cluster of acidic residues that facilitates interactions with dibasic cations. Binding of Ca^{2+} or Mg^{2+} destabilize this fold and shift the protein towards monomer. Single mutants disrupting the acidic face reduced the cation sensitivity *in vitro*. Together, my data reveal that the β-grasp-like matrix region of MCU harbors a distinct acidic patch that modulates stability and protein-protein interaction equilibria in response to Mg^{2+} and Ca^{2+} binding, suggesting that these matrix cations play an important role in controlling MCU activity.

Keywords

mitochondrial calcium uniporter, calcium, crystal structure, cations, single mutants, equilibrium, beta-grasp-like fold

Co-Authorship Statement

Dr. Peter B. Stathopulos supervised and contributed to the design of all experiments discussed in this work. Dr. Murray Junop and M.C.Y. Mok performed all of the crystal mounting, diffraction, data collection, phasing and refinement in order to obtain the final crystal structures.

Acknowledgments

First and foremost, I would like to thank Dr. Peter B. Stathopulos for being a very patient and caring supervisor. I am very thankful for his dedication in investing time in all of his graduate students to help them get the best out of the graduate student experience. He has helped me learn numerous experimental techniques and helped me become a better critical thinker. All of my work would not have been possible without him.

Secondly, I would like to thank Dr. Murray Junop and M.C.Y. Mok for all of their hard work and commitment to helping me with all the crystal structure work. They have showed great patience with me and provided me with great insight in the field of crystallography. Without their help, I would not have been able to obtain the crystal structures in this project.

I would also like to thank Lee-Ann Briere from Western's biochemistry department for her patience and her help in the analytical ultracentrifugation experiments. This experiment takes a lot of time with a great deal of set up and I would just like to thank her for assisting in every process.

From the lab, I would like to thank Lisa Choi and Yue Zhao for all of their help in my project. Their assistance has allowed me to perform experiments more efficiently and effectively. Their willingness to always help me has been very encouraging and I can't thank them enough.

Lastly, I would like to thank all of my friends for all their support throughout all these years to make everything I accomplished possible. More specifically, I would like to thank all of my LFD friends for making every experience a great one. Without them, I wouldn't be the person I am today as they have helped me mature in many ways. I would of course also like to thank my family for always being there for me through both the good and the bad times. I thank them for raising me and teaching me many important things in life that I am able to take with me for the rest of my life.

Table of Contents

List of Tables

List of Figures

List of Appendices

List of Abbreviations

ADP	adenosine diphosphate
ATP	adenosine triphosphate
AUC	analytical ultracentrifugation
Å	angstrom
α	alpha
β	beta
Ca^{2+}	calcium
CC	coiled-coil
CD	circular dichroism
DNA	deoxyribonucleic acid
DTT	dithiothreitol
EMRE	essential MCU regulator
ER	endoplasmic reticulum
g	g-force
GFP	green-fluorescent protein
GnHCl	guanidine hydrochloride
HEPES	4-(2-Hydroxyethyl)-1-piperazineethanesulfonic acid
IMM	inner mitochondrial membrane
IMS	intermembrane space
IP_3	inositol 1,4,5-trisphosphate
IP_3R	inositol 1,4,5-trisphosphate receptor
K_A	equilibrium association constant
K_D	equilibrium dissociation constant
LB	Luria-Bertani
MALS	multi-angle light scattering
MCU	mitochondrial calcium uniporter
MCUb	mitochondrial calcium uniporter subunit b
MCUR1	mitochondrial calcium uniporter regulator 1

Me	metal
MEF	mouse embryo fibroblast
MICU1	mitochondrial calcium uptake 1
MICU2	mitochondrial calcium uptake 2
miR-25	micro ribonucleic acid 25
mPTP	mitochondrial permeability transition pore
MRE	mean residue ellipticity
mRNA	messenger ribonucleic acid
MW	molecular weight
MWCO	molecular weight cut off
NCX	Na^+/Ca^{2+} exchanger
Ni-NTA	nickel-nitrilotriacetic acid
OD	optical density
OMM	outer mitochondrial membrane
PCR	polymerase chain reaction
PEG	polyethylene glycol
RMSD	root mean square deviation
RNA	ribonucleic acid
Rpm	rotations per minute
SDS-PAGE	sodium dodecyl sulfate polyacrylamide gel electrophoresis
SEC	size-exclusion chromatography
Se-Met	seleno-methionine
T_m	midpoint of temperature denaturation
TM	transmembrane
TMRM	tetramethylrhodamine methyl ester
ULP5	ubiquitin-like protein
WT	wild-type
λ_{em}	emission wavelength
λ_{ex}	excitation wavelength

Chapter 1

Introduction

1.1 The general framework of cellular calcium (Ca^{2+}) regulation and signaling

In all eukaryotic cells, the Ca^{2+} concentration ($[Ca^{2+}]$) of the cytosol is tightly controlled by complex interactions among binding proteins, channels, exchangers and pumps (Rizzuto *et al.*, 2009). The cytosolic $[Ca^{2+}]$ is maintained around 100 nM in resting conditions, which is significantly lower than the extracellular $[Ca^{2+}]$ of approximately 1 mM. This is maintained by the low permeability of the plasma membrane to ions and the activity of the plasma membrane Ca^{2+}-ATPase and the Na^{+}/Ca^{2+} exchanger (NCX) (Rizzuto *et al.*, 2009). This precise regulation allows Ca^{2+} to be one of the most important second messengers in signal transduction pathways (Hajnoczky *et al.*, 2000b; Hajnoczky *et al.*, 2002).

There are two fundamental mechanisms through which intracellular $[Ca^{2+}]$ can be increased. The first involves Ca^{2+} release from intracellular stores, mainly the endoplasmic reticulum (ER) and Golgi apparatus, and the second mechanism involves the entry of Ca^{2+} from the extracellular space (Rizzuto *et al.*, 2009). Ca^{2+} release from intracellular stores is mainly induced by inositol 1,4,5-trisphosphate receptor (IP_3R), a transmembrane (TM) protein located on the ER and Golgi membrane. When extracellular soluble agonists bind a G-protein-coupled receptor, inositol 1,4,5-trisphosphate (IP_3) is produced by activation of phospholipase C (Rizzuto *et al.*, 2009). IP_3 binding to its receptor induces opening and release of Ca^{2+} from the ER and Golgi apparatus. If the opening of the IP_3R causes a depletion of ER Ca^{2+} stores, plasma membrane Ca^{2+} channels are activated and mediate Ca^{2+} entry from the extracellular space, in a process named the store-operated Ca^{2+} entry (Rizzuto *et al.*, 2009). An ER Ca^{2+}-sensing protein called stromal interaction molecule and specialized Ca^{2+} channels in the plasma membrane made up of Orai1 protein subunits have been identified in the last few years as key molecular determinants of store-operated Ca^{2+} entry (Oh-hora & Rao, 2008).

The second mechanism inducing increased intracellular Ca^{2+} involves the opening of plasma membrane Ca^{2+} channels, which are grouped into three classes: the voltage-operated Ca^{2+} channels, opened by a decrease in membrane potential (Bertolino & Llinas, 1992), the receptor-operated Ca^{2+} channels such as vanilloid receptor subtype 1, opened by capsaicin (Jambrina *et al.*, 2003), and the second messenger-operated channels, opened by the binding of a second messenger on the inner surface of the membrane (Meldolesi &

Pozzan, 1987). In the case of second messenger-operated channels, second messengers such as diacylglycerols interact with and initiate activation of the channels (Clementi & Meldolesi, 1996).

To restore resting conditions, Ca^{2+} must be rapidly removed from the cytosol once downstream targets are activated. Therefore, in addition to induced increases in intracellular Ca^{2+}, there are also Ca^{2+} extrusion mechanisms (O'Neill *et al.*, 2016; Rizzuto *et al.*, 2009; van Loon *et al.*, 2016; Wolwer *et al.*, 2016). Plasma membrane Ca^{2+}-ATPase for example, is a transport protein in the plasma membrane of cells that removes intracellular Ca^{2+} (Boczek *et al.*, 2014). This transporter is driven by the hydrolysis of adenosine triphosphate (ATP), with one Ca^{2+} removed for each molecule of ATP hydrolyzed (Oceandy *et al.*, 2007). Another example of a transporter involved in Ca^{2+} extrusion is NCX, an antiporter membrane protein that also removes intracellular Ca^{2+}. NCX uses stored energy in the electrochemical gradient of Na^{+} by allowing Na^{+} to flow down its gradient across the plasma membrane in exchange for Ca^{2+}, removing one Ca^{2+} in exchange for the import of three Na^{+} (Yu & Choi, 1997). Organelle uptake of Ca^{2+} is involved in returning Ca^{2+} levels to basal in the cytosol (Becker *et al.*, 1980; Clapham, 2007) and hence, it is important for cells to have homeostatic balance of influx and efflux of intracellular Ca^{2+} in order to function properly.

1.2 Discovery of mitochondrial Ca^{2+} uptake

Mitochondrial Ca^{2+} uptake was first measured over 50 years ago, when studies showed that mitochondria were capable of rapid Ca^{2+} uptake (Deluca & Engstrom, 1961; Rossi & Lehninger, 1964). This rapid Ca^{2+} uptake increased mitochondrial matrix Ca^{2+} concentrations by factors of 10 or more. The ability of isolated mitochondria to accumulate Ca^{2+} led to suggestions in the late 1970s that mitochondria may be involved in regulating cytosolic Ca^{2+}. It was found that if extra-mitochondrial Ca^{2+} was increased above a certain set point, mitochondria would accumulate Ca^{2+}, whereas if extra-mitochondrial Ca^{2+} was reduced below this set point, mitochondria would release Ca^{2+} via the efflux pathway (Nicholls, 1978).

Attention returned to mitochondria a couple of decades later with the development of highly specific probes that revealed microdomains of high Ca^{2+} concentrations close to the mitochondria (Hajnoczky *et al.*, 1995; Rudolf *et al.*, 2004). Mitochondria close to these microdomains of high Ca^{2+} concentration are able to rapidly take up Ca^{2+}. Therefore, it was speculated that Ca^{2+} release from the ER exposed mitochondria to much higher Ca^{2+} concentrations than what is usually present in the cytosol (Marsault *et al.*, 1997; Rizzuto *et al.*, 1993). Furthermore, mitochondria appear to be bound to the ER at designated signaling sites, allowing their close proximity and ability to use these small, locally potent (high concentration) releases of Ca^{2+} (de Brito & Scorrano, 2008). If the proximity between the ER and mitochondria are shortened, mitochondria are more prone to Ca^{2+} overload, due to their increased exposure to microdomains of high cytosolic Ca^{2+} (Dorn & Scorrano, 2010). Collectively, it is evident that mitochondria are responsible for Ca^{2+} uptake in cells and involved in the regulation of cytosolic Ca^{2+}.

1.3 Importance of mitochondrial Ca^{2+} uptake

Balanced Ca^{2+} uptake by the mitochondria is essential for cells and important for energy production, buffering and shaping cytosolic Ca^{2+} rises and also in determining cell fate by triggering or preventing apoptosis (Saris & Carafoli, 2005). Therefore, mitochondrial Ca^{2+} levels can stimulate important metabolic processes at appropriate levels. Mitochondria are known as the powerhouse of the cell and are able to produce ATP and maintain an inner membrane potential. In fact, Ca^{2+} activates three mitochondrial matrix dehydrogenases essential for ATP production (Denton, 2009), in addition to several complexes of the electron transport chain (Glancy & Balaban, 2012). The activation of the three dehydrogenases by Ca^{2+} increases nicotinamide adenine dinucleotide availability, resulting in increased flow of electrons down the respiratory chain leading to increased ATP production for the cell (Territo *et al.*, 2000). However, excessive mitochondrial Ca^{2+} can be detrimental for a cell, activating cell death pathways such as apoptosis and necrosis (Raffaello *et al.*, 2013). Mitochondria are capable of rapidly taking up Ca^{2+}, but at excessive levels, their ability to balance Ca^{2+} can be overwhelmed. When this occurs, pathological Ca^{2+} concentrations are reached and a large conductance channel known as the

mitochondrial permeability transition pore (mPTP) opens in the inner mitochondrial membrane (IMM) (Baines, 2009; Di Lisa *et al.*, 2011; Halestrap, 2009). This pore is implicated in multiple cell death pathways, including cardiac and neuronal death, hepatotoxicity, and nervous and muscular dystrophies (Hunter *et al.*, 1976). Upon mPTP opening due to mitochondrial Ca^{2+} overload, the mitochondrial membrane potential collapses which disrupts the cell's energy production mechanism, resulting in mitochondrial swelling and ultimately cell death (Juhaszova *et al.*, 2008). Opening of the mPTP may also lead to the release of caspase cofactors into the cytoplasm which triggers apoptosis (Rizzuto *et al.*, 2012). Fortunately, in cell death caused by mPTP opening, blocking of either the mPTP or the reduction of mitochondrial Ca^{2+} uptake seem to be protective, suggesting that mitochondrial Ca^{2+} uptake may be a potential target for therapeutic intervention (Baines *et al.*, 2005; Griffiths & Halestrap, 1993). Therefore, it is clear that mechanisms for altering mitochondrial Ca^{2+} levels, and maintaining homeostasis, are essential for both aerobic metabolism and cell survival.

1.4 Identification of the mitochondrial Ca^{2+} uniporter (MCU)

Although it was clear for decades that Ca^{2+} was taken up by the mitochondria and involved in the regulation of processes such as aerobic metabolism and cell death, the actual protein responsible for taking up Ca^{2+} was not identified until 2011 (Harrington & Murphy, 2015). In 2010, a mitochondrial protein that bound Ca^{2+} known as the mitochondrial Ca^{2+} uptake 1 (MICU1) was identified *in silico* in the MitoCarta database, which is an inventory of 1158 human and mouse genes encoding proteins with strong support of mitochondrial localization (Calvo *et al.*, 2016; Perocchi *et al.*, 2010). MICU1 seemed to be necessary for rapid mitochondrial Ca^{2+} uptake in intact cells and when silenced, diminished mitochondrial Ca^{2+} uptake (De Stefani *et al.*, 2011). However, it was correctly hypothesized that MICU1 was more likely to be a regulator of a uniporter rather than a core component, since it had maximally only one predicted TM domain, while a pore would need at least two (Harrington & Murphy, 2015). It was also noted that due to its two EF hands with the ability to bind Ca^{2+}, MICU1 might regulate a partner channel (Baughman *et al.*, 2011; Perocchi *et al.*, 2010).

Two groups simultaneously identified the uniporter over the next year using the MitoCarta database. Both groups identified CCDC109A, now called the mitochondrial Ca^{2+} uniporter (MCU), as a universally expressed protein that is present in mitochondria, with two TM domains that oligomerizes to form a larger complex (Baughman *et al.*, 2011; De Stefani *et al.*, 2011). In order to identify proteins that were co-expressed in proportion to MICU1, Mootha's group examined RNA and protein expression profiles (Baughman *et al.*, 2011; De Stefani *et al.*, 2011). Rizzuto's group looked in the MitoCarta database for an integral inner membrane protein that matched the criteria for being the uniporter (De Stefani *et al.*, 2011; Harrington & Murphy, 2015). Tissue expression profiling by quantitative real time polymerase chain reaction (PCR) showed ubiquitous presence in all investigated tissues with expression levels correlating with those of MICU1. (De Stefani *et al.*, 2011). To confirm their finding of MCU being the channel responsible for mitochondrial Ca^{2+} uptake, both groups further showed, in a variety of cell types, that MCU overexpression and knockdown results in increased mitochondrial Ca^{2+} and diminished mitochondrial Ca^{2+} uptake, respectively (De Stefani *et al.*, 2011; Harrington & Murphy, 2015; Kovacs-Bogdan *et al.*, 2014). Therefore, in 2011, the membrane channel MCU was identified after approximately five decades after the first characterization of mitochondrial Ca^{2+} uptake.

1.5 Localization and topology of MCU

The outer mitochondrial membrane (OMM) has channels such as the voltage-dependent anion channel, allowing Ca^{2+} to enter through the OMM (Harrington & Murphy, 2015). Localization of MCU to the IMM was confirmed by De Stefani et al., (De Stefani *et al.*, 2011) using digitonin-permeablized cells. In this experiment, green-fluorescent protein (GFP) fluorescence was visualized before and after treatment with proteinase K or Trypan blue, a fluorescence quencher that crosses the OMM, but not the IMM (De Stefani *et al.*, 2011; Giacomello *et al.*, 2010). Proteinase K had no effect on MCU-GFP fluorescence but diminished fluorescence of the cytosolic, OMM-anchored N33D1cpV probe, confirming that MCU is not on the OMM, whereas Trypan blue abrogated MCU-GFP but not mitochondrial-GFP fluorescence. Baughman et al., (Baughman *et al.*, 2011) also confirmed the localization of MCU to the IMM by disrupting the OMM by inducing hypotonic

swelling and treating the resulting mitoplasts with proteinase K (Baughman *et al.*, 2011). Proteins such as the oxidase assembly 1 that are exposed to the IMS are digested by proteinase K, whereas cytochrome oxidase II, an integral inner membrane protein, and MCU are protected, despite being targets for proteinase K (Baughman *et al.*, 2011).

Although it was established that MCU is an IMM protein with two TM domains, initial reports disagreed about its topology. Based on protease susceptibility data, Kamer et al., (Kamer *et al.*, 2014) suggested that MCU is an IMM protein with its N- and C- termini in the mitochondrial matrix and only a short linker region containing the DIME motif facing the intermembrane space (IMS). The DIME motif is a short stretch of conserved amino acids that link MCU's two TM domains (TM1 and TM2) (Baughman *et al.*, 2011). Two negatively charged residues, D and E, in this DIME motif are known to be essential for MCU function, perhaps by providing Ca^{2+} binding sites (Baughman *et al.*, 2011; De Stefani *et al.*, 2011; Lee *et al.*, 2015). They also showed that the S259A mutant of MCU (predicted to face the IMS) is resistant to the inhibitory action of the cell impermeant, Ru360 (Kamer *et al.*, 2014). On the contrary, De Stefani et al., (De Stefani *et al.*, 2011) examined the susceptibility of GFP-tagged MCU to fluorescence quenching and reported the opposite topology, stating that the N- and C- termini and most of the protein are located in the IMS (De Stefani *et al.*, 2011). Ultimately, the development and use of ascorbate peroxidase, which functions as an EM tag, indicated that the N- and C- termini are located in the mitochondrial matrix (Martell *et al.*, 2012).

Raffaello et al., (Raffaello *et al.*, 2013) performed a molecular dynamics simulation to predict the channel's quaternary structure. They developed a comparative model of the pore domain of MCU and a four-fold symmetry was imposed to the oligomer construction, as suggested by most of the available crystallographic data of other channel forming proteins. The three-dimensional averaged structure obtained from the molecular dynamics simulation of a membrane-embedded MCU model revealed the presence of a narrow selectivity filter constituted by conserved acidic residues (E257, D260, D261, E263 and E264) (Raffaello *et al.*, 2013). Subsequently, they looked for experimental confirmation of the proposed oligomeric structure and found interactions *in situ* of MCU monomers in a higher order complex (Raffaello *et al.*, 2013). *In vitro* translated MCU was separated on a

native gel, and bands at the expected molecular weight (MW) of the monomer (40 kDa) as well as at 170 kDa (reactive with a 6×-His antibody), which is compatible with a tetramer, were identified (Raffaello *et al.*, 2013). These data supported the tetrameric model of MCU assembly. Kamer et al., (Kamer *et al.*, 2014) also noted that MCU appears to oligomerize within the IMM as part of a larger MW complex. Baughman et al., (Baughman *et al.*, 2011) proposed the idea that the DIME motif appears to be critical for Ca^{2+} transport. They speculated this from the observation that mutations in this stretch of amino acids (E257A, S259A, D261A and E264A) and in the C-terminus conferred a marked resistance to both Ca^{2+} uptake and the inhibitory effect of Ru360, strongly suggesting that this is the pore-forming unit of the uniporter (Baughman *et al.*, 2011). However, despite the speculations and studies that have been done on the localization and topology of MCU, the precise structure of MCU is still largely unstudied.

1.6 MCU function in mitochondrial Ca^{2+} uptake

The mechanism by which Ca^{2+} is imported across the OMM into the IMS is through the voltage-dependent anion channel, a large, high-conductance channel and the most abundant protein of the OMM (Rizzuto *et al.*, 2009). Under resting cytosolic Ca^{2+} levels, MCU is inactive; however, upon agonist stimulation leading to increased cytosolic Ca^{2+} levels and accumulation of Ca^{2+} in the IMS, it is the role of MCU as a highly selective Ca^{2+} channel to mediate Ca^{2+} uptake into the mitochondrial matrix (Rizzuto *et al.*, 2009). Ca^{2+} from the IMS crosses the IMM through MCU by a negative potential driving force. ATP synthesis in the mitochondria establishes a large electrical membrane potential of ~-180 mV across the IMM due to proton efflux (Marchi & Pinton, 2014; Patron *et al.*, 2013) that is an attractive force for cations (Carafoli, 2003; Raffaello *et al.*, 2012). MCU-overexpressing cells show a drastic increase in the mitochondrial [Ca^{2+}] rise evoked by histamine compared to control cells and accordingly, there is a significant reduction in cytosolic [Ca^{2+}], due to increased Ca^{2+} uptake by the mitochondria (De Stefani *et al.*, 2011). Additionally, MCU-overexpressing cells show a faster rate of Ca^{2+} uptake and reach a higher mitochondrial [Ca^{2+}] plateau level (De Stefani *et al.*, 2011). MCU-expressing cells are more efficiently killed after treatment with C2-ceramide or hydrogen peroxide, thus confirming the notion

that mitochondrial Ca^{2+} loading is correlated with apoptotic signaling (Hajnoczky *et al.*, 2000a; Pinton *et al.*, 2001).

To obtain evidence of cation permeation across the pore-forming domain, De Stefani et al., (De Stefani *et al.*, 2011) mutated into glutamines two negatively charged residues of the conserved region (D260Q, E263Q) and assessed the electrophysiological properties of the mutant protein ($MCU^{D260Q,E263Q}$) produced *in vitro*. The mutant protein fails to give rise to Ca^{2+}-permeable channel activity in bilayer experiments (De Stefani *et al.*, 2011) and when the mutant is overexpressed in HeLa cells, a marked reduction in histamine-induced mitochondrial [Ca^{2+}] increases is observed compared to MCU-overexpressing and control cells. Hence, $MCU^{D260Q,E263Q}$ acts as a dominant-negative mutant, likely by inhibiting MCU channel activity within an oligomer or competing for binding sites or essential regulators (De Stefani *et al.*, 2011).

Overall, it is critical for MCU to tightly control mitochondrial Ca^{2+} uptake, as vital processes are regulated by matrix Ca^{2+} including apoptosis and energy production.

1.7 Protein regulators of MCU

1.7.1 MCUb

Following the identification of MCU, several associated regulators of MCU and a dominant-negative paralog of MCU were identified, indicating that MCU exists as a multiprotein complex with these regulators modulating its activity (Harrington & Murphy, 2015). Although the exact stoichiometry, precise role and mode of interaction with regulators are still largely unknown and under investigation, it is clear that MCU forms an ion channel as a heteromeric protein complex. This high level of regulation is consistent with the important role that mitochondrial Ca^{2+} and MCU play in cell physiology (Plovanich *et al.*, 2013).

Genomic analysis reveals a gene which translates into a 33 kDa protein known as MCUb, sharing ~50% similarity to MCU (De Stefani *et al.*, 2015). MCUb possesses two coiled-

coil (CC) domains and two TM domains separated by a short loop that slightly differs from MCU (De Stefani *et al.*, 2015). MCU and MCUb also appear to form hetero-oligomers, as *in situ* interaction of MCU and MCUb is observed and fluorescence resonance energy transfer reveals MCUb self-oligomerization (Raffaello *et al.*, 2013). Additionally, MCUb has a crucial amino acid substitution in the DIME motif at the loop region (E256V) that could have an important impact on channeling properties by removing one critical negative charge (Raffaello *et al.*, 2013).

When MCU and MCUb are co-expressed, MCU activity is significantly reduced to ~13% compared to MCU-only (Raffaello *et al.*, 2013). Therefore, MCUb subunits greatly impair Ca^{2+} permeation when incorporated into the MCU complex, acting in a dominant-negative manner (Raffaello *et al.*, 2013). In intact cells, MCUb-silencing causes a significant increase in the histamine-induced mitochondrial [Ca^{2+}] peak, and both MCUb silencing and overexpression do not alter mitochondrial tetramethylrhodamine methyl ester (TMRM) loading (Raffaello *et al.*, 2013), which is a cell-permeant, fluorescent dye sensitive to mitochondrial membrane potential.

In permeabilized cells in which mitochondrial Ca^{2+} accumulation is initiated, MCUb silencing increases the uptake rate, whereas MCU silencing significantly reduces it (Raffaello *et al.*, 2013). In the latter case, MCUb silencing does not rescue Ca^{2+} uptake (Raffaello *et al.*, 2013). An analysis of mouse tissues revealed a low level of MCUb expression that did not correlate with MCU expression. Therefore, based on the mRNA data, the MCU/MCUb ratio appears to vastly differ in various tissues, which may provide a mechanism for modulating the efficiency of mitochondrial Ca^{2+} uptake (Raffaello *et al.*, 2013).

Overall, MCUb is an endogenous dominant-negative subunit of the MCU complex that inhibits Ca^{2+} uptake activity. Furthermore, the MCU/MCUb variations among different tissues is consistent with a demonstration that the overall activity of the MCU complex is also highly variable among tissues (Fieni *et al.*, 2012).

1.7.2 MICU1 and MICU2

Early studies showed that MICU1 was required for mitochondrial Ca^{2+} uptake, as its knockdown using RNA interference largely reduced it (Perocchi *et al.*, 2010). In fact, the high resolution structure for MICU1, a 50 kDa protein consisting of four domains including two Ca^{2+}-binding EF hands, has been solved (Fig. 1.1).

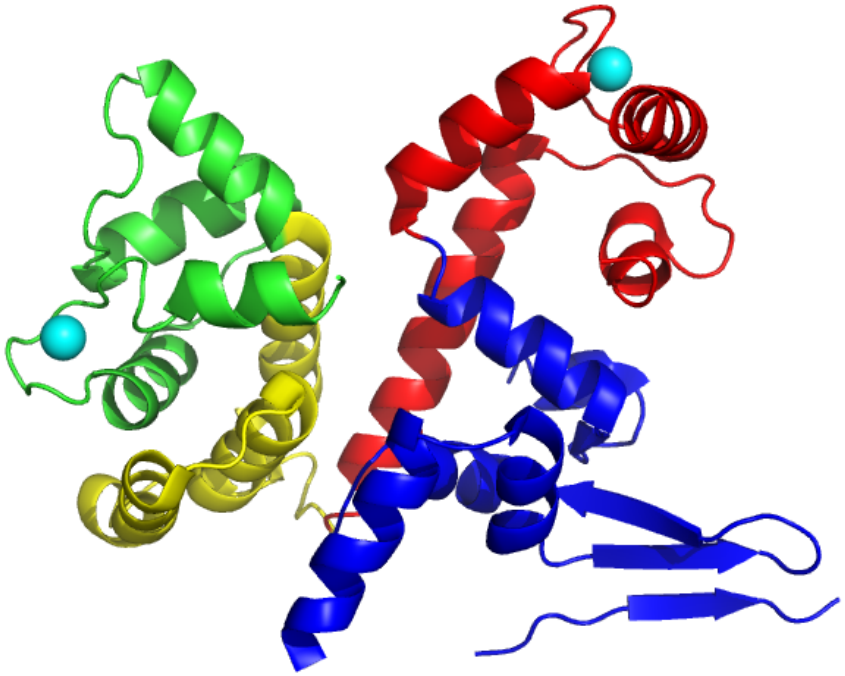

Figure 1.1. Ribbon structure of MICU1 and its domains. The structure of MICU1 was obtained from the protein data bank (4NSD) and rendered in PyMol. MICU1 consists of four different domains. Shown are ID1 in blue (residues 107-218), EF1 in red (219-315), ID2 in yellow (316-373) and EF2 in green (374-444). Ca^{2+} (cyan spheres) binding to EF1 and EF2 is also shown.

MICU2 was discovered in 2014 and is a 45 kDa paralog of MICU1 with ~27% sequence identity (Harrington & Murphy, 2015). MICU2 was first described as a protein whose silencing results in reduced mitochondrial Ca^{2+} clearance in response to large (~50 μM) extra-mitochondrial Ca^{2+} pulses (Plovanich *et al.*, 2013). However, there are conflicting perspectives on the precise role that MICU1 and MICU2 have on MCU activity. Mootha's group suggested that both MICU1 and MICU2 are negative regulators of the pore (Kamer & Mootha, 2014). Rizzuto's group proposed that MICU2 is an inhibitor and MICU1 is an activator of channel opening (Patron *et al.*, 2014).

Recently, Matesanz-Isabel's group shed some light on this discrepancy by showing that at low cytosolic [Ca^{2+}] from ~100 nM to 4.5 μM, there is a large increase in mitochondrial Ca^{2+} uptake in MICU2-silenced cells, whereas above these levels, at ~7 and 10 μM cytosolic [Ca^{2+}], the rate of mitochondrial Ca^{2+} uptake is not significantly modified by MICU2-silencing (Matesanz-Isabel *et al.*, 2016). In fact, the effect of MICU2 decreases progressively as cytosolic [Ca^{2+}] is increased. These results indicate that MICU2 acts as an inhibitor of MCU, but only at low cytosolic [Ca^{2+}] and that the regulatory effects of MICU2 disappear as the cytosolic [Ca^{2+}] is increased (Matesanz-Isabel *et al.*, 2016).

MICU1 seems to cooperate with MICU2 to keep MCU closed and set the threshold of MCU activation at low cytosolic [Ca^{2+}] (Matesanz-Isabel *et al.*, 2016). MICU1 behaves as an activator of MCU at cytosolic [Ca^{2+}] above ~2.5 μM, whereas removal of MICU2 produces no effects at cytosolic [Ca^{2+}] of ~7 μM and above. Therefore, MICU2 is a genuine inhibitor of MCU, though only at low cytosolic [Ca^{2+}], and MICU1 is inhibitory at low cytosolic [Ca^{2+}] and acts as an MCU activator at high cytosolic [Ca^{2+}] (Matesanz-Isabel *et al.*, 2016).

Although there have been speculations, the location of MICU1 and MICU2 are still unknown. Mallilankaraman et al., (Mallilankaraman *et al.*, 2012) utilized a pre-pulse protocol to load the mitochondrial matrix with Ca^{2+} to test whether MICU1 sensed Ca^{2+} in the matrix or the IMS, and concluded that MICU1 senses Ca^{2+} in the mitochondrial matrix. On the other hand, using protease sensitivity assays in isolated mitochondria or mitoplasts, several groups have concluded that MICU1 is localized in the IMS (Csordas *et al.*, 2013; Kamer & Mootha, 2014; Patron *et al.*, 2014; Wang *et al.*, 2014). However, another group image-tagged mitochondrial proteins in plasma membrane-permeabilized cells in response

to outer and inner membrane permeabilization and concluded that MICU1 behaves as if it is localized in the matrix (Hoffman *et al.*, 2013). Thus, despite the extensive studies done on MICU1 and MICU2, many unanswered questions remain on their localization and even function, limiting our full understanding of MCU regulation.

1.7.3 Essential MCU regulator (EMRE)

EMRE, discovered in 2013, is a broadly expressed 10 kDa single-pass IMM regulator with a highly conserved C-terminus rich in aspartate residues that appears to be essential to MCU function (De Stefani *et al.*, 2015; Harrington & Murphy, 2015). In both isolated mouse cells and organelles, EMRE silencing renders MCU completely ineffective and cannot be rescued by MCU overexpression (Sancak *et al.*, 2013). So far, *in vivo* reconstitution experiments using *Dictyostelium discoideum* MCU have shown that although MICU1 and MICU2 are important MCU regulators, they are not essential for MCU function, unlike EMRE (Kovacs-Bogdan *et al.*, 2014). Therefore, EMRE represents the first identified regulator essential for uniporter activity (Harrington & Murphy, 2015). Interestingly, MCU silencing results in decreased EMRE protein levels even though normal levels of EMRE mRNA are present, suggesting that EMRE loss is due to protein destabilization caused by the loss of MCU (Harrington & Murphy, 2015).

Consistent with EMRE being a core component of the MCU complex, EMRE loss results in reduced size of the complex on a native gel (Sancak *et al.*, 2013). Furthermore, co-immunoprecipitation experiments showed that the loss of EMRE specifically disrupts the association of MCU with MICU1 and MICU2. However, interactions between MCUb, MICU1 and MICU2 all appear to be dispensable for MCU-EMRE interactions since EMRE remains associated with immunoprecipitated MCU-FLAG in cells lacking MCUb or MICU1 (Sancak *et al.*, 2013).

Despite these findings, the reasons why MCU requires association with EMRE for *in vivo* Ca^{2+} conductance needs further investigation. Additional experimental work is also required to understand precisely how the activity of MCU is regulated by EMRE.

1.7.4 MCU regulator 1 (MCUR1)

MCUR1 is a 40 kDa protein with two TM domains and one CC region, with its N- and C-termini facing the IMS (Harrington & Murphy, 2015). When expressed in *Drosophila* S2R+ cells, MCUR1 markedly reduces the Ca^{2+} threshold for the mPTP opening (Chaudhuri *et al.*, 2016). On the contrary, genetic inhibition of MCUR1 makes mammalian cells resistant to Ca^{2+} overload and protects them from consequent cell death (Chaudhuri *et al.*, 2016). Although the Ca^{2+} uptake results vary, it was concluded that MCUR1 is not essential for mitochondrial Ca^{2+} transport in all species, as *Drosophila* cells display intact Ca^{2+} uptake despite an absence of an MCUR1 homolog (Mallilankaraman *et al.*, 2015). Furthermore, Ca^{2+} uptake does not change after MCUR1 overexpression in S2R+ cells or after acute/moderate inhibition in mammalian cells, despite altered Ca^{2+} sensitivity of the mPTP (Mallilankaraman *et al.*, 2015). Initially, MCUR1 was identified as an essential subunit of MCU (Mallilankaraman *et al.*, 2015), while a second report suggests that MCUR1 assists in complex assembly (Paupe *et al.*, 2015).

Although our understanding of MCU and its modulation by regulators has been evolving quickly over the past several years (Fig. 1.2), there remains many unanswered questions on precisely how the interactions with these regulators change to mediate the ON/OFF activity of MCU.

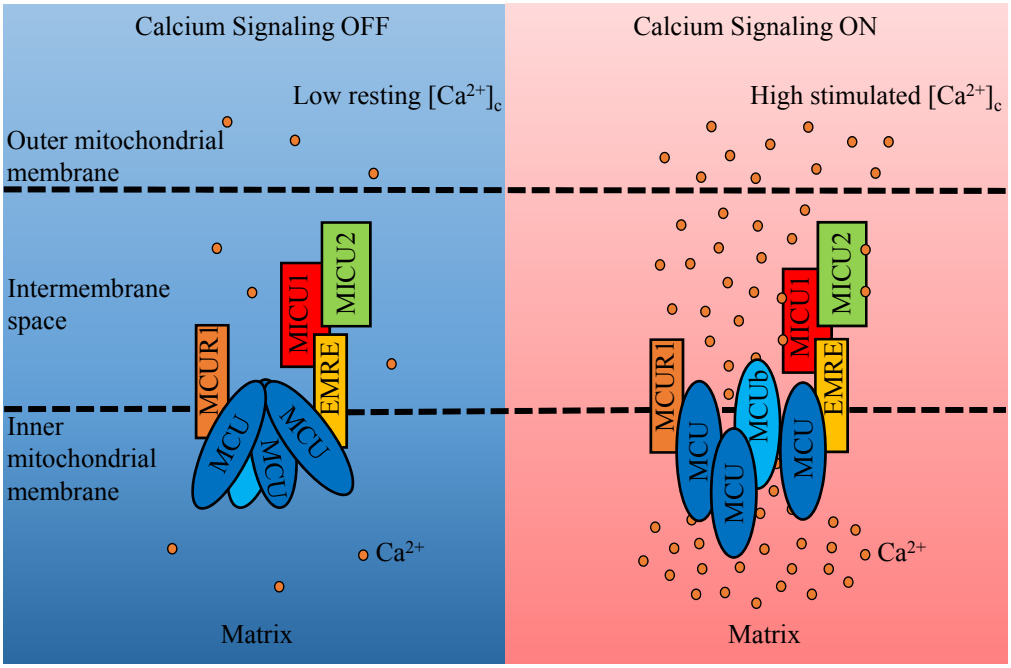

Figure 1.2. Schematic representation of the MCU complex. This schematic representation is adapted from (De Stefani *et al.*, 2015), with both low and high cytosolic [Ca^{2+}] conditions indicated (Matesanz-Isabel *et al.*, 2016). Mitochondrial Ca^{2+} uptake is controlled by a multiprotein complex composed of MCU and MCUb (the channel forming subunits) together with EMRE, MICU1, and MICU2 (other components are omitted for the sake of clarity). In resting conditions (left), Ca^{2+} signaling is off as MICU1/MICU2 heterodimers act as MCU gatekeepers, due to inhibitory effects of MICU1 and MICU2 in low [Ca^{2+}], thus preventing vicious Ca^{2+} cycles. Once Ca^{2+} signaling is activated by high [Ca^{2+}], the increase in extra-mitochondrial [Ca^{2+}] (right) induces a conformational change, with MICU1 becoming activated despite MICU2 inhibitory activity. This results in MICU1-mediated enhancement of MCU channeling activity, taking up Ca^{2+} into the mitochondrial matrix. MICU1 and MICU2 localization in the IMS is based off of my standpoint from previous studies that have been done.

1.8 MCU downregulation and knockout

Mitochondrial Ca^{2+} homeostasis participates in the control of the intrinsic pathway of apoptosis and is influenced by oncogenes, suggesting that it is involved in tumorigenesis (Clapham, 2007; Giorgi *et al.*, 2012; Pinton *et al.*, 2008; Roderick & Cook, 2008).

The identification of MCU and MICU1 has allowed molecular investigation of this process, including the regulation of their expression by microRNAs, which are a class of small (19-25 nucleotides), non-coding regulatory RNAs that modulate gene expression, causing target mRNA degradation or suppressing mRNA translation (Filipowicz *et al.*, 2008). Recently, five cancer-related microRNA families were predicted to target MCU and/or MICU1; furthermore, miR-25 was shown to cause a marked reduction in the mitochondrial $[Ca^{2+}]$ rise evoked by histamine (Marchi *et al.*, 2013). Accordingly, overexpression of an anti-miR-25 increased mitochondrial Ca^{2+} uptake induced by histamine (Marchi *et al.*, 2013). Immunoblotting showed a marked reduction in the protein level upon miR-25 overexpression and an increase in anti-miR-25-expressing cells. Marchi et al., (Marchi *et al.*, 2013) also found that miR-25-expressing HeLa cells were strongly protected from death induced by C2-ceramide and hydrogen peroxide-induced apoptotic challenges (Marchi *et al.*, 2013).

Interestingly, it has been shown that prostatic cells possess very high levels of miR-25 and are strongly sensitized to apoptosis after MCU overexpression (Marchi *et al.*, 2013). Prostate and colon cancer cell lines both demonstrate high miR-25 levels and low MCU expression levels (Marchi *et al.*, 2013). Overall, miR-25 is highly expressed in colon and prostate cancer cells, which reduces their sensitivity to apoptotic agents, highlighting MCU signaling as a novel target for cancer therapy.

MCU knockout studies have been performed in mice. The Finkel lab created $MCU^{-/-}$ mice to further elucidate the role of MCU in biologic processes (Harrington & Murphy, 2015; Pan *et al.*, 2013). Mitochondria from $MCU^{-/-}$ mice, mouse embryo fibroblasts (MEFs), and isolated adult cardiac myocytes have the inability to rapidly uptake Ca^{2+} into the mitochondria (Pan *et al.*, 2013). As expected, wild-type (WT) mitochondria are able to quickly and efficiently take up Ca^{2+}, unless treated with ruthenium red or Ru360 to inhibit

MCU, which reduces mitochondrial Ca^{2+} levels comparable to those observed in the *MCU* $^{-/-}$ mice (Pan *et al.*, 2013). Interestingly, MCU deletion has no obvious effects on aerobic respiration in the purified mitochondria from *MCU* $^{-/-}$ mice (Pan *et al.*, 2013). Furthermore, there are no detectable differences in aerobic metabolism between *MCU* $^{-/-}$ and WT MEFs using a variety of substrates (Pan *et al.*, 2013), suggesting that basal metabolism is not markedly altered in the absence of MCU expression. However, in skeletal muscle, under conditions of maximum work evaluated by an inclined treadmill test and grip strength, the *MCU*$^{-/-}$ mice have reduced abilities to generate maximal power (Pan *et al.*, 2013). Although *MCU*$^{-/-}$ mice were viable when outbred, they were born in non-Mendelian ratio, suggesting that there is some embryonic lethality (Murphy *et al.*, 2014). Additionally, *MCU*$^{-/-}$ is embryonically lethal in mice with a C57 background (Murphy *et al.*, 2014). As expected, *MCU*$^{-/-}$ mice show a significant reduction in total mitochondrial matrix Ca^{2+} (Pan *et al.*, 2013). The presence of mitochondrial Ca^{2+} in the *MCU*$^{-/-}$ mice and the non-embryonic lethality suggests that there are alternative mechanisms for Ca^{2+} entry that may compensate in the absence of MCU, such as the Letm1 Ca^{2+}/H^{+} antiporter (Jiang *et al.*, 2013).

Interestingly, when exposed to pathologic levels of Ca^{2+}, mitochondria or permeabilized MEFs from *MCU*$^{-/-}$ mice exhibit no signs of mPTP opening (Pan *et al.*, 2013). However, there is no evidence that the *MCU*$^{-/-}$ MEFs are protected from cell death, since they die as quickly and in similar numbers to WT MEFs, and the *MCU*$^{-/-}$ cells show similar levels of caspase-3 activation and mitochondrial swelling (Pan *et al.*, 2013). It is possible that the mPTP in the *MCU*$^{-/-}$ cells is activated in a Ca^{2+}-independent manner, which would be consistent with suggestions that reactive oxygen species are primary activators of mPTP *in vivo* (Lemasters *et al.*, 2009; Zorov *et al.*, 2014).

In conclusion, since the discovery of mitochondrial Ca^{2+} uptake and MCU, it is clear that the uniporter exists as a complex with multiple regulatory proteins. However, although a variety of regulators and a paralog of MCU have been identified, their exact roles and stoichiometric variance from tissue to tissue are still not fully understood. Studies on MCU downregulation and on *MCU*$^{-/-}$ mice have helped us further understand the physiological significance of MCU as a key player in mitochondrial Ca^{2+} homeostasis. Nevertheless,

understanding the mechanisms of MCU function and regulation at the molecular level is still highly lacking and needed to not only grasp the importance of the uniporter and its regulators on mitochondrial Ca^{2+} homeostasis, but more broadly on human health.

1.9 Rationale and hypothesis

Despite the realization that MCU functions as a multifaceted oligomer and the identification of a suite of proteins involved in the complex formation, an understanding of the precise atomic and molecular mechanisms of regulation is highly lacking in the field. Furthermore, while many Ca^{2+} channel proteins exhibit Ca^{2+}-dependent feedback mechanisms including IP_3Rs (Bezprozvanny *et al.*, 1991; Mak *et al.*, 1998), ryanodine receptors (Meissner *et al.*, 1986) and Ca^{2+} release-activated Ca^{2+} channels (Hoth & Penner, 1993; Zweifach & Lewis, 1995), it is unclear how dibasic cations may play a regulatory role in the function of MCU. Solving these unknown issues will not only help to gain a better understanding of mitochondrial Ca^{2+} regulation via MCU and its regulators, but will also lay the foundation to the future design of modulators of MCU activity that have a potential to treat a range of Ca^{2+}-related pathological processes.

I hypothesize that the prevalent mitochondrial matrix cations Ca^{2+} and Mg^{2+} regulate the structure and activity of MCU. Studies on the structural effects of dibasic cation binding to MCU will increase our understanding of the precise atomic and molecular mechanisms of MCU function and regulation.

Chapter 2

Materials and Methods

2.1 Cloning and mutagenesis of MCU constructs

Full length GFP-tagged MCU cDNA was graciously gifted by Muniswamy Madesh (Temple University). All primers (Sigma) used in this thesis are compiled in Table 1. With their respective primers, the sequence of interests, WT MCU construct 5 ($MCU_{105-189}$) and MCU construct 6 (MCU_{72-189}), were amplified by PCR using Thermo Phusion DNA Polymerase and Thermo Scientific 10 mM dNTP mix. PCR amplification of both constructs involved one cycle of denaturation at 98°C for 30 seconds, followed by 35 cycles of denaturation at 98°C for 10 seconds, annealing at 56°C for one minute and extension at 72°C for one minute, with a final extension at 72°C for one minute. The PCR products and pET-28a vectors encoding a 6×-His tag (Novagen) were then both digested with NheI and XhoI (New England Biolabs) overnight at 37°C, followed by gel purification of the digested products using a GenepHlow Gel/PCR Kit (GeneAid). The DNA fragments were ligated in a 20 µL reaction volume with a 3:1 ratio of insert to vector DNA by using T4 DNA ligase (New England Biolabs). Afterwards, 5 µL of each of the ligated products were then placed into an Eppendorf tube containing 100 µL of DH5α cells for transformation. The Eppendorf tubes containing the ligated products and DH5α cells were heat shocked at 42°C for 45 seconds and placed on ice for two minutes. All of the cells were then added to 900 µL of Luria-Bertani (LB) in a falcon tube and incubated with constant shaking at 37°C for 90 minutes. The cells were then centrifuged down and resuspended with 150 µL of LB medium and plated on kanamycin-containing agar plates to be incubated overnight at 37°C.

To ensure the ligated products were in the bacteria, colony PCR was performed with 2× Taq Frogga Mix along with T7 forward and T7 reverse primers. After setting up 15 Eppendorf tubes with colonies resuspended in autoclaved H_2O and running PCR under the same conditions as above, agarose gel electrophoresis was performed followed by staining with ethidium bromide to identify colonies harboring the expected insert size. Positive colonies were grown overnight in 5 mL LB + kanamycin and incubated overnight at 37°C. The final kanamycin concentrations in all cloning, expression and purification procedures were 60 µg mL^{-1}. Plasmid mini-preparation was then performed to isolate the plasmid DNA using a Presto Mini Plasmid Kit (GeneAid), following the protocol as described by the manufacturer. DNA sequencing was then performed at the DNA Sequencing Facility of the

Robarts Research Institute (London, Ontario) to confirm the insert sequences, with sequencing reactions prepared according to their guidelines using T7 forward or reverse primers.

The MCU_{72-189} I141M/L146M, MCU_{72-189} D131R and MCU_{72-189} D147R mutations were each generated by QuikChange site-directed mutagenesis (Stratagene). Mutagenic primers (Table 1) were used to amplify the entire pET-28a vectors that contained the MCU_{72-189} WT template inserts. The PCR for mutagenesis involved one cycle of denaturation at 98°C for 30 seconds, followed by 35 cycles of denaturation at 98°C for 10 seconds, annealing at 56°C for 30 seconds and extension at 72°C for three minutes, with a final extension at 72°C for five minutes. DpnI was used to digest the methylated template DNA for two hours at 37°C. The PCR amplification products were then transformed into DH5α cells. Plasmids from the resultant colonies were propagated and purified by plasmid mini-preparation as described above. Mutations were confirmed by DNA sequencing, as described above.

Table 1 Primers used in this thesis. Underlined sequences indicate NheI restriction sites (GCTAGC) and XhoI restriction sites (CTCGAG). All primers are shown in the 5' to 3' direction.

Primer	Sequence
MCU5 S105 Sense	ACACTCAAGGCTAGCTCTGACTCGTTGGTGTATTTTTACG
MCU6 S72 Sense	GCAGCACTGTTGCTAGCTCTGATGATGTTACAGTGG
MCU6 T189 Antisense	GTTTAACTGGTGCTGCTCCTCGAGCTATGTGGTGTATAGTTG
MCU6 I141M/L146M Antisense	GCTGCTTCAACAGGAATGGACCTCCTCCTCATGGATGACTTTAAGCTG
MCU6 I141M/L146M Antisense	CAGCTTAAAGTCATCCATGAGGAGGAGGTCCATTCCTGTTGAAGCAGC
MCU6 D131R Sense	GCTATCTATTCACCACGTGGTGTTCGCGTTGCTGC
MCU6 D131R Antisense	GCAGCAACGCGAACACCACGTGGTGAATAGATAGC
MCU6 D147R Sense	GACCTCCTCCTCCTTCGTGACTTTAAGCTGGTC
MCU6 D147R Antisense	GACCAGCTTAAAGTCACGAAGGAGGAGGAGGTC

2.2 Expression and purification of MCU constructs

WT $MCU_{105-189}$ and WT, D131R, or D147R MCU_{72-189} pET-28a constructs were all transformed in BL21 (DE3) codon + *Escherichia coli*. First, 1.25 µL of DNA for each construct were added into 100 µL of BL21 (DE3) codon + *Escherichia coli* and incubated on ice for 45 minutes. The cells were then heat shocked at 42°C for 45 seconds, and placed on ice for two minutes. The cells were then added to 900 µL of LB in a falcon tube and incubated for 60 minutes at 37°C and ~200 rotations per minute (rpm). Next, 100 µL of the cells were then spread onto kanamycin-containing agar plates and incubated overnight at 37°C. The next day, a single colony was inoculated in 25 mL of LB medium containing kanamycin and grown overnight at 37°C. The next day, this starter culture was equally divided into two larger flasks containing 500 mL of LB each, supplemented with kanamycin. The cells were grown at 37°C to an OD_{600nm} of ~0.6-0.8, and 200 µM of isopropyl β-D-1-thiogalactopyranoside was added to induce expression over a 16 hour period at 22°C. Cells were harvested using a centrifuge (Beckman Model J2-21M) at 9,300× *g* for 25 minutes at 8°C. Harvested cells were then stored at -20°C in conical tubes until purification.

The I141M/L146M MCU_{72-189} construct was used for seleno-methionine (Se-Met) incorporation. Transformation and starter cultures were prepared as described above. For Se-Met incorporation, cells were large scale cultured in M9 medium supplemented with kanamycin. First, 1 L of M9 salt solution was prepared by adding 41.4 mM anhydrous Na_2HPO_4, 22.0 mM KH_2PO_4 and 8.6 mM NaCl filled up to 1 L of nanowater with a pH of 7.4. The large flask with the M9 salt solution was then autoclaved. Once the flasks were cooled down, the following additives were then filtered through a 0.22 µm syringe into the M9 salt solution: 11.1 mM D-glucose, 18.7 mM NH_4Cl, 0.1 mM thiamine, 4.1 µM biotin, 0.1 mM $CaCl_2$ and 0.1 mM $MgSO_4$.

Starter culture cells were centrifuged (Thermo Scientific Sorvall ST 16R centrifuge) at 2,400× *g* for 15 minutes at 8°C and the LB medium was decanted. The cell pellet was resuspended in ~10-15 mL of the M9 medium supplemented with kanamycin and transferred into the 1 L M9 medium for growth. Cells were incubated with constant shaking at ~180 rpm at 37°C to an OD_{600nm} of ~0.6-0.8. Subsequently, the following amino acids

were added to inhibit methionine biosynthesis: 0.6 mM phenylalanine, 0.7 mM lysine, 0.8 mM threonine, 0.4 mM leucine, 0.4 mM isoleucine and 0.4 mM valine. This was followed by the addition of 0.3 mM Se-Met for incorporation. After 15 minutes of incubation at 37°C and ~180 rpm, the medium and cells were split evenly into two 2 L flasks (i.e. 500 mL in each) and 200 μM isopropyl β-D-1-thiogalactopyranoside was added to induce expression over a 16 hour period at 22°C. Cells were harvested and stored for purification as described above.

For purification, frozen MCU_{72-189} cell pellets were lysed and denatured with 6 M guanidine hydrochloride (GnHCl), 20 mM Tris (pH 8.8) and 5 mM 2-Mercaptoethanol, whereas $MCU_{105-189}$ was denatured with 6 M GnHCl and 20 mM Tris (pH 8). Cell pellets were well homogenized by mechanical agitation using a transfer pipette. Cell suspensions were subsequently placed in a rotating hybridization oven for 90 minutes at ambient temperature. Lysates were clarified by centrifugation (Thermo Scientific Sorvall ST 16R centrifuge) at 10,000× *g* for 30 minutes at 8°C. Approximately 1.5 mL of a ~30% (v/v) slurry of Ni-nitriloacetic acid (Ni-NTA) agarose resin (Qiagen) was added to the clarified supernatant (~40 mL) and incubated for 90 minutes on the rotating hybridization oven. The Ni-NTA resin was subsequently captured on a column and the flow-through was disposed. The resin was washed with 3× 10 mL volumes of wash buffer containing 6 M urea, 20 mM Tris (pH 8.8) and 5 mM 2-Mercaptoethanol for MCU_{72-189} constructs, whereas for $MCU_{105-189}$ constructs, the column was washed with 3× 10 mL volumes of wash buffer containing 6 M urea and 20 mM Tris (pH 8). The 6×-His tagged MCU_{72-189} bound to the resin was eluted with seven fractions of 2 mL elution buffer containing 6 M urea, 300 mM imidazole, 20 mM Tris (pH 8.8) and 5 mM 2-Mercaptoethanol, whereas the 6×-His tagged $MCU_{105-189}$ was eluted with 6 M urea, 300 mM imidazole and 20 mM Tris (pH 8). Each of the seven fractions were collected 2 mL at a time with an incubation time of two minutes. Afterwards, 17.5 μL aliquots of the elution fractions prepared in Laemmli sample loading dye were individually assessed by denaturing sodium dodecyl sulfate polyacrylamide gel electrophoresis (SDS-PAGE) in 15% (v/v) acrylamide gels, which were run at 195 volts (V) for 55 minutes.

The gels were then Coomassie blue stained for 20 minutes, followed by destaining for 20 minutes. The destained gels were visualized under a white light transilluminator (VWR Scientific) to check the presence of the protein bands at its corresponding MW at high purity, as shown in Figure 2.1A.

The MCU_{72-189} eluted fractions (i.e. ~14 mL) were refolded by dialysis using a 3,500 molecular weight cut off (MWCO) membrane (BioDesignDialysis Tubing) overnight in 1 L of buffer containing 20 mM Tris (pH 8.8), 150 mM NaCl and 1 mM dithiothreitol (DTT), whereas the eluted $MCU_{105-189}$ fractions were dialyzed overnight in refolding buffer containing 20 mM Tris (pH 8) and 150 mM NaCl. The 6×-His tags were subsequently cleaved by adding ~1 U mg^{-1} thrombin (BioPharm) to the dialysis bags and dialyzed in buffer containing 20 mM 4-(2-Hydroxyethyl)-1-piperazineethanesulfonic acid (HEPES) (pH 8.5), 150 mM NaCl and 1 mM DTT for ~24 hours. $MCU_{105-189}$ 6×-His tags were cleaved in dialysis buffer containing 20 mM Tris (pH 7.5) and 150 mM NaCl for ~24 hours. Thrombin cleavage efficiency was checked by SDS-PAGE as described above. The gels were then stained in Coomassie blue stain and destained for 20 minutes each and visualized under white light using the transilluminator (VMR Scientific) (Figure 2.1B).

After thrombin digestion, proteins were further purified by 5 mL HiTrap Q (GE Healthcare) anion exchange chromatography (GE Healthcare). All proteins were concentrated to ~1.5 mL using an Amicon Ultra-15 10 K (Millipore) and were negatively charged at the loading buffer pH to bind to the positively charged column resin. The pI of MCU_{72-189} and $MCU_{105-189}$ with bound 6×-His tag are 7.30 and 6.79 respectively, whereas the pI of the MCU_{72-189} D131R and D147R mutants with bound 6×-His tag are both 8.27. Without bound 6×-His tag, the pI of MCU_{72-189} and $MCU_{105-189}$ are 6.30 and 5.38 respectively, whereas the pI of the MCU_{72-189} D131R and D147R mutants are both 7.47. The loading buffer for the MCU_{72-189} construct was 20 mM HEPES (pH 8.5) and 1 mM DTT, whereas the loading buffer for the $MCU_{105-189}$ constructs was 20 mM Tris (pH 7.5). To elute the proteins of interest, a high salt buffer containing 20 mM HEPES (pH 8.5), 1 M NaCl and 1 mM DTT for MCU_{72-189} constructs and 20 mM Tris (pH 7.5) and 1 M NaCl for $MCU_{105-189}$ constructs was used. All buffers were filtered and degassed. By increasing the salt concentration using a linear salt gradient from 0-60%, the molecules with the weakest ionic interactions were

eluted from the column first, while those with stronger ionic interactions require a higher salt concentration and elute later in the gradient. All fractions were eluted at a flow rate of 1 mL min^{-1} and collected in Eppendorf tubes in 1.5 mL fractions. All fractions were run on SDS-PAGE as described above to assess the purity of the fractions and confirm the identity of the proteins of interest (Figure 2.1C).

Once proteins were confirmed to be present and high in purity, the appropriate fractions were collected together and placed in 3,500 MWCO dialysis tubing (BioDesignDialysis Tubing). All proteins were dialyzed overnight in a final buffer containing 20 mM HEPES (pH 7.5), 150 mM KCl and 2 mM DTT which were used in all experiments unless otherwise stated. Once dialyzed, proteins were concentrated using an Amicon Ultra-15 10 K (Millipore) to its appropriate concentration and stored at 4°C.

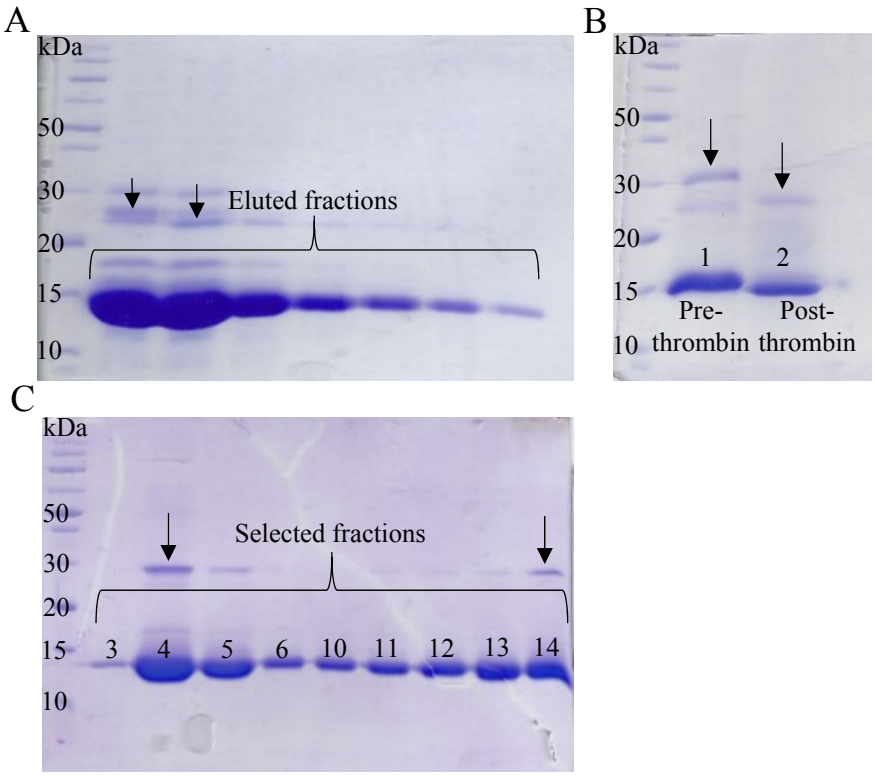

Figure 2.1. SDS-PAGE gels of MCU_{72-189}. (A) SDS-PAGE gel of eluted MCU_{72-189} protein with 6×-His tag purification fractions. MCU_{72-189} with 6×-His tag bands are seen at its approximate corresponding MW of 15.8 kDa as calculated by Protein Calculator v3.4. Darker bands indicate high amounts of protein, whereas lighter bands above the corresponding MW indicate contaminants or oligomers. Protein eluted from the Ni-NTA beads are estimated to have a purity >90%, as visualized by the intensity of the protein bands and a small presence of contaminant or oligomerized MCU_{72-189} bands (arrows). **(B)** SDS-PAGE gel assessment of MCU_{72-189} thrombin cutting efficiency of 6×-His tag. Sufficient thrombin cleaving of 6×-His tag is shown, with a band at approximately 15.8 kDa pre-thrombin (1), and a band at approximately 13.9 kDa post-thrombin (2), which is the expected MW of MCU_{72-189} without the 6×-His tag, as calculated by Protein Calculator v3.4. Less intense bands above the corresponding MW indicate contaminants or oligomers of MCU_{72-189} (arrows). **(C)** SDS-PAGE gel of MCU_{72-189} anion exchange chromatography elution fractions. The selected Eppendorf tube fractions show protein bands with strong intensity at approximately 13.9 kDa, which is the MW of MCU_{72-189} without the 6×-His tag, as calculated by Protein Calculator v3.4. Less intense bands above the corresponding MW indicate contaminants or oligomers (arrows). However, the protein is highly pure (>90%), allowing for further experiments. Note that selected fractions in between 3-14 not shown on the gel were also used for experiments.

2.3 Mass spectrometry of MCU_{72-189}

The final dialyzed MCU_{72-189} was diluted to 0.5 mg mL^{-1} with 25 mM ammonium bicarbonate with a total volume of 100 µL. A 7,000 MWCO Zeba Spin Desalting Column (Thermo Scientific) was centrifuged at 1,500× *g* for one minute at 8°C (Thermo Scientific Sorvall Micro 21R Centrifuge). The column was then washed with 300 µL of ammonium bicarbonate three times for one minute each. After washing, 85 µL of the protein sample was added to the column and placed in a sterile Eppendorf tube. The sample was then eluted (Thermo Scientific Sorvall Micro 21R Centrifuge) at 1,500× *g* for two minutes at 8°C. The prepared sample was then sent to the Biological Mass Spectrometry Laboratory (Western University, London, ON) for electrospray ionization mass spectrometry to confirm the identity of the protein obtained after the final purification step (Figure 2.2). This was performed by the technician (Paula Pittock) on a Q-Tof Micro Mass spectrometer (Waters) equipped with a Z-spray source and run in positive ion mode. The MS survey data range was 600-1800 with a cone voltage of 25 V and a source temperature of 80°C. Calibration was performed with myoglobin with a mass error of 0.5 Da and the acquisition software was MassLynx 4.1 (Waters).

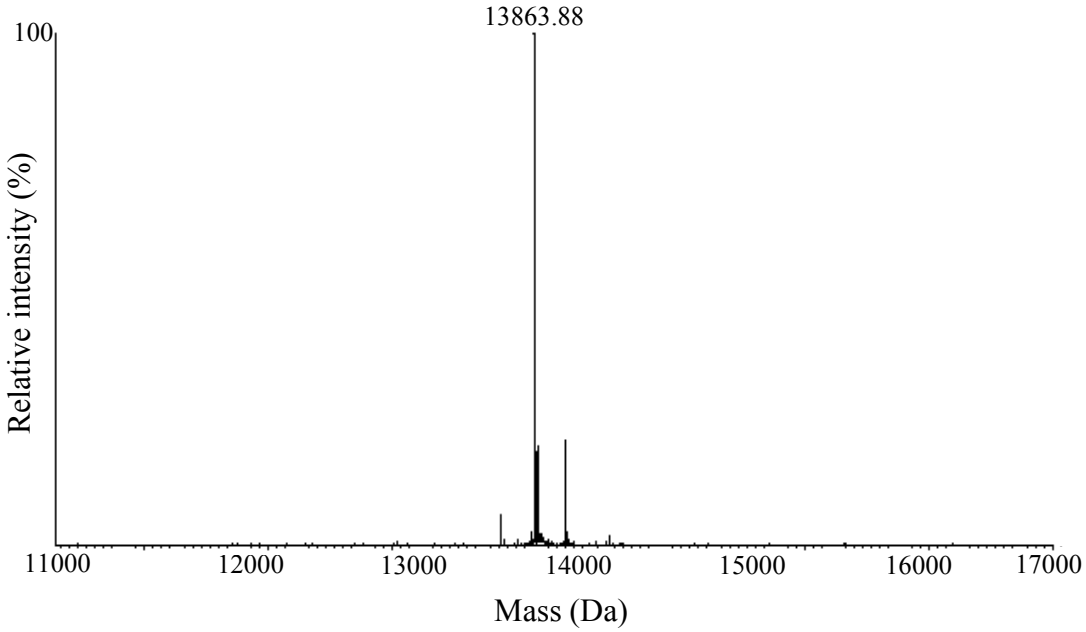

Figure 2.2. Mass spectrometry data of MCU_{72-189}. X-axis represents the MW in Da and the Y-axis represents the relative intensity (%). The MW weight shown at 13863.88 Da essentially matches the theoretical MW of MCU_{72-189} of 13863.73 Da, confirming the presence of the protein to carry on with experiments knowing the protein of interest is present. The other peaks may represent contaminants or protein fragments.

2.4 Crystallization of MCU_{72-189} constructs

All crystals were grown at 18°C using the hanging-drop vapor diffusion method with 24-well crystallization plates (Nextal). Purified protein in 20 mM HEPES (pH 7.5), 150 mM KCl and 2 mM DTT were concentrated to ~4.5 mg mL^{-1} using Amicon Ultra-15 10 K. Crystallization of MCU_{72-189} was initially screened by mixing 1 µL of protein (2.84 mg mL^{-1}) with 1 µL of precipitant using Heavy and Light Twin Pack, Wiz I and II and Pact Premier kits, equilibrated against 500 µL of 1.5 M $(NH_4)_2SO_4$. Further optimization was performed with the conditions that gave crystals, testing varying protein to precipitant ratios ranging from 1:1 to 3:1, equilibrated against varying concentrations of $(NH_4)_2SO_4$, ranging from 1.1 M to 1.7 M. For this further optimization process, there were 96 different conditions performed, followed by an additional 72 conditions for further optimization.

Ultimately, apo native MCU_{72-189} was crystallized by mixing 1 µL of protein with 1 µL of precipitant (0.2 M $LiSO_4$, 0.1 M imidazole, 10% polyethylene glycol (PEG) 3000, pH 8.0) and equilibrated against 500 µL of 1.5 M $(NH_4)_2SO_4$. Native MCU_{72-189} was also crystallized in a similar manner using 0.32 M $MgCl_2$, 0.1 M Tris (pH 8.5), 24% PEG 400 equilibrated against 500 µL of 1.6 M $(NH_4)_2SO_4$ or 0.2 M calcium acetate, 0.1 M imidazole, 10% PEG 8000, pH 8.0 equilibrated against 500 µL of 1.3 M $(NH_4)_2SO_4$. The Se-Met derivatized I141M/L146M MCU_{72-189} mutant was crystallized under the same conditions as the native in the presence of $MgCl_2$. Crystals were grown for three days to an average size of 300 × 50 × 50 μm^3, and the subsequent crystal mounting, diffraction, data collection, phasing and refinement were graciously performed by the Junop laboratory. Single-wavelength anomalous diffraction for Se-Met derivatized I141M/L146M and native datasets for MCU_{72-189} were collected at a wavelength of 0.979 Å under cryogenic conditions (100 K) at the Canadian Light Source CMCF08ID beamline. Data were processed using iMosflm (Battye *et al.*, 2011). For Se-Met derivatized I141M/L146M MCU_{72-189}, Phenix was used to locate the Se sites, phasing, density modification and model building (Adams *et al.*, 2010). For all native datasets, the structures were determined by molecular replacement using the I141M/L146M structure as a search model in Phenix (Adams *et al.*, 2010). Refinement of mutant Se-Met and native MCU structures were carried out utilizing multiple interactions of Coot and Phenix-Refine until R and R_{free} values

converged and geometry statistics reached suitable ranges (Adams *et al.*, 2010; Emsley *et al.*, 2010). The final model for Se-Met derivatized I141M/L146M MCU_{72-189} omitted several residues due to disorder, including: residues 72 and 168-189. The same residues were also missing in the native MCU_{72-189} structures. All crystal structures shown in the figures were rendered in PyMOL.

2.5 Far-UV circular dichroism (CD) spectroscopy

Protein secondary structure was assessed by far-UV CD spectroscopy, which measures the differences in the absorption of left-handed circularly polarised light and right-handed circularly polarised light of the protein. CD spectra were acquired on a Jasco J-810 spectropolarimeter equipped with a Peltier temperature control system (Biomolecular Interactions and Conformations Facility, Western University, London, ON) using a quartz cell with a path length of 0.1 cm. Each spectrum was taken at 4°C with an average of three scans acquired between 200 and 250 nm (unless otherwise stated) at a speed of 20 nm min^{-1}, data pitch of 1 nm and a response time of 8 seconds. CD spectra were corrected for buffer contributions and values were converted to mean residue ellipticity (MRE). All CD experiments were done using a protein concentration of 0.5 mg mL^{-1} unless stated otherwise.

Thermal melts were acquired by monitoring the change in CD ellipticity at 222 nm while heating the samples from 5-90°C at a rate of 1°C min^{-1}. The thermal melt data pitch was 1°C using a response time of 8 seconds. Data points from the melting curves were normalized from 0 to 1 and the apparent temperatures where the fractional change in ellipticity was approximately 0.5 (T_m) were extracted as an indicator of stability. Thermal melts were acquired using a protein concentration of 0.5 mg mL^{-1} unless stated otherwise.

2.6 Size exclusion chromatography with in-line multi-angle light scattering (SEC-MALS)

SEC was performed on a Superdex 200 Increase 10/300 GL column linked to an AKTA pure fast protein liquid chromatography system (GE Healthcare) housed at 4°C. MALS measurements were performed in-line with the SEC using a 16-angle Dawn Heleos II light-scattering instrument equipped with a 662-nm laser (Wyatt Technologies). Protein concentrations through the eluted peaks were measured with an in-line Optilab T-rEX differential refractometer (Wyatt Technologies) with a 658-nm laser and a refractive index increment of $dn \cdot dc^{-1} = 0.185\ mL \cdot g^{-1}$. For this experiment, proteins were dialyzed in a final buffer containing 20 mM HEPES (pH 7.5), 150 mM KCl and 0.5 mM DTT. The running buffer for the Ca^{2+}-free experiment was 20 mM HEPES (pH 7.5), 150 mM KCl and 0.5 mM DTT, whereas the running buffer for the Ca^{2+}-loaded experiments was 20 mM HEPES (pH 7.5), 150 mM KCl, 40 mM $CaCl_2$ and 0.5 mM DTT. All protein concentrations used for this experiment were 2.0 mg mL^{-1}. Three repetitions for both Ca^{2+}-free and Ca^{2+}-loaded experiments for each protein were performed. Samples were eluted at a flow rate of 0.35 mL min^{-1} and molecular weights were calculated using the ASTRA software v6.1.5.22 (Wyatt Technologies).

2.7 Analytical ultracentrifugation (AUC) sedimentation equilibrium

Sedimentation equilibrium studies were carried out using a Beckman Optima XL-A Analytical Ultracentrifuge (Biomolecular Interactions and Conformations Facility, Western University) at 25°C. Final dialyzed $MCU_{72\text{-}189}$ was concentrated to a minimum of 1.2 mg mL^{-1}. AUC was performed with three concentrations (1.2 mg mL^{-1}, 0.8 mg mL^{-1}, 0.4 mg mL^{-1}) in both Ca^{2+}-free and Ca^{2+}-loaded states. An An60Ti rotor and six-channel cells with Epon-charcoal centerpieces were used. For loading, 125 µL of the sample buffers and 110 µL of samples with different protein concentrations were pipetted into the channel centerpieces. Absorbance measurements at 280 nm were collected in 0.002 cm radial steps and averaged over 10 readings. The densities of solvents were calculated from published tables (Rissato *et al.*, 2005; Yurdakok-Dikmen *et al.*, 2016).

Data were analyzed using the global single ideal species model defined as:

$$c_r = c_o \exp\left[\frac{\omega^2}{2RT} M_{obs}\,(1 - \bar{\nu}\,\rho)(r^2 - r_0^2)\right] + I_o$$

where c_r is the concentration at radius r, c_o is the concentration at reference radius r_o, ω is the angular velocity of the rotor, M_{obs} is the molecular weight of the protein, $\bar{\nu}$ is the partial specific volume of $MCU_{72\text{-}189}$, calculated from its amino acid composition as 0.738 mL g^{-1}, ρ is the density of the solvent, R is the ideal gas constant, T is the temperature in Kelvins, and I_o is the baseline offset. Data were also analyzed according to a monomer-dimer equilibrium model defined as:

$$c_r = c_o \exp\left\{\left[\frac{\omega^2}{2RT} M_m\,(1 - \bar{\nu}\,\rho)(r^2 - r_0^2)\right]\right\} + \left\{c_o^n\, K_A exp\left[\frac{\omega^2}{2RT} n M_m\,(1 - \bar{\nu}\,\rho)(r^2 - r_0^2)\right]\right\} + I_o$$

Where K_A is the equilibrium association constant, M_m is the theoretical mass of the monomer, and other terms are defined as above. All data fitting was done using Graphpad Prism 5.

2.8 Ca^{2+} and Mg^{2+} binding estimates by intrinsic fluorescence

Changes in intrinsic fluorescence of $MCU_{72\text{-}189}$ as a function of $CaCl_2$ or $MgCl_2$ concentrations were taken as an estimate of binding affinity. Experiments were performed using a Cary Eclipse Fluorescence Spectrophotometer with an excitation wavelength (λ_{ex}) of 280 nm and excitation and emission slit widths of 5 and 10 nm, respectively. The photomultiplier was set at a voltage of 650 V. Emission spectra were acquired between 290 to 350 nm on 0.5 mg mL^{-1} samples placed in a 1.0 cm path length quartz cuvette and equilibrated at 25°C. Increasing concentrations of $CaCl_2$ or $MgCl_2$ from 0 mM to 10 mM were added to the samples to measure the change in relative fluorescence intensity. A similar molar concentration of free Tyr in solution showed nominal changes in fluorescence up to 17 mM $CaCl_2$. Binding curves were fit to a one-site binding model taking into account protein concentration by non-linear regression defined as:

(1) $\mathrm{P} + \mathrm{Me} \overset{K_D}{\leftrightarrow} \mathrm{PMe}$

(2) $F_{bound} = \frac{1}{2}\left(K_D + P_{tot} + Me - \sqrt{(K_D + P_{tot} + Me)^2 - 4\,P_{tot} \cdot Me}\right)$

(3) $F_{free} = 1 - F_{bound}$

(4) $Y_{obs} = I_o \cdot F_{free} + I_{sat} \cdot F_{bound}$

Where P is the protein, Me is the metal, F_{bound} is the fraction of bound protein, F_{free} is the fraction of free protein, P_{tot} is the total protein, Y_{obs} is the observed signal, I_o is the initial signal, and I_{sat} is the saturated signal. All data fitting was done using Graphpad Prism 4.

2.9 Chemical denaturation curves

Equilibrium denaturation curves were obtained for $MCU_{72\text{-}189}$ by diluting the concentrated stock protein to 5 μM in increasing GnHCl concentrations. Samples were equilibrated at 20°C for 90 minutes using a temperature-controlled water bath incubation (Lauda Brinkmann Ecoline RE 120). Intrinsic fluorescence measurements were done using the Cary Eclipse Fluorescence Spectrophotometer. An λ_{ex} of 275 nm and emission wavelength (λ_{em}) of 305 nm were used with excitation and emission slit widths set to 5 and 20 nm, respectively. Fluorescence from samples placed in 1.0 cm path length quartz cuvettes were averaged over 60 seconds for each point.

Chapter 3

Results

3.1 MCU contains a conserved β-grasp-like matrix domain

Human MCU is a ~40 kDa protein that is made up of 351 amino acids (NCBI, Q8NE86) (Fig. 3.1). MCU contains a mitochondrial signal peptide localized in the first 49 N-terminal residues (Emanuelsson *et al.*, 2000), as well as two predicted TM domains (TM1, residues 234-256; TM2, residues 266-283) near the C-terminal region (Krogh *et al.*, 2001; Sonnhammer *et al.*, 1998). Additionally, prior to TM1 and after TM2, two putative CC domains can be identified, adjacent to the C-terminus (Lupas, 1997; Lupas *et al.*, 1991). Electron micrographic immune-labeling studies suggest that both the N- and C- termini, which comprise a large portion of the soluble regions and the overall majority of the protein, are localized within the matrix (Martell *et al.*, 2012). To identify a well-folded domain and structural target within the matrix-oriented region of MCU, I performed a multiple sequence alignment of roundworm, fruit fly, fish, human and mouse sequences (Fig. 3.2) (Sievers & Higgins, 2014). Based on the conserved sequence among these species outside the putative TM and CC domains, I cloned a construct encompassing residues 72 to 189 (i.e. $MCU_{72\text{-}189}$). Far-UV circular dichroism (CD) spectroscopy was used to assess the secondary structure and showed that $MCU_{72\text{-}189}$ is comprised of an α-helix/β-strand mixture (Fig. 3.3A). An assessment of stability was made by monitoring the change in CD signal at 222 nm as a function of temperature. This thermal melt showed that $MCU_{72\text{-}189}$ cooperatively unfolds with a midpoint of temperature denaturation (T_m) above 60°C (Fig. 3.3B), indicating a stably folded domain.

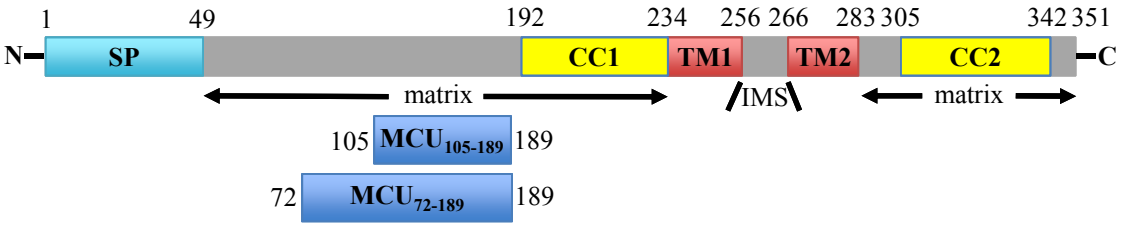

Figure 3.1. Domain architecture and structural features of MCU. Domain architecture of human MCU (NCBI, Q8NE86). Residue ranges and the prevailing topology are indicated at top. Signal peptide (SP, teal), transmembrane domain (TM1, TM2, red) and coiled-coil domain (CC1, CC2, yellow) were predicted bioinformatically (Emanuelsson *et al.*, 2000; Krogh *et al.*, 2001; Lupas, 1997). $MCU_{105-189}$ and MCU_{72-189} constructs studied herein are indicated (blue).

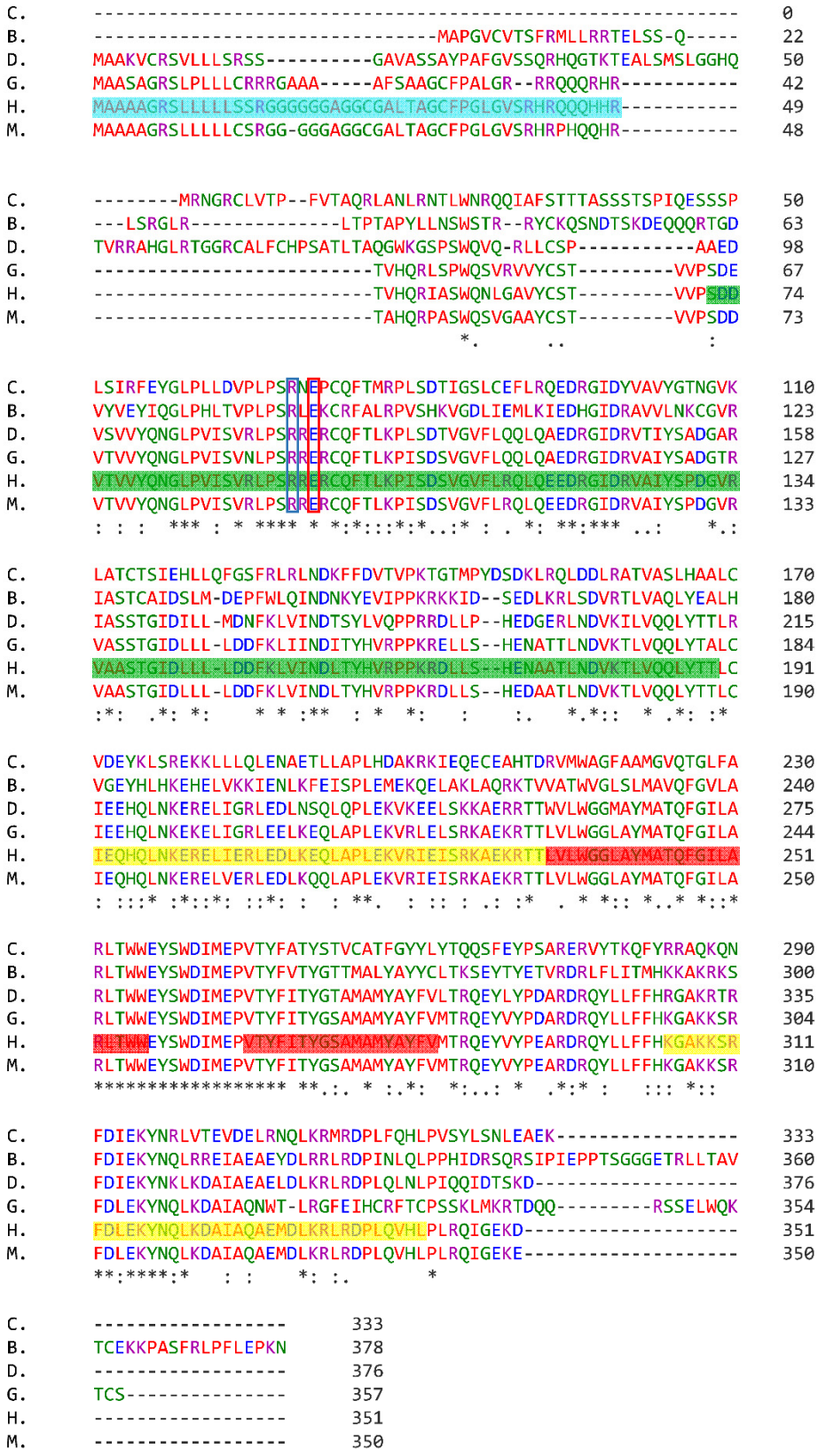
C. ---------- 0
B. ----------MAPGVCVTSFRMLLRRTELSS-Q----- 22
D. MAAKVCRSVLLLSRSS----------GAVASSAYPAFGVSSQRHQGTKTEALSMSLGGHQ 50
G. MAASAGRSLPLLLCRRRGAAA-----AFSAAGCFPALGR--RRQQQRHR---------- 42
H. MAAAAGRSLLLLLSSRGGGGGGAGGCGALTAGCFPGLGVSRHRQQQHHR---------- 49
M. MAAAAGRSLLLLLCSRGG-GGGAGGCGALTAGCFPGLGVSRHRPHQQHR---------- 48
C. --------MRNGRCLVTP--FVTAQRLANLRNTLWNRQQIAFSTTTASSSTSPIQESSSP 50
B. ---LSRGLR----------LTPTAPYLLNSWSTR--RYCKQSNDTSKDEQQQRTGD 63
D. TVRRAHGLRTGGRCALFCHPSATLTAQGWKGSPSWQVQ-RLLCSP----------AAED 98
G. ----------TVHQRLSPWQSVRVVYCST---------VVPSDE 67
H. ----------TVHQRIASWQNLGAVYCST---------VVPSDD 74
M. ----------TAHQRPASWQSVGAAYCST---------VVPSDD 73
C. LSIRFEYGLPLLDVPLPSRNEPCQFTMRPLSDTIGSLCEFLRQEDRGIDYVAVYGTNGVK 110
B. VYVEYIQGLPHLTVPLPSRLEKCRFALRPVSHKVGDLIEMLKIEDHGIDRAVVLNKCGVR 123
D. VSVVYQNGLPVISVRLPSRRERCQFTLKPLSDTVGVFLQQLQAEDRGIDRVTIYSADGAR 158
G. VTVVYQNGLPVISVNLPSRRERCQFTLKPISDSVGVFLQQLQAEDRGIDRVAIYSADGTR 127
H. VTVVYQNGLPVISVRLPSRRERCQFTLKPISDSVGVFLRQLQEEDRGIDRVAIYSPDGVR 134
M. VTVVYQNGLPVISVRLPSRRERCQFTLKPISDSVGVFLRQLQEEDRGIDRVAIYSPDGVR 133
C. LATCTSIEHLLQFGSFRLRLNDKFFDVTVPKTGTMPYDSDKLRQLDDLRATVASLHAALC 170
B. IASTCAIDSLM-DEPFWLQINDNKYEVIPPKRKKID--SEDLKRLSDVRTLVAQLYEALH 180
D. IASSTGIDILL-MDNFKLVINDTSYLVQPPRRDLLP--HEDGERLNDVKILVQQLYTTLR 215
G. VASSTGIDLLL-LDDFKLIINDITYHVRPPKRELLS--HENATTLNDVKTLVQQLYTALC 184
H. VAASTGIDLLL-LDDFKLVINDLTYHVRPPKRDLLS--HENAATLNDVKTLVQQLYTTLC 191
M. VAASTGIDLLL-LDDFKLVINDLTYHVRPPKRDLLS--HEDAATLNDVKTLVQQLYTTLC 190
C. VDEYKLSREKKLLLQLENAETLLAPLHDAKRKIEQECEAHTDRVMWAGFAAMGVQTGLFA 230
B. VGEYHLHKEHELVKKIENLKFEISPLEMEKQELAKLAQRKTVVATWVGLSLMAVQFGVLA 240
D. IEEHQLNKERELIGRLEDLNSQLQPLEKVKEELSKKAERRTTWVLWGGMAYMATQFGILA 275
G. IEEHQLNKEKELIGRLEELKEQLAPLEKVRLELSRKAEKRTTLVLWGGLAYMATQFGILA 244
H. IEQHQLNKERELIERLEDLKEQLAPLEKVRIEISRKAEKRTTLVLWGGLAYMATQFGILA 251
M. IEQHQLNKERELVERLEDLKQQLAPLEKVRIEISRKAEKRTTLVLWGGLAYMATQFGILA 250
C. RLTWWEYSWDIMEPVTYFATYSTVCATFGYYLYTQQSFEYPSARERVYTKQFYRRAQKQN 290
B. RLTWWEYSWDIMEPVTYFVTYGTTMALYAYYCLTKSEYTYETVRDRLFLITMHKKAKRKS 300
D. RLTWWEYSWDIMEPVTYFITYGTAMAMYAYFVLTRQEYLYPDARDRQYLLFFHRGAKRTR 335
G. RLTWWEYSWDIMEPVTYFITYGSAMAMYAYFVMTRQEYVYPDARDRQYLLFFHKGAKKSR 304
H. RLTWWEYSWDIMEPVTYFITYGSAMAMYAYFVMTRQEYVYPEARDRQYLLFFHKGAKKSR 311
M. RLTWWEYSWDIMEPVTYFITYGSAMAMYAYFVMTRQEYVYPEARDRQYLLFFHKGAKKSR 310
C. FDIEKYNRLVTEVDELRNQLKRMRDPLFQHLPVSYLSNLEAEK---------- 333
B. FDIEKYNQLRREIAEAEYDLRRLRDPINLQLPPHIDRSQRSIPIEPPTSGGGETRLLTAV 360
D. FDIEKYNKLKDAIAEAELDLKRLRDPLQLNLPIQQIDTSKD---------- 376
G. FDLEKYNQLKDAIAQNWT-LRGFEIHCRFTCPSSKLMKRTDQQ---------RSSELWQK 354
H. FDLEKYNQLKDAIAQAEMDLKRLRDPLQVHLPLRQIGEKD---------- 351
M. FDLEKYNQLKDAIAQAEMDLKRLRDPLQVHLPLRQIGEKE---------- 350
C. ---------- 333
B. TCEKKPASFRLPFLEPKN 378
D. ---------- 376
G. TCS---------- 357
H. ---------- 351
M. ---------- 350

Figure 3.2. Multiple sequence alignment of MCU from various organisms. *C. elegans* (C.) (NCBI, NP_500892.1), *B. dorsalis* (B.) (NCBI, XP_011204677.1), *D. rerio* (D.) (NCBI, NP_001070793), *G. gallus* (G.) (NCBI, XP_015143713.1), *H. sapiens* (H.) (NCBI, NP_612366.1) and *M. musculus* (M.) (NCBI, NP_001028431) sequences were aligned in Clustal Omega using the default settings *(Sievers & Higgins, 2014)*. Residue numbers are indicated at the right. Below the alignment, the (*) indicates fully conserved residues, (:) strongly similar residues, and (.) weakly similar residues. For the *H. sapiens* sequence, residue ranges corresponding to the domains shown in Fig. 3.1 are shaded the corresponding colour (signal peptide= teal, CC1 & CC2= yellow, TM1 & TM2= red). The residues shaded in green correspond to $MCU_{72\text{-}189}$. The fully-conserved R93 and E95 residues forming a salt bridge are bound by boxes.

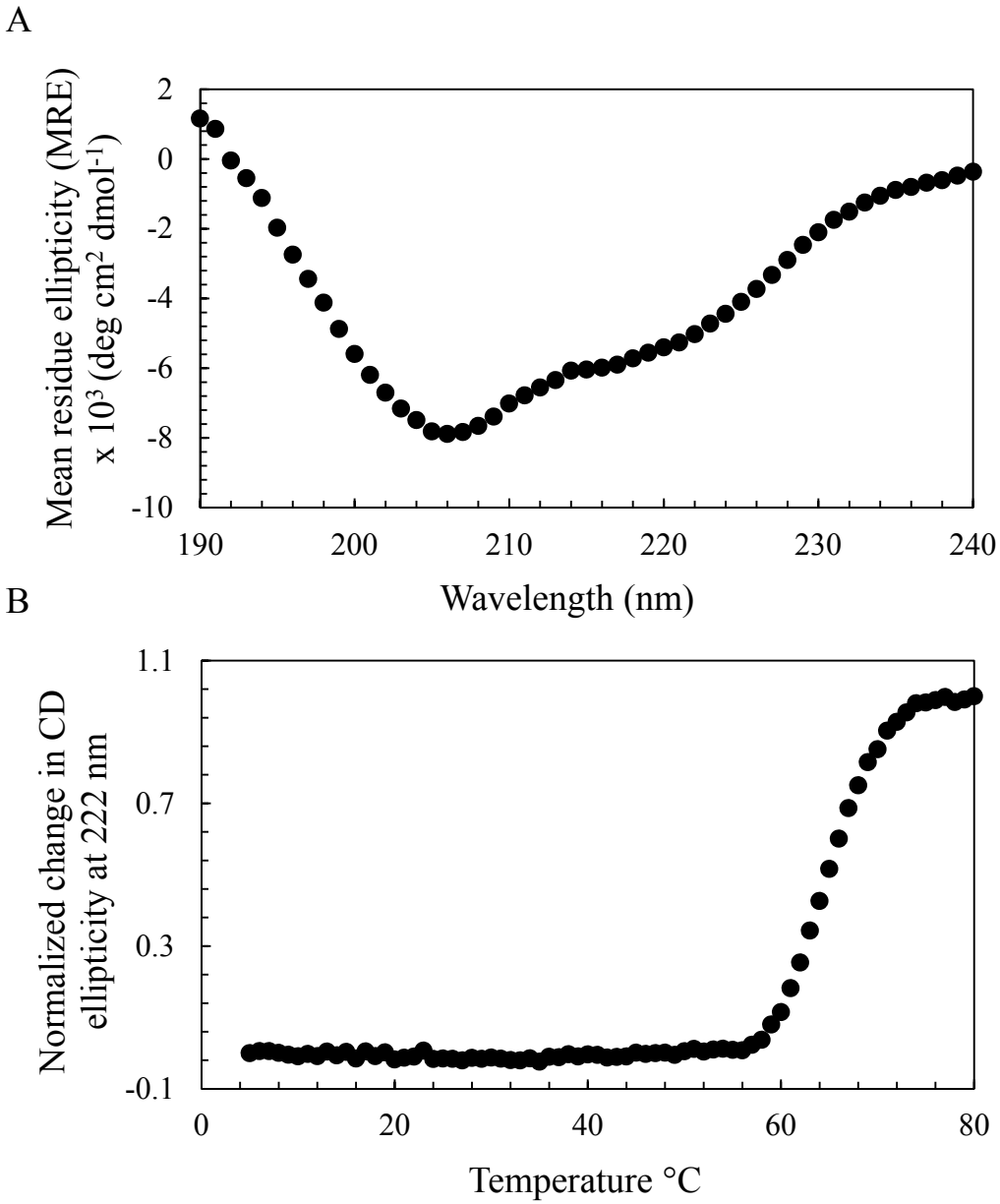

Figure 3.3. Secondary structure and stability of MCU_{72-189}. (A) Far-UV CD spectrum of MCU_{72-189}. α-helices are represented by negative ellipticity at ~208 and 222 nm, β-sheets are represented by negative ellipticity at ~215 nm, and random coils are represented by negative ellipticity at ~200 nm. The far-UV CD spectrum of MCU_{72-189} reveals a mixture of α-helices, β-sheets and random coil conformations. **(B)** Thermal stability of MCU_{72-189}. The change in far-UV CD ellipticity at 222 nm was taken as an indicator of thermal stability. The apparent temperature where the fractional change in ellipticity ≈ 0.5 (T_m) is ~65°C. Data is the average of three separate experiments (n=3) and acquired using 0.5 mg mL^{-1} protein in 20 mM Tris, 150 mM NaCl, 1 mM DTT, pH 8.0.

With MCU_{72-189} being a stably folded domain, I proceeded to crystallize MCU_{72-189} to solve its structure by first identifying conditions for crystallization of the WT MCU_{72-189}. These conditions were identified by performing initial sparse matrix screens, which contain conditions that proved to be successful for previous macromolecules, followed by further optimization of the crystal conditions. Since there was no available template structure to solve the phasing by molecular replacement, I crystallized an I141M/L146M MCU_{72-189} double mutant for selenomethionine (Se-Met) incorporation. Afterwards, the phase problem of the double mutant was solved by anomalous diffraction in collaboration with the M. Junop laboratory (Department of Biochemistry, Western University). With the crystal structure of the double mutant in hand, I then solved the crystal structure of the human native MCU_{72-189} protein under three different solution conditions by molecular replacement in collaboration with the M. Junop laboratory (Table 2).

The native WT structure, with a good resolution of 1.6 Å, revealed two central α-helices approximately perpendicular to one another, in between two three-stranded β-sheets (Fig. 3.4). The first β-sheet is arranged in an antiparallel manner, formed with three β-strands (β1; residues 76-80, β2; residues 83-88 and β3; residues 97-100). The β-strands are linked by one short loop (i.e. L1; residues 81-82) and one long loop (i.e. L2; residues 89-96). Furthermore, a salt bridge between the NH1 atom of R93 and the Oε1 atom of E95 stabilizes the L2 conformation (Fig. 3.5) (Costantini *et al.*, 2008). This salt bridge is in close proximity to a single Cys (i.e. C97) as well as a known phosphorylation site (i.e. S92), which may act to stabilize the loop for post-translational modifications of these residues (Joiner *et al.*, 2012; Lee *et al.*, 2015). Additionally, L3 (i.e. residues 101-107) connects a centrally located α1 helix (i.e. residues 108-118) to the N-terminal β-sheet. Located C-terminal to the central α1 helix is the second β-sheet, formed with three β-strands in an antiparallel orientation (β4; residues 125-128, β5; residues 149-153 and β6; residues 156-160). A short α-helix (i.e. α2; residues 141-146) that is perpendicular to α1 and also centrally positioned relative to the two β-sheets separates the β4 and β5 strands. This short α-helix is linked to the β4 and β5 strands through one long loop (i.e. L5; residues 129-140) and one short loop (i.e. L6; residues 147-148). Residues 168-189 of the C-terminal region of MCU_{72-189} do not show any appreciable electron density, suggesting that the C-terminal tail is dynamic under these conditions.

Table 2. Crystallographic data and refinement statistics.

	I141M/L146M MCU_{72-189} (Se-Met)	MCU_{72-189} ($MgCl_2$)	MCU_{72-189} ($LiSO_4$)	MCU_{72-189} ($CaCl_2$)
Data Collection:				
Resolution range (Å)	48.06-1.5 (1.53-1.5)	68.98-1.6 (1.63-1.6)	48.13-1.5 (1.53-1.5)	71.71-2.7 (2.85-2.7)
Unique reflections	19352	15893	19303	2858
Redundancy	11.3 (11.2)	11 (7.4)	11.4 (11.3)	5.4 (5.5)
Anomalous redundancy	5.4 (5.2)			
Mean (I/σI)	15.1 (3.4)	17.6 (3.2)	13.2 (4.9)	12.8 (3.5)
R_{merged} (%)	9.4 (106.1)	8.5 (63)	14.3 (163.6)	8.6 (43.8)
Completeness (%)	100 (100)	99.9 (99.4)	99.5 (98.9)	100 (100)
Anomalous completeness	100 (100)			
Unit cell	55.5, 55.5, 69.02	55.36, 55.36, 68.98	55.57, 55.57, 69.04	51.28, 51.28, 71.71
Angles	90, 90, 120	90, 90, 120	90, 90, 120	90, 90, 120
Space group	P65	P65	P65	P65
Mosaicity	0.23	0.41	0.22	1.05
Wilson B	18.5	17.4	11.7	61
Model and refinement:				
Resolution range (Å)	39.4-1.5	47.9-1.6	39.5-1.5	37.8-2.7
R_{work}/R_{free} (%)	20.4/21.8	17.2/20	18.5/20.7	27.3/30
Refl. observed	19312	15608	19107	2837
Refl. test set	1953	1560	1915	282
Protein atoms	736	745 [+1 Mg^{2+}]	730	730
Solvent atoms	87 water, 8 Tris	148 water	131 water	15 water
Rmsd bond lengths (Å)	0.008	0.005	0.005	0.004
Rmsd bond angles (°)	1.103	0.830	0.772	0.620
Wilson B	16.92	14.61	14.1	None given

Note: values in parenthesis are for the highest resolution shell

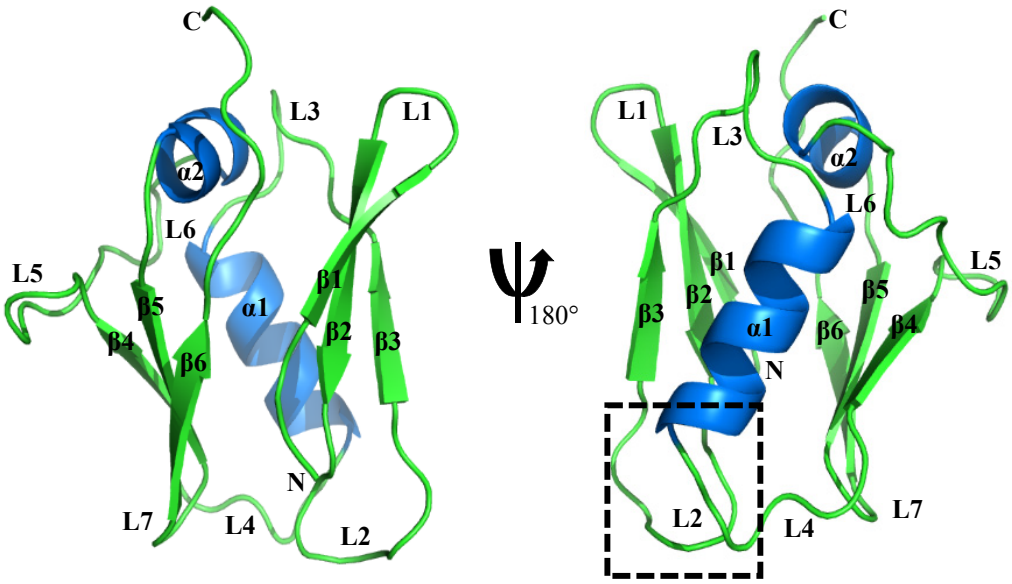

Figure 3.4. Ribbon view of the backbone structure of MCU_{72-189}. The β-strands (β1-β6, arrows) and loop regions (L1-L6) are colored green while the α-helices (α1, α2) are colored blue. The critical L2 region where the phosphorylation site, salt bridge and single Cys residue are found are bound by the broken box.

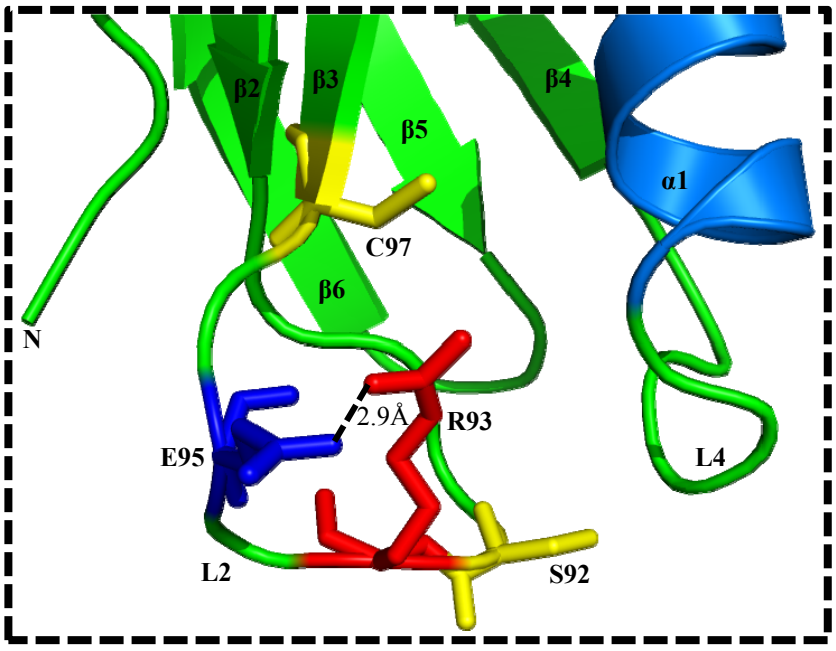

Figure 3.5. Zoomed view of L2. The R93 and E95 side chains forming an intramolecular salt bridge (Costantini *et al.*, 2008) are shown as red and blue sticks, respectively. The L2 C97 and S92 residues that may undergo post-translational modifications are shown as yellow sticks.

Overall, the tertiary structure of MCU_{72-189} hides 33 residues that are at least 85% solvent inaccessible (Cavallo *et al.*, 2003). In fact, the majority of these side chains are directed toward the inner core of the structure. On the contrary, residues V85 and V152, which are centrally located on each of the β-sheets, respectively, are directed away from the inner core (Fig. 3.6). These two residues may play roles in mediating protein-protein interactions and/or stabilizing the β-sheets at a more local level. When viewing the electrostatic surface of the protein, a prominent negative patch near the C-terminal face is shown, with residues D131, D142, D147, D148 and D166 contributing the majority of the acidic charge in this region (Fig. 3.7). A second negative patch closer to the N-terminal face of the protein is primarily comprised of residues E117, E118, E119, D124 and D155. Furthermore, two basic patches on the protein surface are comprised of residues R89, R93, R94 and R96, in addition to residues R113, R124 and R134, respectively (Fig. 3.7). The large degree of surface charge polarity exhibited by MCU_{72-189} may facilitate a relationship for higher order assembly of the domain.

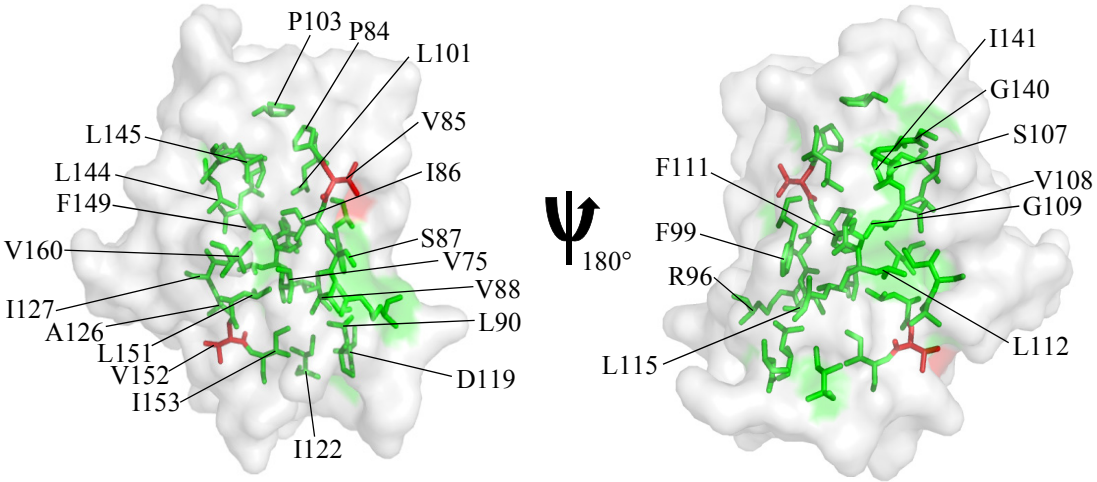

Figure 3.6. Hydrophobic core of MCU_{72-189}. Surface representation of MCU_{72-189} (white) with residues that are at least 85% solvent inaccessible are shown as sticks (green) that were calculated using Parameter OPtimsed Surfaces (POPS) (Cavallo *et al.*, 2003). The V85 and V152 side chains (red) that are directed away from the core, centrally located on each β-sheet, are indicated.

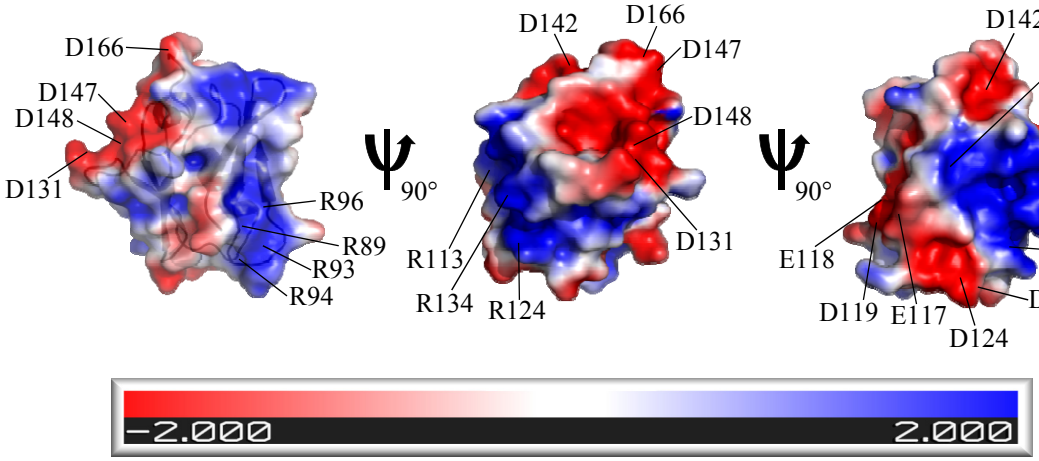

Figure 3.7. Electrostatic surface potential of MCU_{72-189}. The electrostatic potential was calculated by solving the Poisson-Boltzmann equation using the APBS and PDB2PQR tools (Baker *et al.*, 2001; Dolinsky *et al.*, 2007). The gradient shown is from −2 (acidic, red) to +2 (basic, blue) kT/e. Locations of only the surface charge acidic and basic residues are shown.

A DALI search for similar folds, performed by the DALI server which is a network service for comparing protein structures in 3D (Holm & Rosenstrom, 2010), revealed that the closest known structural homologue to MCU_{72-189} is ubiquitin-like protein 5 (ULP5), which also adopts a β-grasp fold. Although the sequence identity between the crystallized region of ULP5 and MCU_{72-189} is only ~5%, the backbone root mean square deviation (RMSD) between the two proteins is 3.0 Å (Fig. 3.8). Although MCU_{72-189} conforms to the core β-grasp structure consisting of a central α-helix that packs diagonally against a β-sheet with parallel and central N- and C-terminal β-strands (Burroughs *et al.*, 2007), it also contains unique differences from the core β-grasp structure. First, MCU_{72-189} contains a discontinuous sheet that is split into two halves, which is due to lack of hydrogen (H)-bonding between the central β1 and β6 strands. Additionally, a third β-strand is placed in the N-terminal sheet (i.e. β3) prior to the central helix, which changes the orientation of α1 by ~90°. Lastly, a short α-helix is located between β4 and β5, capping one end of the structure. The observed β-grasp-like fold of MCU_{72-189} is unlikely to be caused by expressing a small region of a larger protein, since exclusion of the first two β-strands (i.e. leaving a 4-stranded core with the N- and C-terminal strands parallel) results in a destabilized conformation (Fig. 3.9).

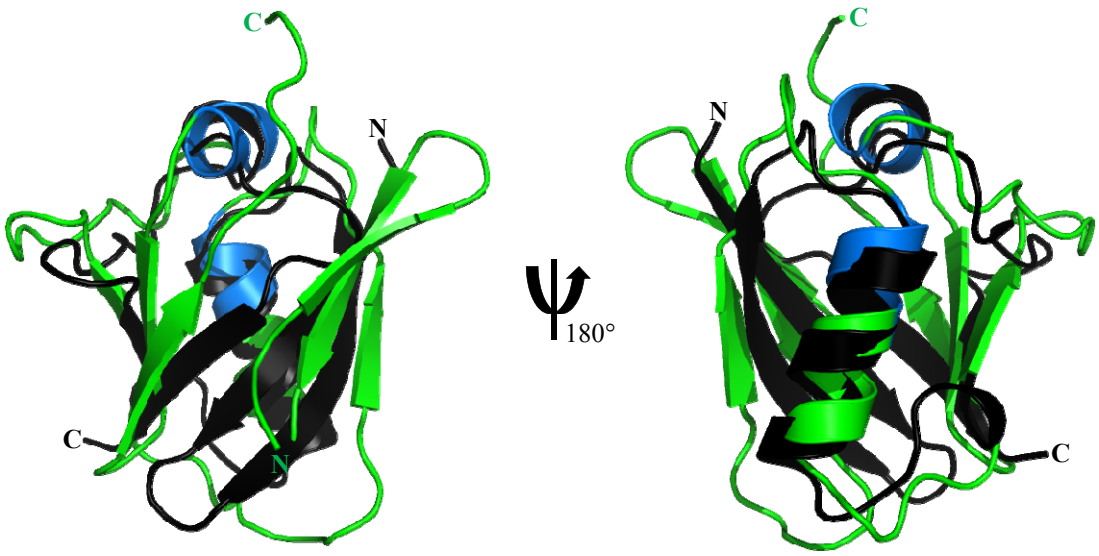

Figure 3.8. Structural alignment of MCU_{72-189} and ULP5. ULP5 (4pyu.pdb) was identified by DALI (Holm & Rosenstrom, 2010) as the closest structural homologue to MCU_{72-189}. The backbone alignment for ULP5 (black ribbon) and MCU_{72-189} (green and blue ribbon) are shown with a 3.0 Å RMSD between the two proteins over 74 residues, despite only 5% sequence identity.

A

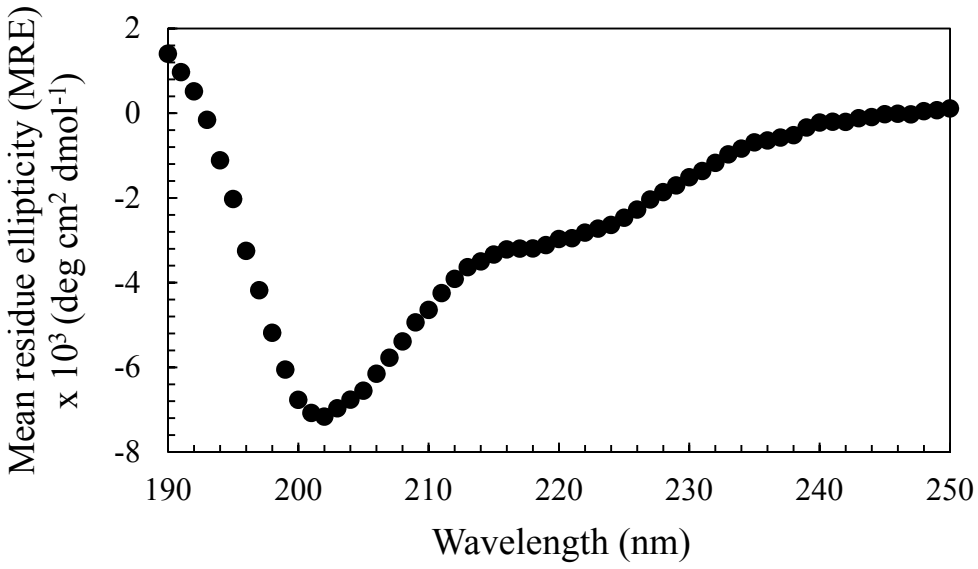
Mean residue ellipticity (MRE)
x 10³ (deg cm² dmol⁻¹)
2
0
-2
-4
-6
-8
190
200
210
220
230
240
250
Wavelength (nm)

B

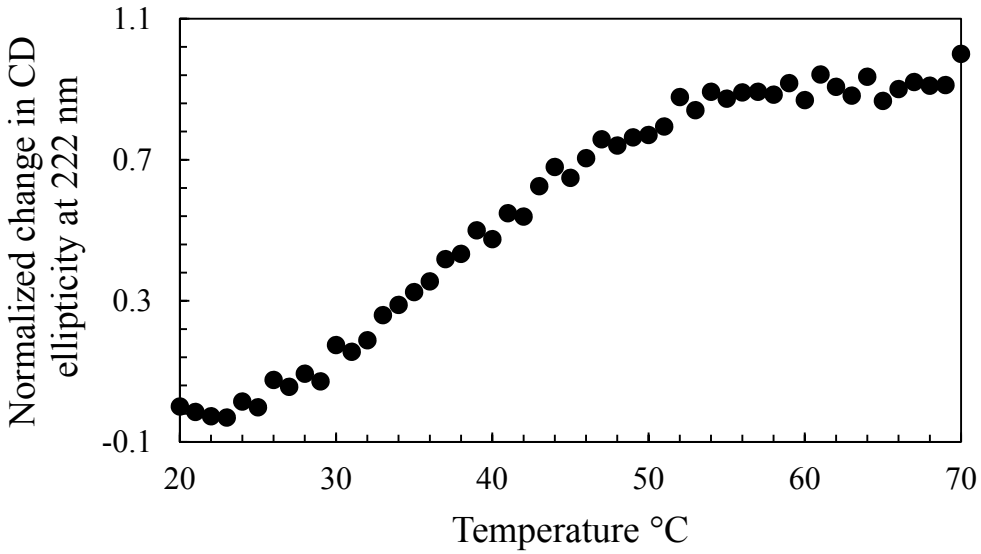
Normalized change in CD
ellipticity at 222 nm
1.1
0.7
0.3
-0.1
20
30
40
50
60
70
Temperature °C

Figure 3.9. Secondary structure and stability of $MCU_{105-189}$. (A) Far-UV CD spectrum of $MCU_{105-189}$. α-helices are represented by negative ellipticity at ~208 and 222 nm, β-sheets are represented by negative ellipticity at ~215 nm, and random coils are represented by negative ellipticity at ~200 nm. The far-UV CD spectrum of $MCU_{105-189}$ reveals a mixture of α-helices, β-sheets and random coil conformations. Relative to MCU_{72-189}, the far-UV CD spectrum of $MCU_{105-189}$ reveals a shift to a lower wavelength in the 208 nm peak as well as less negativity at ~215 and ~222 nm, indicating more protein disorder. **(B)** Thermal stability of $MCU_{105-189}$. The change in far-UV CD ellipticity at 222 nm was taken as an indicator of thermal stability. The apparent temperature where the fractional change in ellipticity ≈ 0.5 (T_m) is ~39°C, which is ~26°C less stable than MCU_{72-189}. The cooperativity of the curve is also decreased, indicating that $MCU_{105-189}$ exists as a less compact and folded structure relative to MCU_{72-189}. Data is the average of three separate experiments (n=3) and acquired using 0.5 mg mL^{-1} protein in 20 mM Tris, 150 mM NaCl, pH 8.0.

3.2 The β-grasp-like domain of MCU interacts with Mg^{2+} and Ca^{2+}

MCU_{72-189} was successfully crystallized in the presence of $MgCl_2$, and under these crystallization conditions, a Mg^{2+} atom was found near the negatively charged D131, D147 and D148 side chains, which are primary contributors to the major acidic surface patch (Fig. 3.10A). D147 side chain atoms Oδ1 and Oδ2 are within 3.5 and 2.1 Å, respectively, of the centrally located Mg^{2+} ion in the acidic patch. On the other hand, the D131 and D148 side chains are positioned further away (i.e. minimum Oδ distance ~6.6 Å) (Fig. 3.10B). The Mg^{2+} ion is coordinated by the D147 Oδ2 atom and five water molecules arranged in an octahedral geometry (Fig. 3.11). The arrangement of the five ligand water molecules and the D147 carboxylate surrounding the Mg^{2+} is visible in the $2F_o$-F_c electron density map contoured at 2.0σ. Furthermore, an F_o-F_c omit map contoured at 9.0σ shows the unaccounted for electron density when the Mg^{2+} atom is not modeled into the structure (Fig. 3.11).

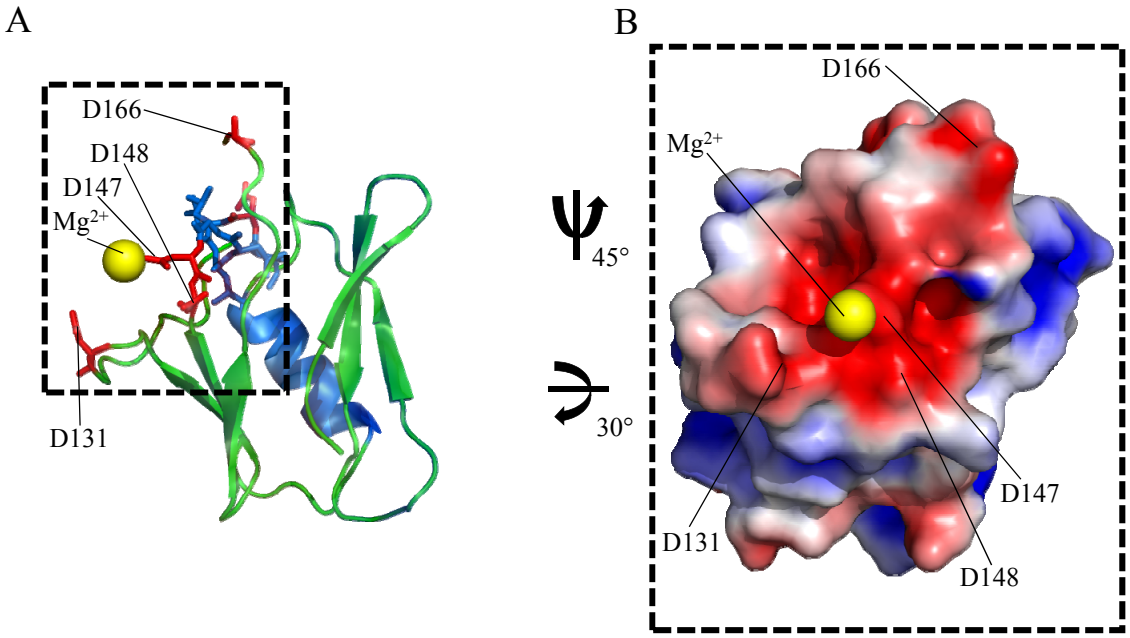

Figure 3.10. Mode of Mg^{2+} binding to MCU_{72-189}. (A) Location of the Mg^{2+} atom (yellow sphere) relative to the backbone structure (ribbon view) and acidic side chains (red sticks) contributing to the prominent negative patch on MCU_{72-189}. The broken box demarcates the acidic patch region. Closest distances from the Asp side chains of D131, D147 and D148 to the Mg^{2+} atom are 6.6 Å, 2.1 Å and 6.6 Å, respectively. **(B)** Enlarged view of the acidic patch shown in (A). The Mg^{2+} atom (yellow sphere) centrally located in the acidic patch is shown.

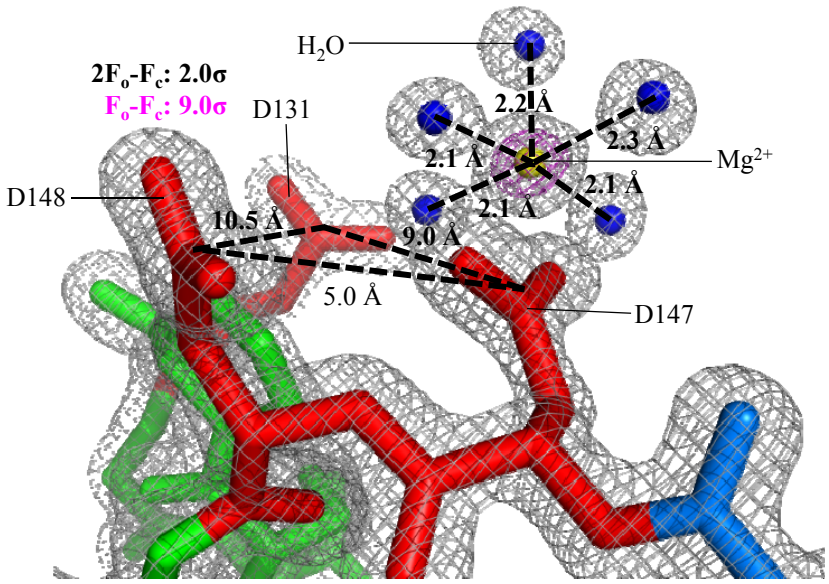

Figure 3.11. Mg^{2+} atom coordination geometry. The $2F_o$-F_c (2.0 σ) electron density map (grey mesh) is shown with the modeled protein chain (sticks), water molecules (blue spheres) and the Mg^{2+} atom (yellow sphere). The F_o-F_c (9.0 σ) omit map (magenta mesh) shows a distinct, unaccounted for density in the absence of the Mg^{2+} atom. Distances between the Asp (red sticks) Cγ atoms are indicated. The octahedral coordination of Mg^{2+} between the D147 Oε1 and five water molecules is shown with oxygen atom distances indicated. The electron density map was created using CCP4 software (Winn *et al.*, 2011).

In addition to $MgCl_2$, $MCU_{72\text{-}189}$ was also successfully crystallized with either $LiSO_4$ or $CaCl_2$ (Table 2). In the presence of $LiSO_4$ (1.5 Å), the F_o-F_c omit map contoured at 2.5σ shows no unaccounted for electron density in the acidic patch, demonstrating electron density associated with the atom only in the presence of $MgCl_2$ (Fig. 3.12). In the presence of $CaCl_2$, the crystallized structure showed much lower resolution than the $MgCl_2$ or $LiSO_4$ structures (i.e. 2.7 Å versus 1.5-1.6 Å), and hence, a Ca^{2+} atom could not be reliably located. The lack of a Ca^{2+} atom may be due to the lower resolution, as well as a twining problem associated with this crystal structure, contributing to lower data quality. However, all three backbone structures are very similar to one another (Fig. 3.13).

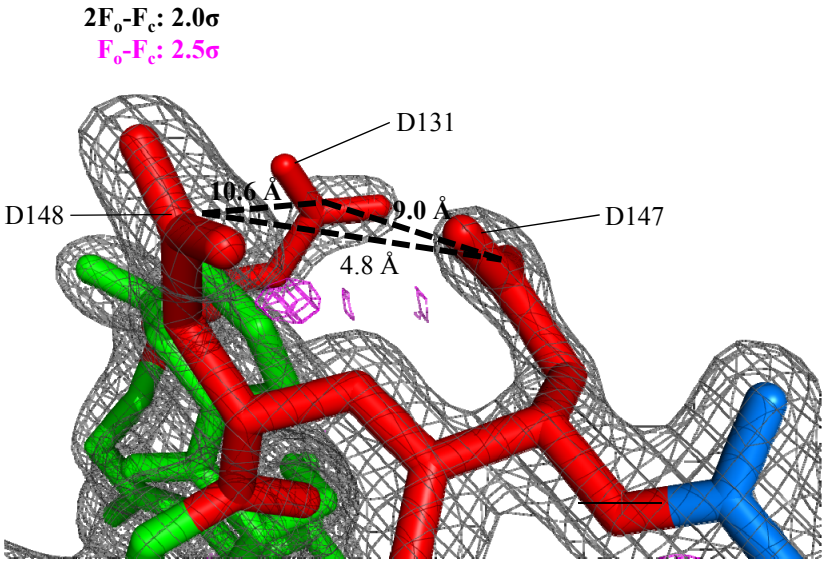

Figure 3.12. Electron density map of MCU_{72-189} solved in the presence of $LiSO_4$. The $2F_o$-F_c (2.0 σ) map (grey mesh) of the same region shown in Fig 3.11 does not exhibit evidence for a cation, and the F_o-F_c (2.5 σ) map (magenta mesh) shows no unaccounted for density. The electron density map was created using CCP4 software (Winn *et al.*, 2011).

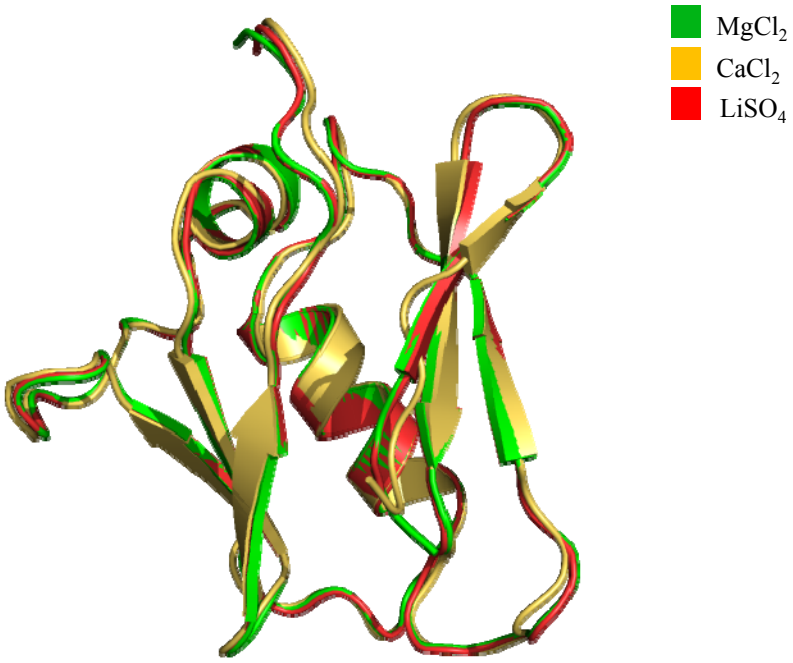

Figure 3.13. Ribbon view of the backbone alignments of MCU_{72-189} structures. The structures were solved in the presence of $MgCl_2$ (green), $CaCl_2$ (yellow) and $LiSO_4$ (red). Structural alignments were performed with Theseus (Theobald & Wuttke, 2008).

With the discovery of a Mg^{2+} ion bound to MCU_{72-189} in the crystal state, I then proceeded to characterize the cation binding in solution. I used changes in MCU_{72-189} intrinsic fluorescence to monitor structural changes associated with Mg^{2+} or Ca^{2+} binding. In divalent cation-free conditions and using an excitation wavelength (λ_{ex}) of 280 nm, MCU_{72-189} showed an intrinsic fluorescence emission maximum at a wavelength (λ_{em}) of ~305 nm. This is consistent with Tyr fluorescence and the absence of Trp in the domain (Preston & Phillips, 2016). Furthermore, addition of 5 mM $MgCl_2$ or $CaCl_2$ decreased the intrinsic fluorescence of MCU_{72-189} (Fig. 3.14A and 3.14B), in which a systematic decrease in intrinsic fluorescence was observed upon increasing concentrations of $MgCl_2$ or $CaCl_2$. It was also revealed that guanidine-induced denaturation decreased the intrinsic fluorescence of MCU_{72-189}, which may suggest that the fluorescence change observed in the $MgCl_2$ and $CaCl_2$ titrations reflect some loss in structure associated with cation binding (Fig. 3.14C). Plots of the changes in fluorescence intensity at the wavelength showing maximum fluorescence change (i.e. λ_{ex}=280 nm; λ_{em}=302 nm) versus $MgCl_2$ or $CaCl_2$ showed saturable binding of Mg^{2+} and Ca^{2+}. After fitting the binding curves to a one-site binding model that takes into account protein concentration, apparent equilibrium dissociation constants for Mg^{2+} ($K_{D,Mg2+}$) and Ca^{2+} ($K_{D,Ca2+}$) were found to be ~1.7 and ~2.3 mM, respectively (Fig. 3.15).

A

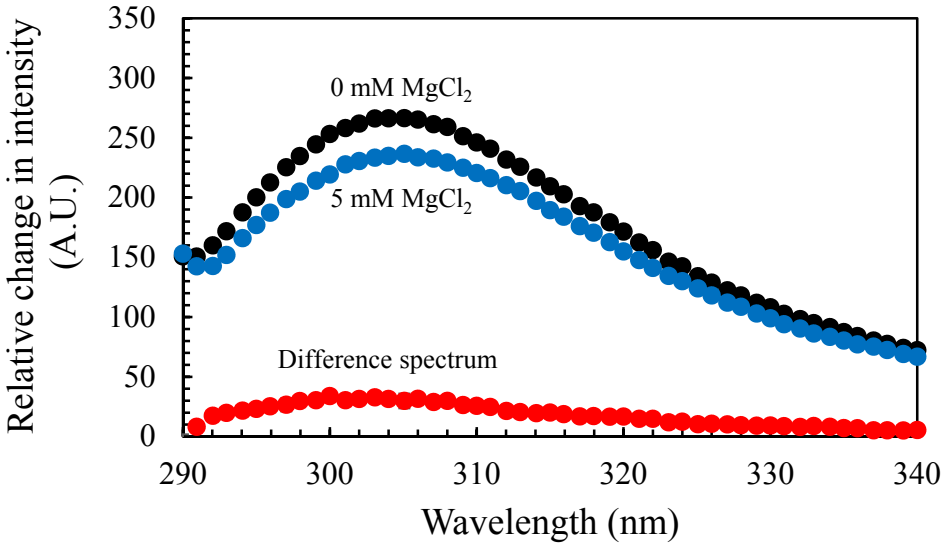
Relative change in intensity (A.U.)
350
300
250
200
150
100
50
0
0 mM MgCl2
5 mM MgCl2
Difference spectrum
290
300
310
320
330
340
Wavelength (nm)

B

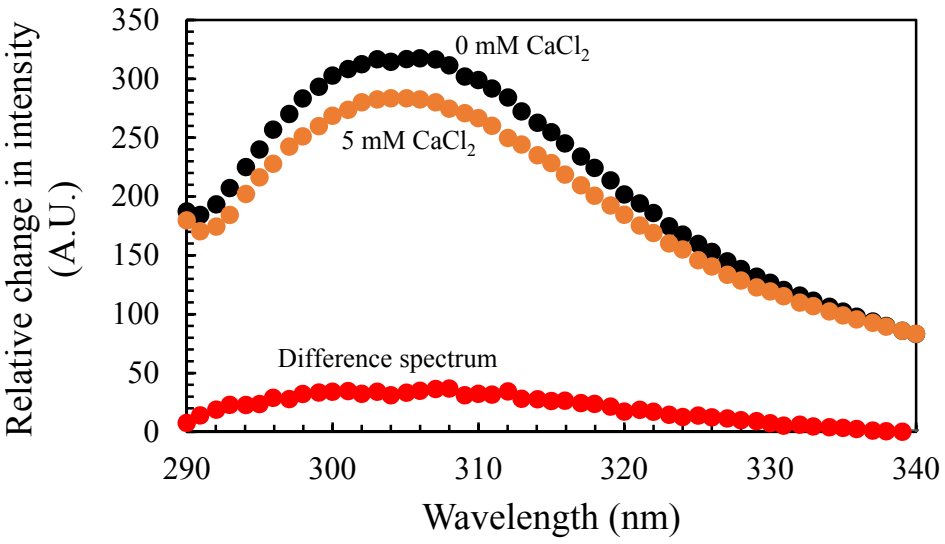
Relative change in intensity (A.U.)
350
300
250
200
150
100
50
0
0 mM CaCl2
5 mM CaCl2
Difference spectrum
290
300
310
320
330
340
Wavelength (nm)

C

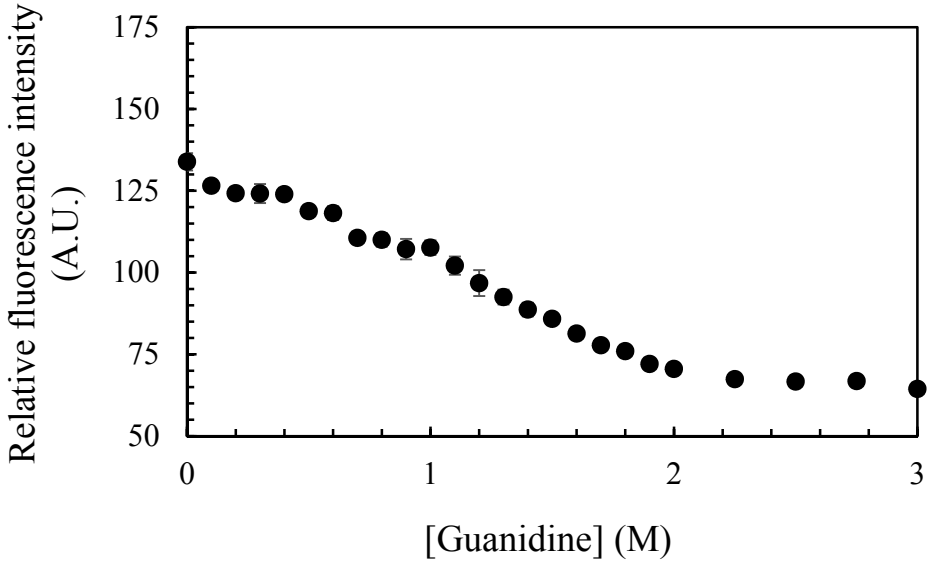
Relative fluorescence intensity (A.U.)
175
150
125
100
75
50
0
1
2
3
[Guanidine] (M)

Figure 3.14. Cation-dependent intrinsic fluorescence changes and chemical denaturation of MCU_{72-189}. (A) Fluorescence emission spectra of MCU_{72-189} in the absence (black circles) and presence (blue circles) of 5 mM $MgCl_2$. The difference spectrum (i.e. 5 mM $MgCl_2$ spectrum - 0 mM $MgCl_2$ spectrum) is shown (red circles). **(B)** Fluorescence emission spectra of MCU_{72-189} in the absence (black circles) and presence (orange circles) of 5 mM $CaCl_2$. The difference spectrum (i.e. 5 mM $CaCl_2$ spectrum - 0 mM $CaCl_2$ spectrum) is shown (red circles). Data in (A) and (B) are the average of three separate experiments (n=3) acquired using 0.5 mg mL^{-1} protein in 20 mM HEPES, 150 mM KCl, 2 mM DTT, pH 7.5, 25°C and an excitation wavelength (λ_{ex}) of 280 nm. Error bars represent SEM. **(C)** Guanidine induced denaturation of MCU_{72-189} monitored by changes in intrinsic fluorescence. Changes in intrinsic fluorescence using λ_{ex}=275 nm and λ_{em}=305 nm are plotted versus guanidine-HCl concentration. The guanidine concentration-dependent decrease in fluorescence is indicative of MCU_{72-189} unfolding. Data is the average of three separate experiments (n=3) acquired using 0.2 mg mL^{-1} protein in 20 mM HEPES, 150 mM KCl, 2 mM DTT, pH 7.5 at 25°C. Error bars represent SEM.

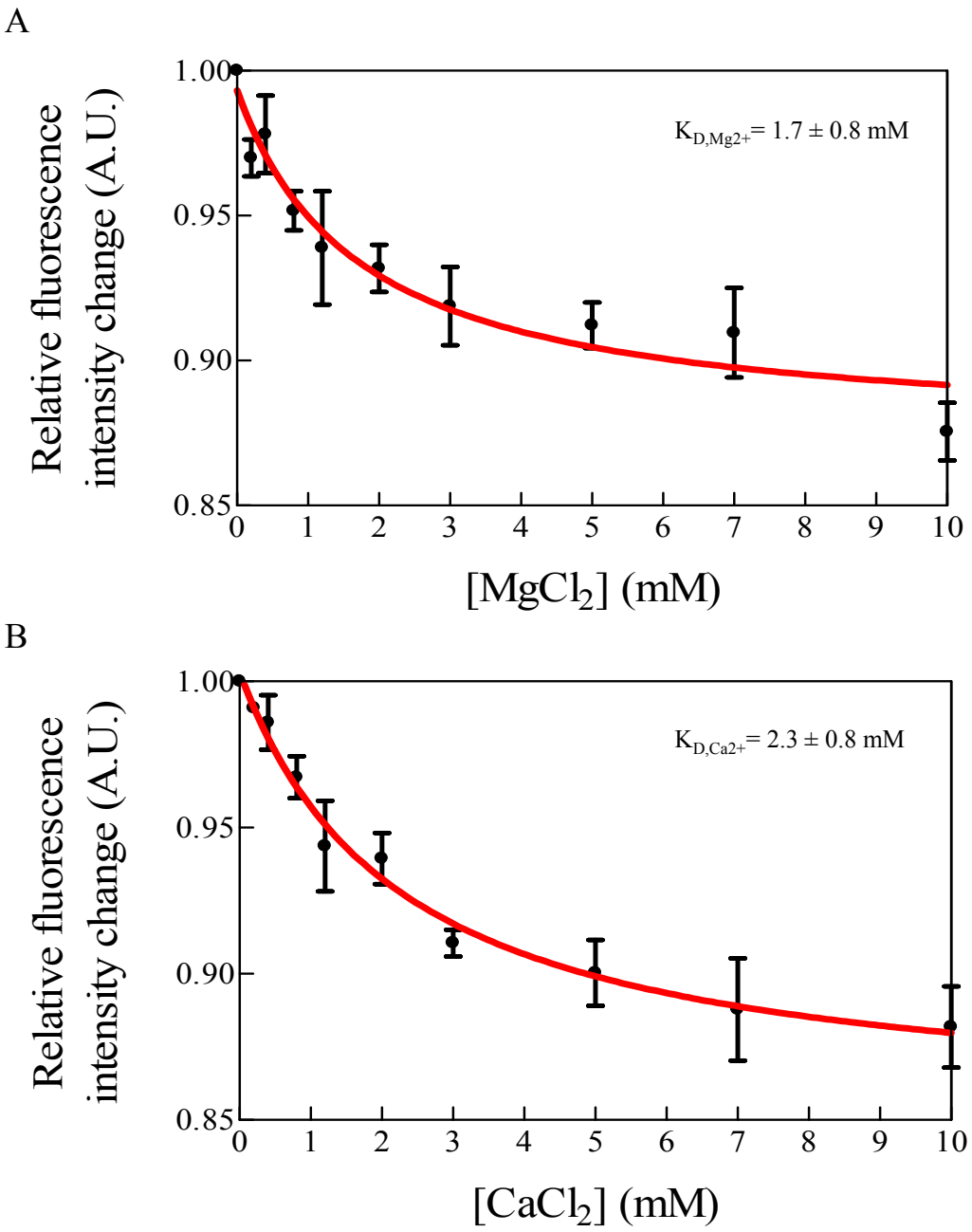

Figure 3.15. Effect of cations on MCU_{72-189} intrinsic fluorescence. Changes in intrinsic fluorescence as a function of $MgCl_2$ **(A)** and $CaCl_2$ **(B)** concentrations at 25°C. Data were fitted to a one-site binding curve (red line) taking into account protein concentration. Data is the average of three separate experiments (n=3) acquired using 0.5 mg mL^{-1} protein in 20 mM HEPES, 150 mM KCl, 2 mM DTT, pH 7.5. Error bars represent SEM.

To evaluate whether Mg^{2+} or Ca^{2+} binding to MCU_{72-189} influences secondary structure or stability in solution, I assessed the far-UV CD spectrum of the protein as a function of increasing Mg^{2+} or Ca^{2+} levels. It was found that cation binding to MCU_{72-189} does not appreciably alter secondary structure, as increasing concentrations of Mg^{2+} or Ca^{2+} minimally changed the far-UV CD ellipticity (Fig. 3.16). The effects on MCU_{72-189} stability were also evaluated through changes in far-UV CD signal at 222 nm as a function of temperature in the presence and absence of $MgCl_2$ or $CaCl_2$. In the absence of cations, MCU_{72-189} had an apparent T_m of ~66°C. Addition of 40 mM $MgCl_2$ to the protein decreased the T_m of MCU_{72-189} to ~62°C (Fig. 3.17A). Remarkably, addition of 40 mM $CaCl_2$ destabilized the protein to a greater extent than $MgCl_2$, resulting in a T_m value of ~59°C (Fig. 3.17B).

Altogether, results from the crystal structures, solution far-UV CD spectroscopy and intrinsic fluorescence suggest that MCU_{72-189} binds Mg^{2+} and Ca^{2+} with ~mM affinity on an acidic region of the protein surface, resulting in destabilization of the domain.

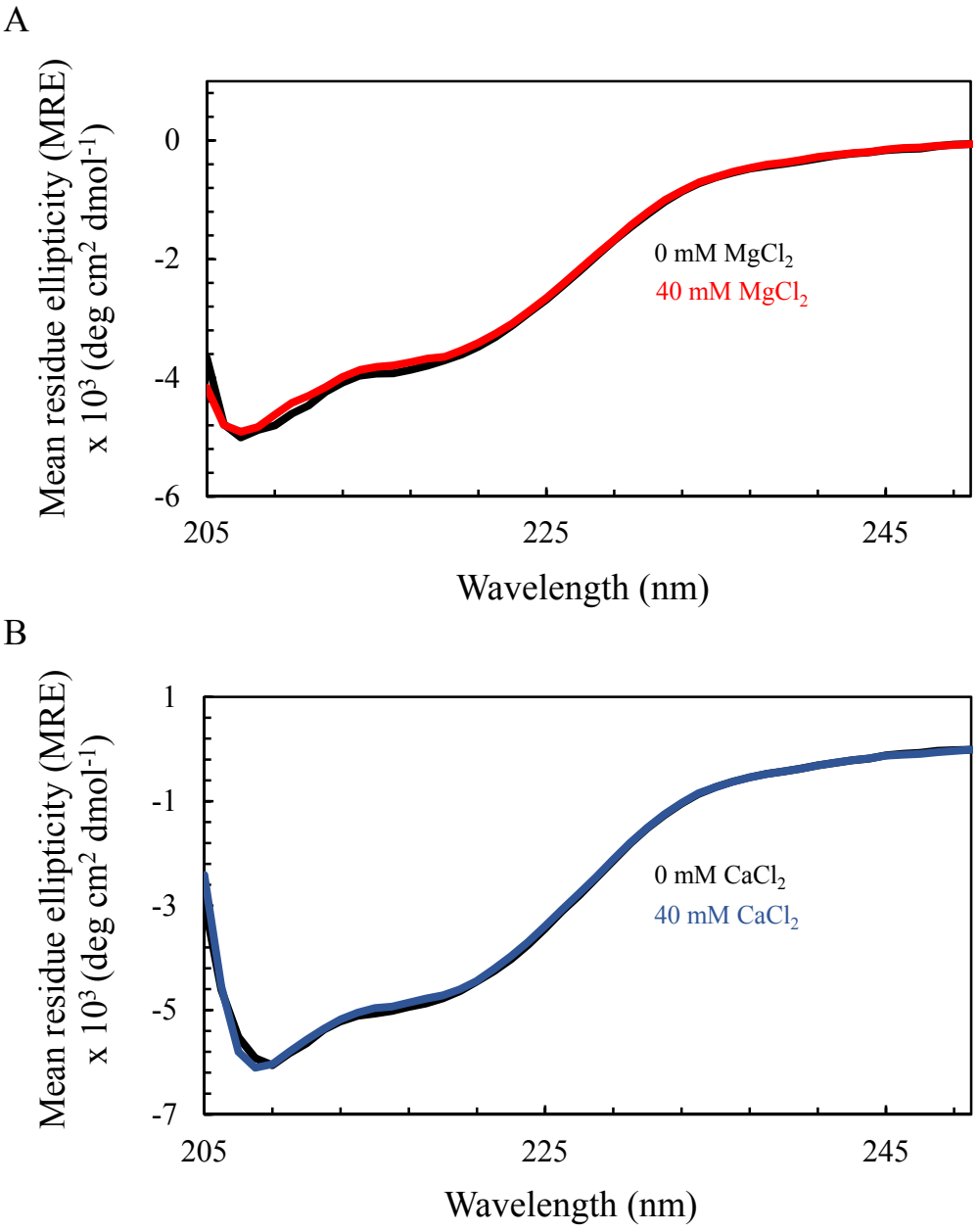

Figure 3.16. Secondary structure of MCU_{72-189}. Effects of $MgCl_2$ **(A)** and $CaCl_2$ **(B)** on MCU_{72-189} secondary structure. Shown are the far-UV CD spectra in the absence (black line) and presence of 40 mM $MgCl_2$ (red line) or $CaCl_2$ (blue line) acquired at 4°C. Data is the average of three separate experiments (n=3) acquired using 0.5 mg mL^{-1} protein in 20 mM HEPES, 150 mM KCl, 2 mM DTT, pH 7.5.

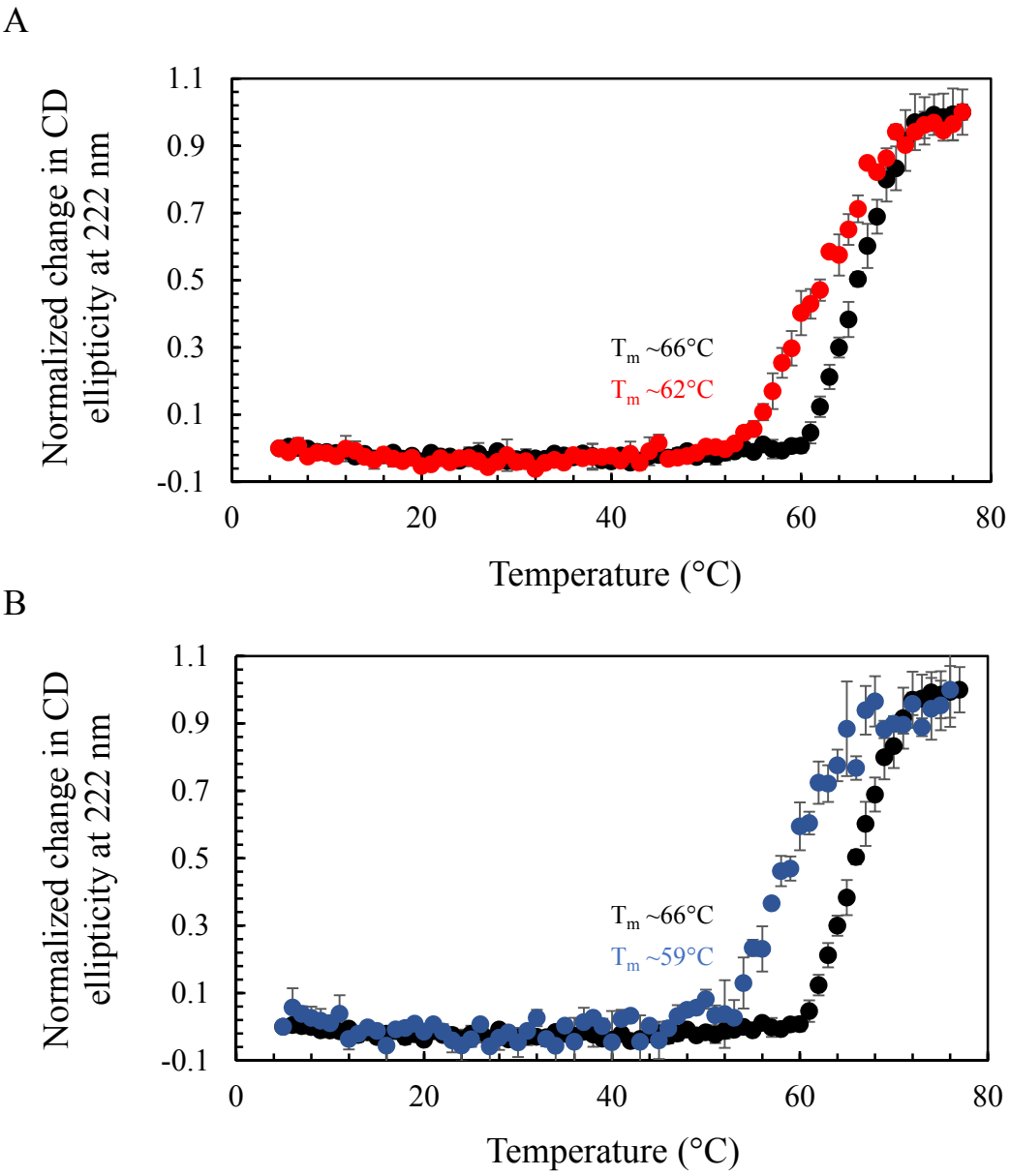

Figure 3.17. Stability of MCU_{72-189}. MCU_{72-189} stability sensitivity to $MgCl_2$ **(A)** and $CaCl_2$ **(B)**. Stability was assessed from changes in ellipticity as a function of temperature in the absence (black circles) and presence of 40 mM $MgCl_2$ (red circles) or $CaCl_2$ (blue circles). Data is the average of three separate experiments (n=3) and acquired using 0.5 mg mL^{-1} protein in 20 mM HEPES, 150 mM KCl, 2 mM DTT, pH 7.5. Error bars represent SEM.

3.3 Ca^{2+} promotes MCU_{72-189} monomerization and weakens self-association

With relatively small secondary structural changes associated with Mg^{2+} or Ca^{2+} binding, I proceeded to determine if other factors might contribute to the destabilization due to cation binding. AUC was performed to assess the quaternary structure of MCU_{72-189}. After globally fitting the equilibrium data to a single ideal species, molecular weights of ~22.3, 21.5 and 18.5 kDa for samples prepared at 1.2, 0.8 and 0.4 mg mL^{-1}, respectively, were revealed (Fig. 3.18A, 3.18B and 3.18C; Table 3). Moreover, these fitted molecular weights corresponded to 1.6, 1.5 and 1.3× the theoretical monomeric mass of ~13.9 kDa, indicating a concentration dependence and fast exchange equilibrium. This fast exchange equilibrium is indicated by the equilibrium data with MWs between the monomer and dimer theoretical masses. Due to the larger destabilization of MCU_{72-189} caused by Ca^{2+} compared to Mg^{2+}, I then performed AUC of MCU_{72-189} in the presence of 40 mM $CaCl_2$. After global fitting of the equilibrium data to a single ideal species, $CaCl_2$ was shown to decrease the fitted molecular weights to ~20.0, 18.8 and 16.2 kDa, corresponding to 1.4, 1.4 and 1.2× the theoretical monomeric mass for the 1.2, 0.8 and 0.4 mg mL^{-1} datasets, respectively (Fig. 3.18D, 3.18E and 3.18F; Table 3). Therefore, $CaCl_2$ appears to shift the monomer-dimer equilibrium of MCU_{72-189} toward monomer.

Another reason I performed AUC was to quantify the strength of the self-association of MCU_{72-189} in the presence and absence of $CaCl_2$. After globally fitting the equilibrium data to a monomer-dimer equilibrium model, the apparent equilibrium dissociation constants for the monomer-dimer equilibrium ($K_{D,dimer}$) were determined at the three protein concentrations. Apparent $K_{D,dimer}$ values of MCU_{72-189} were 58.6, 77.9 and 126 μM for the 1.2, 0.8 and 0.4 mg mL^{-1} datasets, respectively (Fig. 3.19A, 3.19B and 3.19C; Table 3). Global fitting of the 40 mM $CaCl_2$ equilibrium data to a monomer-dimer equilibrium model was also performed. In the presence of 40 mM $CaCl_2$, the globally fitted apparent $K_{D,dimer}$ values were 139, 197 and 369 μM. These values are ~2× higher than the apparent $K_{D,dimer}$ values measured in the absence of $CaCl_2$, indicating weaker affinity for self-association (Fig. 3.19D, 3.19E and 3.19F; Table 3). Therefore, $CaCl_2$ weakens the affinity of MCU_{72-189} self-association.

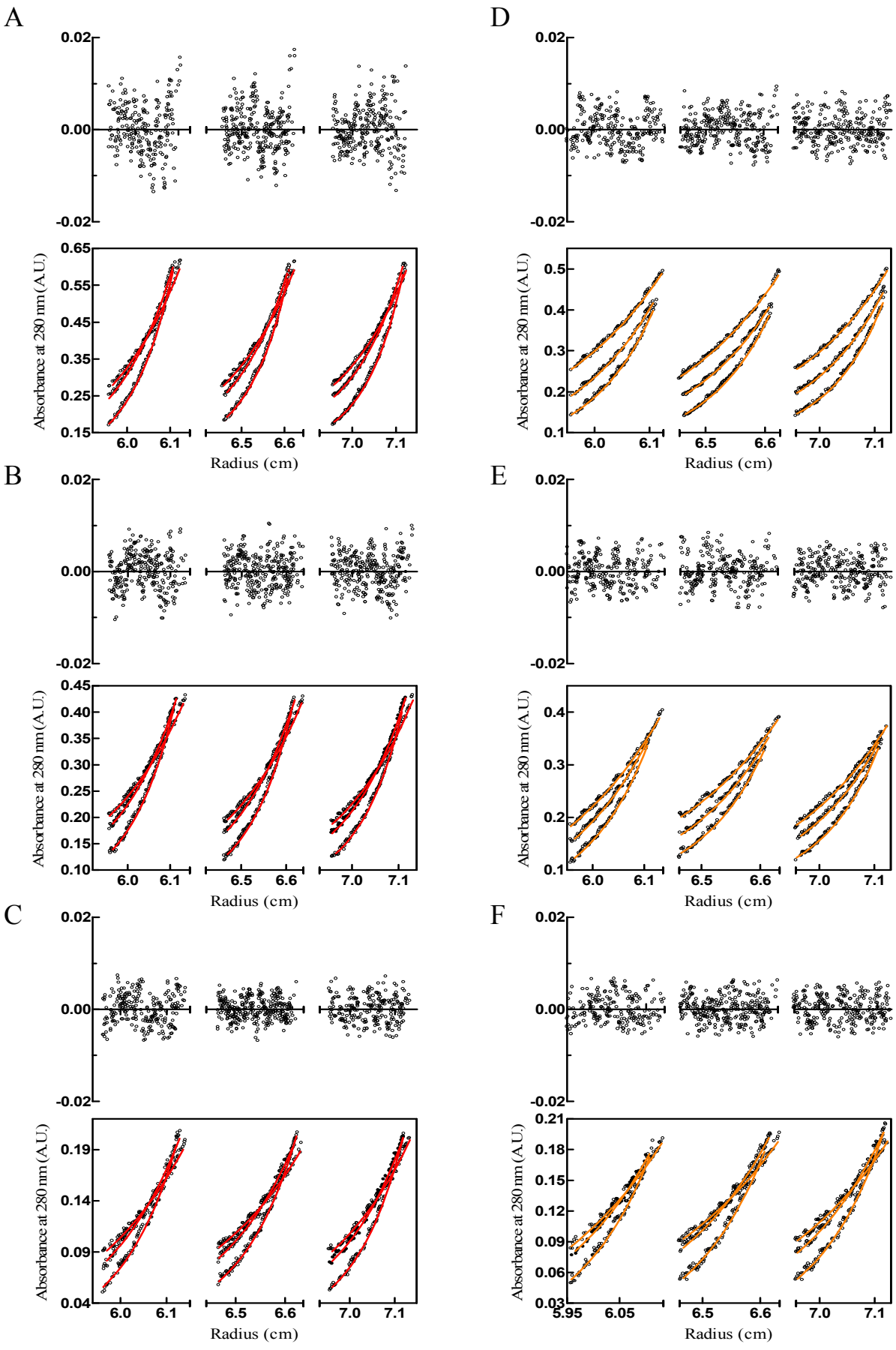
A
B
C
D
E
F
Absorbance at 280 nm (A.U.)
Radius (cm)

Figure 3.18. Equilibrium ultracentrifugation molecular weight analysis of MCU_{72-189} in the absence and presence of $CaCl_2$. Sedimentation equilibrium of MCU_{72-189} in the absence of $CaCl_2$ at 1.4 mg mL^{-1} **(A)**, 0.8 mg mL^{-1} **(B)** and 0.4 mg mL^{-1} **(C)**. Data were acquired at 18,000, 21,000 and 25,000 rpm at 25°C. The red lines through the data are from a global single ideal molecular weight fit within each respective panel. The residuals for the fits are shown on the top of each panel. Sedimentation equilibrium of MCU_{72-189} in the presence of 40 mM $CaCl_2$ performed at 1.4 mg mL^{-1} **(D)**, 0.8 mg mL^{-1} **(E)** and 0.4 mg mL^{-1} **(F)**. Data were acquired at 18,000, 21,000 and 25,000 rpm at 25°C. The orange lines through the data are from a global single ideal molecular weight fit within each respective panel. The residuals for the fits are shown on the top of each panel. Data in all panels were acquired in 20 mM HEPES, 150 mM KCl, 2 mM DTT, pH 7.5 at 25°C.

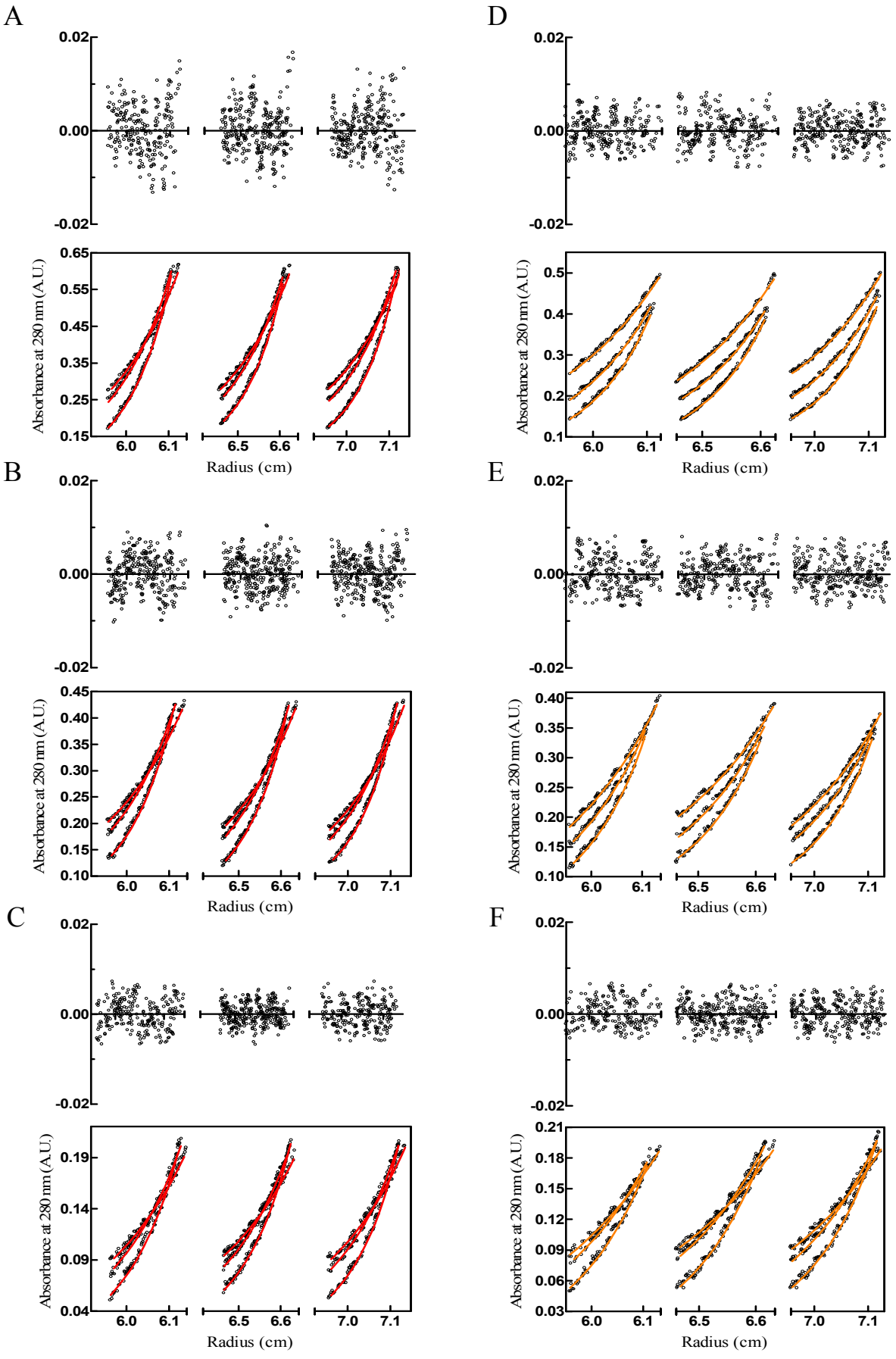
A
B
C
D
E
F
Absorbance at 280 nm (A.U.)
Radius (cm)
0.02
0.00
-0.02
6.0
6.1
6.5
6.6
7.0
7.1

Figure 3.19. Equilibrium ultracentrifugation self-association analysis of MCU_{72-189} in the absence and presence of $CaCl_2$. Sedimentation equilibrium of MCU_{72-189} in the absence of $CaCl_2$ at 1.4 mg mL^{-1} **(A)**, 0.8 mg mL^{-1} **(B)** and 0.4 mg mL^{-1} **(C)**. Data were acquired at 18,000, 21,000 and 25,000 rpm at 25°C. The red lines through the data are from a monomer-dimer equilibrium fit within each respective panel. The residuals for the fits are shown on the top of each panel. Sedimentation equilibrium of MCU_{72-189} in the presence of 40 mM $CaCl_2$ performed at 1.4 mg mL^{-1} **(D)**, 0.8 mg mL^{-1} **(E)** and 0.4 mg mL^{-1} **(F)**. Data were acquired at 18,000, 21,000 and 25,000 rpm at 25°C. The orange lines through the data are from a monomer-dimer equilibrium fit within each respective panel. The residuals for the fits are shown on the top of each panel. Data in all panels were acquired in 20 mM HEPES, 150 mM KCl, 2 mM DTT, pH 7.5 at 25°C.

Table 3. Molecular weights and dimerization affinities as determined from AUC data.

[protein] (mg mL^{-1})	$CaCl_2$[a]	MW (Da)[b]	SE	Stoichiometry[c]	R^2[d]	K_D, Dimer[e] (mM)	SE	R^2[d]
1.2	-	22851	226	1.65	0.998	0.059	0.007	0.998
0.8	-	21465	227	1.55	0.998	0.078	0.008	0.998
0.4	-	18543	346	1.34	0.995	0.126	0.019	0.995
1.2	+	20013	226	1.44	0.998	0.139	0.013	0.998
0.8	+	18748	276	1.35	0.997	0.197	0.023	0.998
0.4	+	16283	369	1.17	0.994	0.369	0.080	0.994

[a]Acquired in the absence (-) or presence (+) of 40 mM $CaCl_2$.
[b]Globally fitted single ideal molecular weights from data acquired at 18,000, 21,000 and 25,000 rpm.
[c]Fitted molecular weight/theoretical monomeric molecular weight (i.e. 13,864 Da).
[d]Correlation coefficient from global fits.
[e]Globally fitted monomer-dimer equilibrium dissociation constants from data acquired at 18,000, 21,000 and 25,000 rpm.
SE, standard error.

3.4 Acidic patch mutations destabilize MCU_{72-189} similar to metal binding

To confirm that MCU_{72-189} destabilization induced by Ca^{2+} and Mg^{2+} is due to interactions with the acidic patch, I introduced D131R or D147R substitutions and evaluated the effects of $CaCl_2$ and $MgCl_2$ on thermal stability. Residue D131 is found within ~9.0 Å of D147 (i.e. Cγ) on the loop immediately after the β4 strand, with D147 adjacent to the C-terminal end of the α2 helix (Fig. 3.10A). Similar to the WT MCU_{72-189}, Mg^{2+} or Ca^{2+} binding to both MCU_{72-189} D131R and D147R did not appreciably alter secondary structure, as shown by minimal changes in far-UV CD ellipticity (Figure 3.20). Compared to the native protein with a T_m value of ~66°C, the D147R and D131R mutant proteins exhibited T_m values of ~61°C (~-5°C) and ~57°C (~-9°C), respectively. This indicates that, despite the loop-localization of the D147 and D131 residues, incorporation of a positively charged residue in the acidic patch markedly destabilizes the domain (Fig. 3.21). When MCU_{72-189} D147R was supplemented with 40 mM $MgCl_2$ or $CaCl_2$, the T_m value decreased by ~2°C. This smaller change is in contrast to the ~4°C and ~7°C destabilization observed for native MCU_{72-189} by $MgCl_2$ and $CaCl_2$, respectively (Fig. 3.21A; Table 4). Likewise, a smaller destabilization compared to native MCU_{72-189} was also observed for MCU_{72-189} D131R (i.e. ~-0°C and ~-3°C, respectively) (Fig. 3.21B; Table 4). Therefore, incorporating the MCU_{72-189} mutations in the acidic patch resulted in a domain destabilization (i.e. ΔT_m between ~-5 and -10°C), which is similar to the destabilization caused by Ca^{2+} and Mg^{2+} binding to native MCU_{72-189} (i.e. ΔT_m between ~-4 and -7°C). Furthermore, these mutations attenuated the effects of divalent cation binding on MCU_{72-189} stability. These data suggest that incorporation of a basic charge into the acidic patch via mutation destabilizes MCU_{72-189} similar to the binding of cations in this region and suppresses any further destabilization caused by interactions with Mg^{2+} or Ca^{2+}.

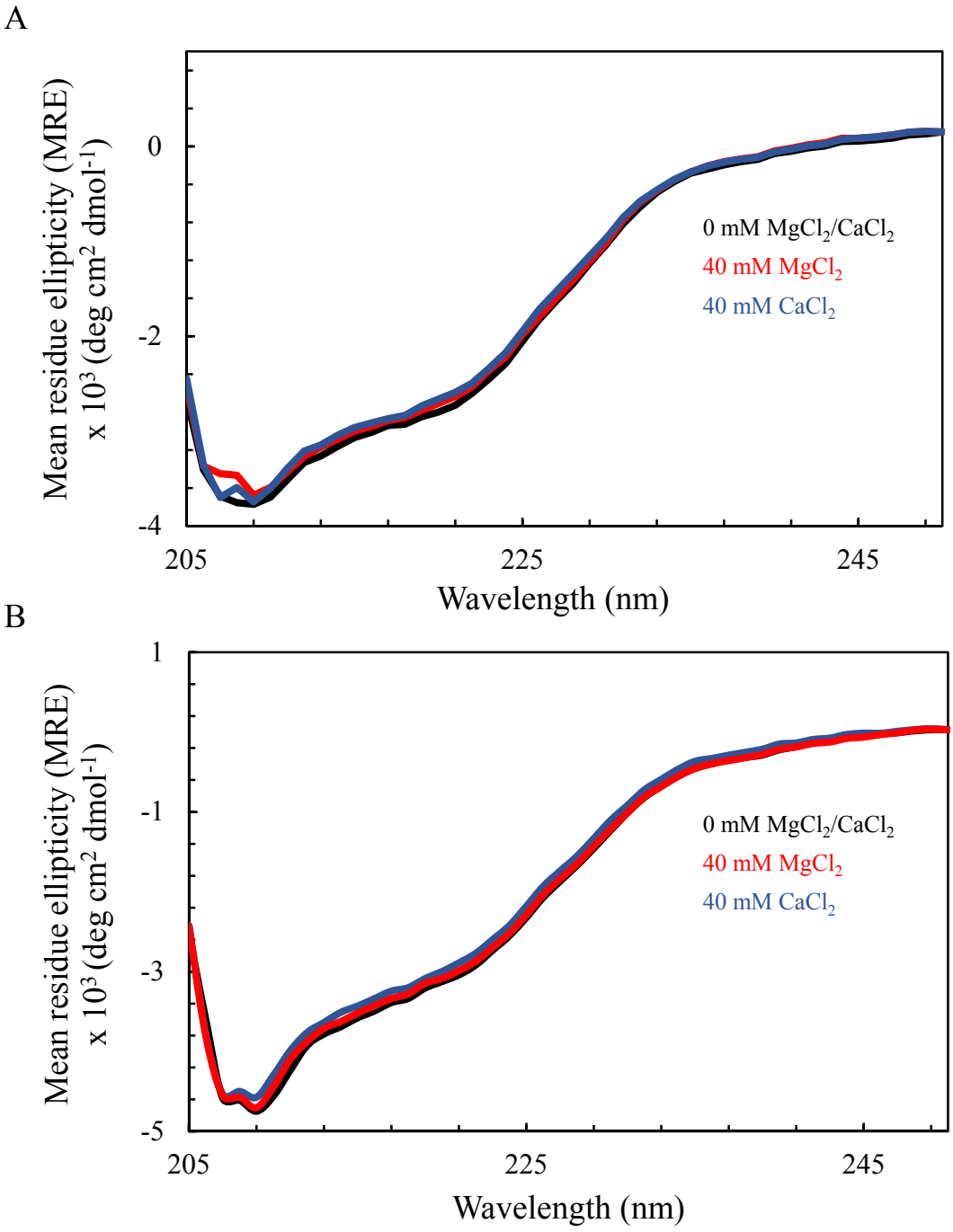

Figure 3.20. Secondary structure of MCU_{72-189} D131R and D147R. Effects of $MgCl_2$ and $CaCl_2$ on MCU_{72-189} D147R **(A)** and D131R **(B)** secondary structure. Shown are far-UV CD spectra in the absence (black line) and presence of 40 mM $MgCl_2$ (red line) or $CaCl_2$ (blue line) acquired at 4°C. Data is the average of three separate experiments (n=3) acquired using 0.5 mg mL^{-1} protein in 20 mM HEPES, 150 mM KCl, 2 mM DTT, pH 7.5.

A

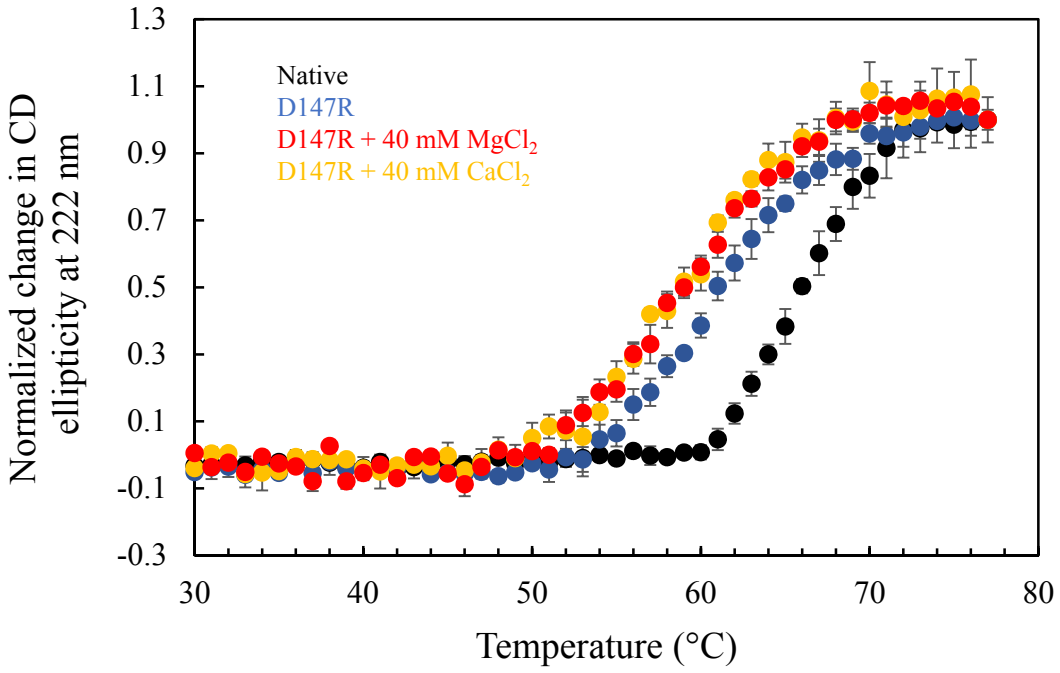
Native
D147R
D147R + 40 mM MgCl2
D147R + 40 mM CaCl2
Normalized change in CD ellipticity at 222 nm
Temperature (°C)
1.3
1.1
0.9
0.7
0.5
0.3
0.1
-0.1
-0.3
30
40
50
60
70
80

B

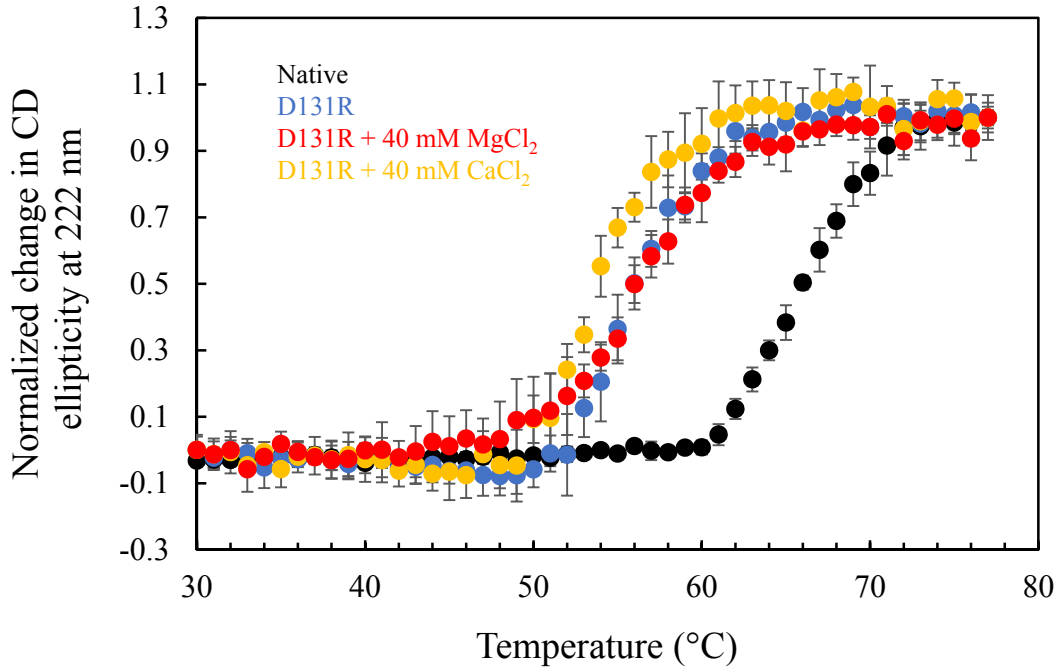
Native
D131R
D131R + 40 mM MgCl2
D131R + 40 mM CaCl2
Normalized change in CD ellipticity at 222 nm
Temperature (°C)
1.3
1.1
0.9
0.7
0.5
0.3
0.1
-0.1
-0.3
30
40
50
60
70
80

Figure 3.21. Stability of native MCU_{72-189}, MCU_{72-189} D131R and D147R. (A) Changes in far-UV CD ellipticity as a function of temperature for native MCU_{72-189} (black circles) and MCU_{72-189} D147R (blue circles) in the presence of 40 mM $MgCl_2$ (red circles) or 40 mM $CaCl_2$ (yellow circles). **(B)** Changes in far-UV CD ellipticity as a function of temperature for native MCU_{72-189} (black circles) and MCU_{72-189} D131R (blue circles) in the presence of 40 mM $MgCl_2$ (red circles) or 40 mM $CaCl_2$ (yellow circles). The control data are the same in both (A) and (B). Data were acquired together but are separated into (A) and (B) for clarity. Data is the average of three separate experiments (n=3) acquired using 0.5 mg mL^{-1} protein in 20 mM HEPES, 150 mM KCl, 2 mM DTT, pH 7.5. Error bars represent SEM.

Table 4. Stability of mutant and native MCU_{72-189} in the presence and absence of $MgCl_2$ or $CaCl_2$.

Protein	**$T_{m,apo}$[a] (°C)**	**SE**	**$T_{m,Mg2+}$[b] (°C)**	**SE**	**$T_{m,Ca2+}$[c] (°C)**	**SE**
Native	66.0	±0.02	62.0	±0.03	59.0	±0.04
D147R	61.0	±0.04	59.0	±0.04	59.0	±0.04
D131R	57.0	±0.05	57.0	±0.06	54.0	±0.09
Protein	**$\Delta T_{m,mutant}$[d] (°C)**	**SE[e]**	**$\Delta T_{m,Mg2+}$[f] (°C)**	**SE[e]**	**$\Delta T_{m,Ca2+}$[g] (°C)**	**SE[e]**
Native	N/A	N/A	-4.0	±0.04	-7.0	±0.04
D147R	-5.0	±0.04	-2.0	±0.06	-2.0	±0.06
D131R	-9.0	±0.05	0.0	±0.08	-3.0	±0.10

[a]Average of three separate thermal melts in the absence of $MgCl_2$ and $CaCl_2$ (i.e. apo).
[b]Average of three separate thermal melts in the presence of $MgCl_2$.
[c]Average of three separate thermal melts in the presence of $CaCl_2$.
[d]$T_{m,mutant(apo)}$-$T_{m,native(apo)}$.
[e]Propagated error.
[f]$T_{m,Mg2+}$-$T_{m,apo}$.
[g]$T_{m,Ca2+}$-$T_{m,apo}$.
SE, standard error.

3.5 Mutation in the MCU_{72-189} acidic patch attenuates Ca^{2+}-dependent monomerization

In addition to AUC, I also performed SEC-MALS to assess the quaternary structure of MCU_{72-189} and to confirm the tendency for MCU_{72-189} dimerization. The protein eluted as a single major peak on a Superdex 200 10/300 GL column with an apparent MW of ~24.6 kDa, equal to 1.77× the theoretical 13.9 kDa monomeric mass (Fig. 3.22, Table 5). Given the globular structure of MCU_{72-189}, this data suggests the presence of a monomer-dimer equilibrium in fast exchange, consistent with the AUC data. When SEC-MALS was performed in the presence of 40 mM $CaCl_2$, the apparent MW of MCU_{72-189} was ~17.9 kDa, equal to 1.29× the theoretical monomeric mass (Fig 3.22, Table 5). Therefore, consistent with the AUC findings, the SEC-MALS data show a shift in the monomer-dimer equilibrium of MCU_{72-189} toward monomer in the presence of $CaCl_2$.

With residue D147 being one of the major contributors to the formation of the contiguous acidic patch, I introduced a D147R substitution and assessed its effects on MCU_{72-189} quaternary structure by SEC-MALS. The protein eluted as a single major peak on a Superdex 200 10/300 GL column with an apparent MW of ~16.0 kDa, equal to 1.15× the theoretical monomeric mass of ~13.9 kDa (Fig 3.22, Table 5). SEC-MALS of MCU_{72-189} D147R in the presence of 40 mM $CaCl_2$ revealed an apparent MW of ~15.8 kDa, 1.14× the theoretical monomeric mass of ~13.9 kDa (Fig 3.22, Table 5). Therefore, with the incorporation of the D147R mutation, the monomer-dimer equilibrium of MCU_{72-189} is persistently shifted toward monomer. Consistent with the constitutive monomeric state, $CaCl_2$ has minimal effect on the oligomerization state.

Taken together, the AUC and SEC-MALS data demonstrate that MCU_{72-189} exists in a monomer-dimer equilibrium with sub-mM affinity undergoing fast exchange. Importantly, $CaCl_2$ weakens MCU_{72-189} self-association by ~2-3 fold, and disruption of the acidic patch by mutation promotes monomerization similar to cation binding.

A

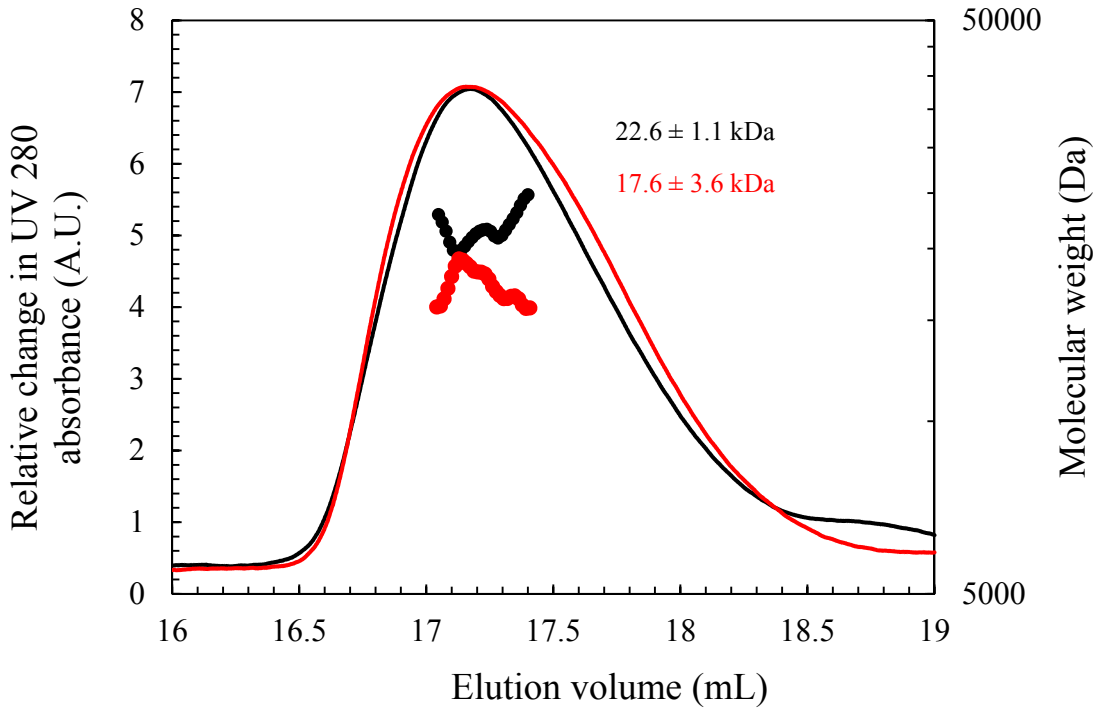
22.6 ± 1.1 kDa
17.6 ± 3.6 kDa
Relative change in UV 280 absorbance (A.U.)
Molecular weight (Da)
Elution volume (mL)
0
1
2
3
4
5
6
7
8
5000
50000
16
16.5
17
17.5
18
18.5
19

B

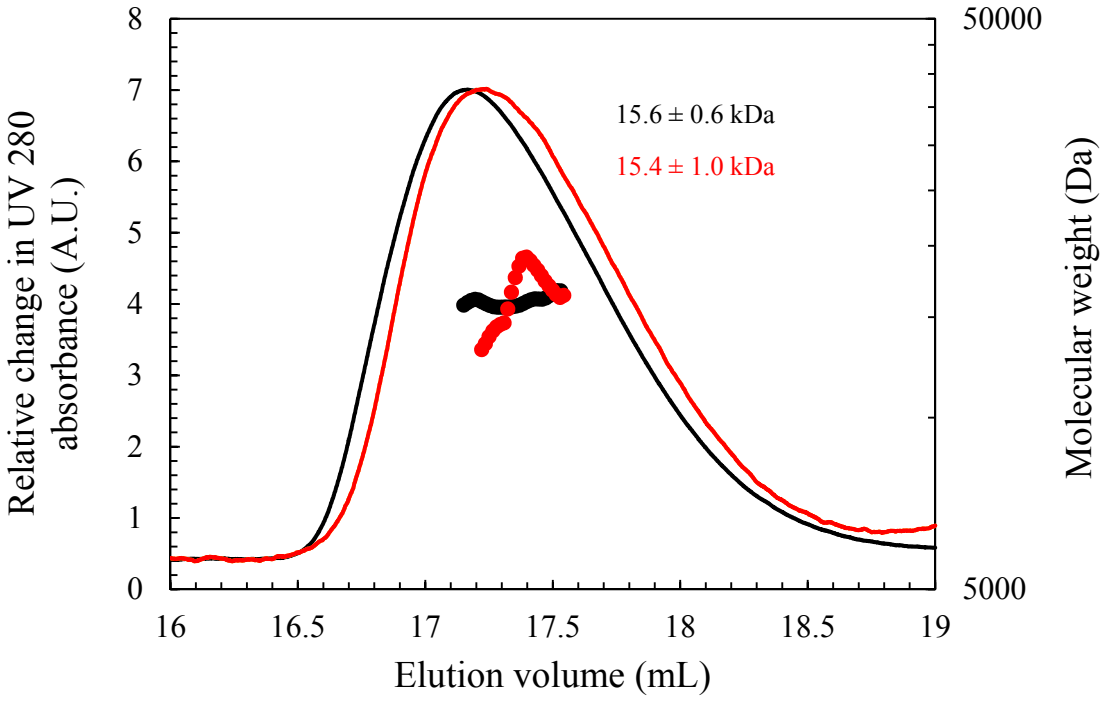
15.6 ± 0.6 kDa
15.4 ± 1.0 kDa
Relative change in UV 280 absorbance (A.U.)
Molecular weight (Da)
Elution volume (mL)
0
1
2
3
4
5
6
7
8
5000
50000
16
16.5
17
17.5
18
18.5
19

Figure 3.22. SEC-MALS analysis of MCU_{72-189} and MCU_{72-189} D147R. Relative changes in UV 280 absorbance and MW (Da) of native MCU_{72-189} **(A)** and MCU_{72-189} D147R **(B)** are plotted as a function of elution volume (mL). Shown are their respective peaks in the absence of $CaCl_2$ (black line) and in the presence of $CaCl_2$ (red line). Over the peak region, the MW of the species in the absence of $CaCl_2$ (black circles) and in the presence of $CaCl_2$ (red circles) is calculated from the light scattering measurements. The MW of each peak is shown on the right of each peak with SE. Data are representative of three separate experiments (n=3) for each plot, acquired using 2.0 mg mL^{-1} protein in 20 mM HEPES, 150 mM KCl, 0.5 mM DTT, pH 7.5.

Table 5. Ca^{2+} dependence of MCU_{72-189} and MCU_{72-189} D147R MWs measured by SEC-MALS.

Protein	Repetition	$CaCl_2$[a]	MW (kDa)[b]	SE	Stoichiometry[c]
Native MCU_{72-189}	1	-	21.8	0.7	1.57
	2	-	29.4	1.7	2.12
	3	-	22.6	1.1	1.63
	Average	-	24.6	1.2	1.77
Native MCU_{72-189}	1	+	15.8	2.3	1.14
	2	+	17.6	3.6	1.27
	3	+	20.2	1.9	1.45
	Average	+	17.9	2.6	1.29
MCU_{72-189} D147R	1	-	15.9	1.1	1.14
	2	-	15.6	0.6	1.12
	3	-	16.4	0.7	1.18
	Average	-	16.0	0.8	1.15
MCU_{72-189} D147R	1	+	16.8	2.2	1.21
	2	+	15.4	1.0	1.11
	3	+	15.2	0.7	1.09
	Average	+	15.8	1.3	1.14

[a]Acquired in the absence (-) or presence (+) of 40 mM $CaCl_2$.
[b]Molecular weights calculated from ASTRA software v.6.1.5.22 (Wyatt Technologies).
[c]Fitted molecular weight/theoretical monomeric molecular weight (i.e. 13.9 kDa).
SE, standard error.

Altogether, I have discovered that MCU contains a conserved β-grasp-like matrix domain that weakly interacts with the divalent cations Mg^{2+} and Ca^{2+}. Furthermore, Ca^{2+} not only promotes MCU_{72-189} monomerization, but also weakens its tendency to self-associate. D131R and D147R mutations in the acidic patch destabilize MCU_{72-189} similar to metal binding and also attenuate the sensitivity of stability to the presence of Mg^{2+} and Ca^{2+}. Lastly, incorporation of a D147R mutation in the cation binding region induces monomerization of MCU_{72-189} even in the absence of Ca^{2+}.

Chapter 4

Discussion

4.1 Significance of the MCU_{72-189} β-grasp-like fold

Proteins that adopt β-grasp folds such as ubiquitin are known to be involved in a diverse range of biochemical functions, such as providing a scaffold for different enzymatic active sites, assembly of macromolecular complexes and also for post-translational protein modification (Burroughs *et al.*, 2007). Furthermore, they are known to interact with nucleic acids, proteins and metal ions (Burroughs *et al.*, 2007; Burroughs *et al.*, 2012). In fact, the eukaryotic ubiquitin superfamily has diversified into at least 67 distinct families (Burroughs *et al.*, 2007). Therefore, given the large structural diversity of β-grasp proteins, the variations observed for the β-grasp-like fold of MCU_{72-189} are not surprising. β-grasp proteins can include as many as ten or as few as three β-strands and up to three α-helices with the central α-helix crossing in either direction (Burroughs *et al.*, 2007; Burroughs *et al.*, 2012). For example, the streptococcal immunoglobulin-binding protein G and the staphylococcal enterotoxin B are dominated by a β-sheet with five anti-parallel β-strands and a single helical segment (Kraulis, 1991; Murzin *et al.*, 1995). With regards to MCU_{72-189}, I have found that its β-grasp-like fold not only plays a role as a protein-interaction domain through self-association tendencies, but also has an intrinsic ability to bind the divalent cations Ca^{2+} and Mg^{2+}. Interestingly, this N-terminal region of MCU was also recently shown by co-immunoprecipitation assays to associate with MCUR1, an important MCU regulator (Lee *et al.*, 2015).

4.2 Differences between MCU_{72-189} and MCU_{75-185} (Lee et al., 2015)

While I was performing structural-rationalized mutations based on my own crystal structures discussed in this thesis, a structural study on MCU residues 75-185 was published, showing a similar overall fold to my MCU_{72-189} protein (Figure 4.1). However, despite the similarities of the fold, there are two prominent differences. First, my MCU_{72-189} protein shows a dynamic C-terminal tail (i.e. residues 168-189) that cannot be modeled in the electron density. Lee et al., (Lee *et al.*, 2015) found that the position of this C-terminus region (i.e. residues 166-185) can be stabilized by a tetraethylene glycol molecule, revealing a third α-helix close to α2 (Figure 4.1). Considering the mobility of the

C-terminal tail and its close proximity to the MCU acidic patch, residues 168-189 could act as a dynamic cap, involved in regulating the accessibility of cations and/or other larger molecules. The second difference involves the formation of the R93:E95 salt bridge. Although this salt bridge may stabilize the conformation of L2, it appears to be less favorable in the Lee et al., (Lee *et al.*, 2015) structure (i.e. NH1:Oε distances of 2.9 Å in the present work versus 5.1 Å) (Figure 4.1). It is interesting that S92 is a proposed phosphorylation site very close to the salt bridge found in my structure, and its mutation results in suppression of MCU activity (Lee *et al.*, 2015). Phosphorylation of S92 is important as it induces conformational changes by breaking the hydrogen bonds in the L2 and L4 loops and modulating MCU function (Joiner *et al.*, 2012; Lee *et al.*, 2015; Settimo *et al.*, 2007). Therefore, the R93:E95 salt bridge may play an important role in regulating the phosphorylation event that modulates MCU function.

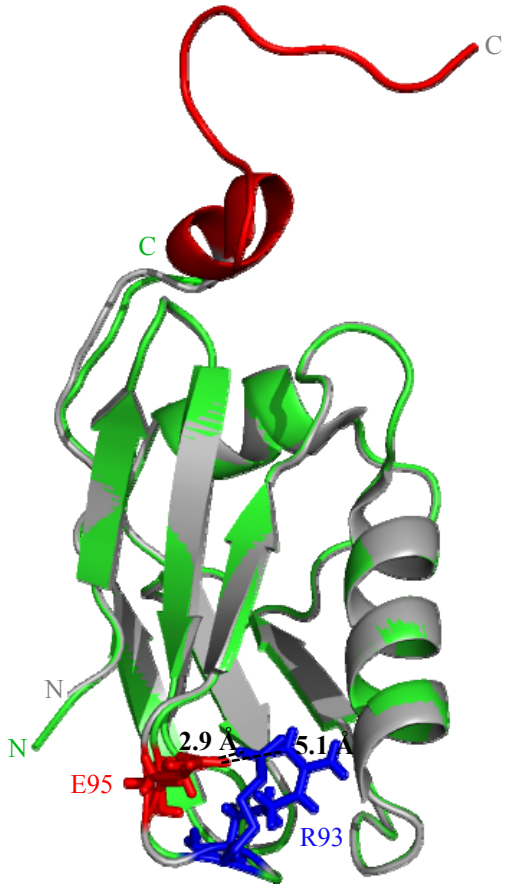

Figure 4.1. Ribbon view of the backbone alignments of MCU_{72-189} solved in the presence of $MgCl_2$ (green) and MCU_{75-185} (4XTB.pdb). The additional C-terminal helix (α3) stabilized by tetraethylene glycol in the MCU_{75-185} structure is shown in red. The differences in the L2 salt bridge residue orientation are highlighted with R93 residues (blue sticks) and E95 residues (red sticks). The salt bridge was identified using ESBRI (Costantini *et al.*, 2008), but not by the online tool used for the MCU_{75-185} structure (Lee *et al.*, 2015). The distance between the R93 and E95 residues for MCU_{72-189} is 2.9 Å, whereas the distance between the R93 and E95 residues for MCU_{75-185} is 5.1 Å. Structural alignments were performed with Theseus (Theobald & Wuttke, 2008) between residues 75-167, common to both structures.

4.3 Significance of MCU *in vitro* and *in vivo* data

In vitro, the MCU_{72-189} matrix region binds the divalent cations Ca^{2+} and Mg^{2+} with ~mM binding affinity in the acidic patch. Interestingly, Mg^{2+} is the most abundant intracellular divalent cation, with cytosolic and nuclear concentrations maintained in the mM range (Romani *et al.*, 1993; Szanda *et al.*, 2009). Mg^{2+} is known to enter the mitochondria electrogenically through a high conductance Mg^{2+} channel known as the Mrs2p channel; therefore, alterations in the mitochondrial membrane potential can modulate Mrs2p-mediated Mg^{2+} uptake (Kolisek *et al.*, 2003; Schindl *et al.*, 2007; Zsurka *et al.*, 2001). It is also known that varying concentrations of PO_4^{3-}, ADP and ATP can alter the free Mg^{2+} concentration in the mitochondrial matrix, which is ~0.5-1.5 mM (Gout *et al.*, 2014; Jung *et al.*, 1990; Rutter *et al.*, 1990). Therefore, under physiological conditions with saturation levels dependent on the metabolic state of the cell, a large fraction of MCU molecules could bind Mg^{2+}. Additionally, Mg^{2+} is able to inhibit mitochondrial Ca^{2+} uptake (Favaron & Bernardi, 1985; Jacobus *et al.*, 1975; Prentki *et al.*, 1983; Szanda *et al.*, 2009), which can even occur after elevations in cytosolic Mg^{2+} (Crompton *et al.*, 1976; Saris *et al.*, 2000; Szanda *et al.*, 2009). Consistent with this notion, it has also been found that matrix Mg^{2+} inhibits swelling and uncoupling of mitochondria associated with opening of the mPTP caused by Ca^{2+} uptake during cell death (Bernardi *et al.*, 1993; Novgorodov *et al.*, 1994; Saris *et al.*, 2000; Zoratti & Szabo, 1995).

Although it is unlikely for global free Ca^{2+} levels to approach mM levels in the matrix, the charge difference between the inside and outside of the matrix (-180 mV) is a massive driving force for cations, which would reach mM levels if allowed to freely equilibrate. Therefore, the highly negative mitochondrial membrane potential is the driving force responsible for establishing Ca^{2+} levels within the mitochondrial matrix. According to the diffusion theory, local Ca^{2+} levels would be in the mM range at the immediate base of the channel pore (Bauer, 2001; Chad & Eckert, 1984; Simon & Llinas, 1985) and ~0.1 mM at a distance of ~10 nm from the exiting region (Tadross *et al.*, 2013). Therefore, the Ca^{2+} binding ability of MCU_{72-189} will be dependent on its proximity to the open pore. Interestingly, it has been shown that sustained cytosolic Ca^{2+} levels inactivate the mitochondrial Ca^{2+} uptake pathway (Moreau *et al.*, 2006).

To complement my *in vitro* studies, the Muniswamy Madesh group (Department of Medicine, Temple University) performed functional studies on MCU in live HEK293T cells. I have included this complementary work in the appendix of my thesis since the mutations and rationale for these studies were based on my *in vitro* work described in this thesis. The Madesh group observed that elevation of matrix Ca^{2+} inhibits the MCU-dependent Ca^{2+} uptake rate without changes in the normal mitochondrial membrane potential levels (App Fig. 1). The destabilization of MCU_{72-189} induced by Ca^{2+} binding may be an important contributor to this inhibition and may be a protective buffering mechanism to prevent cell death or damage induced by mitochondrial Ca^{2+} overload (Giorgi *et al.*, 2012). Further work by Muniswamy also revealed that D131A, D131R, D147A and D147R substitutions attenuate Ca^{2+} uptake in live cells compared to native MCU, without significant differences in the mitochondrial membrane potential (App Fig. 2-4). Specifically, HeLa cells overexpressing WT MCU showed a significantly increased maximal mitochondrial Ca^{2+} uptake compared to empty vector transfected cells. On the other hand, each of the mutants mentioned showed significantly reduced mitochondrial Ca^{2+} uptake compared to endogenous MCU (i.e. D131A, D131R, D147A) and WT MCU overexpression (i.e. D131A, D131R, D147A, D147R), hence revealing a dominant-negative effect for some of the mutants (App Fig. 2). HeLa cells expressing WT MCU showed a significant decrease in agonist-induced cytosolic Ca^{2+} levels compared to empty vector cells and all the mutants (App Fig. 4).

Taken together, my *in vitro* data complemented by the Madesh group live cell data reveal that MCU can be self-regulated by mitochondrial Ca^{2+} and Mg^{2+} levels. I have shown that when MCU_{72-189} binds Ca^{2+} or Mg^{2+}, the protein is destabilized and its self-association equilibrium is shifted toward monomer. These divalent cations bind on a distinct, acidic patch, in which its mutation destabilizes MCU_{72-189} similar to cation binding and decreases its sensitivity to Ca^{2+} and Mg^{2+}. Additionally, incorporation of mutations in the acidic patch causes monomerization and can attenuate MCU uptake in live cells in a dominant-negative manner. Based on these observations, I propose a model of regulation in which MCU activity is inhibited upon Mg^{2+} and/or Ca^{2+} binding to the MCU soluble matrix domain via a destabilization that is associated with a suppression in self-association (Figure 4.2). In the biological context, the metabolic state of the cell and the varying amounts of PO_4^{3-}, ADP

and ATP would modulate MCU activity. Additionally, the Mrs2p activity would also modulate MCU activity, where increased free Mg^{2+} would inhibit MCU activity. An open MCU pore resulting in high Ca^{2+} levels (i.e. ~mM) within nanodomains in close proximity to $MCU_{72\text{-}189}$ would also inhibit MCU activity in a negative feedback mechanism.

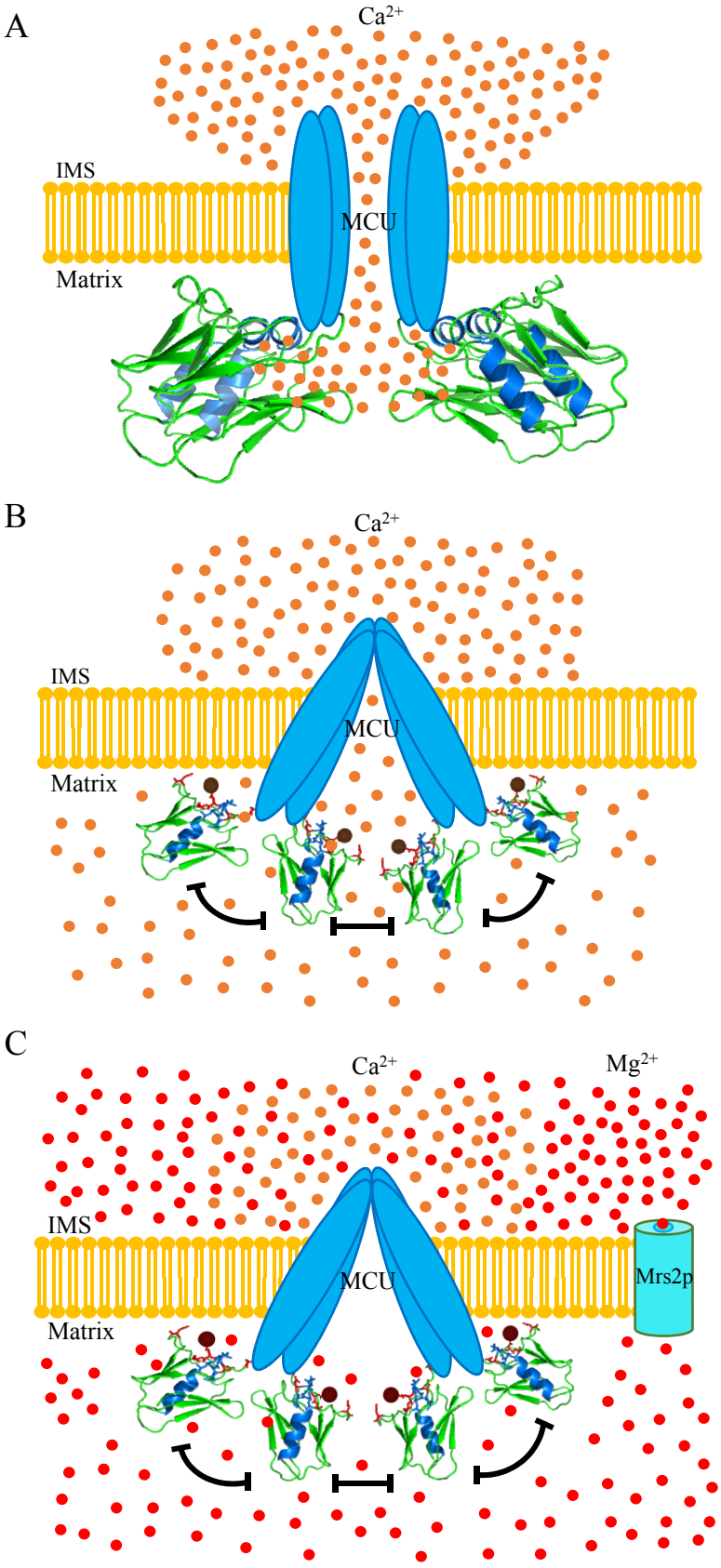
A
Ca2+
IMS
MCU
Matrix
B
Ca2+
IMS
MCU
Matrix
C
Ca2+
Mg2+
IMS
MCU
Mrs2p
Matrix

Figure 4.2. Model of MCU autoregulation by Mg^{2+} and Ca^{2+}. (A) MCU channel activation by increased IMS Ca^{2+} levels. The dimerized MCU_{72-189} domain on the matrix side of the channel is shown in ribbon view. **(B)** Feedback-inhibited MCU channel due to self-association disruption by high Ca^{2+} levels in nanodomains close to the channel pore. **(C)** Inhibited MCU channel due to increased free Mg^{2+} levels entering the matrix through the Mrs2p channel. Mg^{2+} and Ca^{2+} are depicted as red and orange spheres, respectively. Note that in (a) – (c), the precise stoichiometry of the channel is not known, and known protein regulators that directly or indirectly interact with MCU have been omitted for simplicity. In (b) – (c), the dimerized MCU_{72-189} ribbon structures are reduced to fit illustrations.

4.4 Contrasting perspectives on MCU function and regulation

Recently, a paper that talks about matrix Ca^{2+} inhibiting MCU activity via EMRE has been published (Vais *et al.*, 2016). This proposed mechanism may be different than the regulatory mechanism I am proposing, since my data suggests that Ca^{2+} binds directly to MCU to inhibit its activity, whereas this paper states that inhibition of MCU activity by Ca^{2+} is mediated by EMRE (Vais *et al.*, 2016). It is important to note that the orientation of EMRE described in this paper is different from the orientation of EMRE described in many other recent papers. Vais et al., (Vais *et al.*, 2016) state that the C-terminal of EMRE is localized in the mitochondrial matrix, whereas other papers have stated that the C-terminal of EMRE is localized in the IMS (Pendin *et al.*, 2014; Sancak *et al.*, 2013; Tomar *et al.*, 2016; Tsai *et al.*, 2016; Yamamoto *et al.*, 2016). Clearly, further studies need to be done to have a better understanding of EMRE orientation and how it may be regulating MCU.

A separate group also had a paper recently published which describes a low resolution solution nuclear magnetic resonance spectroscopy and EM structure of the pore domain of MCU (Oxenoid *et al.*, 2016). This paper states that MCU in the closed state oligomerizes as a pentamer (Oxenoid *et al.*, 2016). However, I believe that the pentamer is suspect in this paper for two important reasons. First, when calculating the MW of MCU via SEC-MALS, they did not account for the bound micelle, hence overestimating the calculated MW of MCU (Oxenoid *et al.*, 2016). Second, the chemical crosslinking [i.e. using 3,3'-dithiobis (sulfosuccinimidyl propionate)] and SDS-PAGE approach they used to further characterize the MCU oligomerization state is highly ambiguous (Oxenoid *et al.*, 2016). Specifically, when visualizing the gel, the pentamer band shows little intensity whereas the monomer and dimer bands have the strongest intensity (i.e. ~75% of the intensity) (Oxenoid *et al.*, 2016), indicating that most of MCU is oligomerized as monomer and dimer, consistent with my data. Therefore, I am skeptical of the notion that MCU oligomerizes as a pentamer. However, the work does suggest a role for the C-terminal domain in MCU oligomerization, and clearly, further structural work is required on the full-length molecule to reveal the precise functional MCU oligomerization state.

4.5 Conclusion

In conclusion, my structural and *in vitro* data of MCU_{72-189} suggest that MCU is autoregulated by Ca^{2+} and/or Mg^{2+} that bind to an acidic patch, destabilizing the self-association of the soluble matrix region of MCU. In fact, this regulatory model is consistent with a recent study that showed inhibition of MCU by Mg^{2+} (Blomeyer *et al.*, 2016), as well as a study that showed Ca^{2+}-dependent inactivation of mitochondrial Ca^{2+} uptake (Moreau *et al.*, 2006). However, further work needs to be done to determine if the acidic patch is involved in modulating MCU activity through protein-protein interactions. Future structural studies would involve the associated regulators of MCU (Section 1.7) to expand our knowledge on the function and modulation of MCU activity. Important structural studies would involve performing pull-down experiments, nuclear magnetic resonance or intrinsic fluorescence to evaluate the interactions between MCU and the MICU1 domains, as well as the EMRE domains. Since there has been debate over the interactions of MICU1 and EMRE with MCU (Foskett & Madesh, 2014; Perocchi *et al.*, 2010; Sancak *et al.*, 2013), these interactions could be tested to help further clarify the interactive role of MICU1 and EMRE in modulating MCU function. Nonetheless, my findings provide new mechanistic insights into MCU regulation and lay the foundation to the future design of MCU inhibitors to control cell death and treat a range of Ca^{2+}-related pathological processes.

References

1. Adams, P. D., Afonine, P. V., Bunkoczi, G., Chen, V. B., Davis, I. W., Echols, N., Headd, J. J., Hung, L. W., Kapral, G. J., Grosse-Kunstleve, R. W., McCoy, A. J., Moriarty, N. W., Oeffner, R., Read, R. J., Richardson, D. C., Richardson, J. S., Terwilliger, T. C. & Zwart, P. H. (2010). PHENIX: a comprehensive Python-based system for macromolecular structure solution. *Acta Crystallogr D Biol Crystallogr* **66**, 213-21.

2. Baines, C. P. (2009). The molecular composition of the mitochondrial permeability transition pore. *J Mol Cell Cardiol* **46**, 850-7.

3. Baines, C. P., Kaiser, R. A., Purcell, N. H., Blair, N. S., Osinska, H., Hambleton, M. A., Brunskill, E. W., Sayen, M. R., Gottlieb, R. A., Dorn, G. W., Robbins, J. & Molkentin, J. D. (2005). Loss of cyclophilin D reveals a critical role for mitochondrial permeability transition in cell death. *Nature* **434**, 658-62.

4. Battye, T. G., Kontogiannis, L., Johnson, O., Powell, H. R. & Leslie, A. G. (2011). iMOSFLM: a new graphical interface for diffraction-image processing with MOSFLM. *Acta Crystallogr D Biol Crystallogr* **67**, 271-81.

5. Bauer, P. J. (2001). The local Ca concentration profile in the vicinity of a Ca channel. *Cell Biochem Biophys* **35**, 49-61.

6. Baughman, J. M., Perocchi, F., Girgis, H. S., Plovanich, M., Belcher-Timme, C. A., Sancak, Y., Bao, X. R., Strittmatter, L., Goldberger, O., Bogorad, R. L., Koteliansky, V. & Mootha, V. K. (2011). Integrative genomics identifies MCU as an essential component of the mitochondrial calcium uniporter. *Nature* **476**, 341-5.

7. Becker, G. L., Fiskum, G. & Lehninger, A. L. (1980). Regulation of free Ca2+ by liver mitochondria and endoplasmic reticulum. *J Biol Chem* **255**, 9009-12.

8. Bernardi, P., Veronese, P. & Petronilli, V. (1993). Modulation of the mitochondrial cyclosporin A-sensitive permeability transition pore. I. Evidence for two separate Me2+ binding sites with opposing effects on the pore open probability. *J Biol Chem* **268**, 1005-10.

9. Bertolino, M. & Llinas, R. R. (1992). The central role of voltage-activated and receptor-operated calcium channels in neuronal cells. *Annu Rev Pharmacol Toxicol* **32**, 399-421.

10. Bezprozvanny, I., Watras, J. & Ehrlich, B. E. (1991). Bell-shaped calcium-response curves of Ins(1,4,5)P3- and calcium-gated channels from endoplasmic reticulum of cerebellum. *Nature* **351**, 751-4.

11. Blomeyer, C. A., Bazil, J. N., Stowe, D. F., Dash, R. K. & Camara, A. K. (2016). Mg differentially regulates two modes of mitochondrial Ca uptake in isolated cardiac mitochondria: implications for mitochondrial Ca sequestration. *J Bioenerg Biomembr*.

12. Boczek, T., Lisek, M., Ferenc, B., Kowalski, A., Stepinski, D., Wiktorska, M. & Zylinska, L. (2014). Plasma membrane Ca2+-ATPase isoforms composition regulates cellular pH homeostasis in differentiating PC12 cells in a manner dependent on cytosolic Ca2+ elevations. *PLoS One* **9**, e102352.

13. Burroughs, A. M., Balaji, S., Iyer, L. M. & Aravind, L. (2007). Small but versatile: the extraordinary functional and structural diversity of the beta-grasp fold. *Biol Direct* **2**, 18.

14. Burroughs, A. M., Iyer, L. M. & Aravind, L. (2012). Structure and evolution of ubiquitin and ubiquitin-related domains. *Methods Mol Biol* **832**, 15-63.

15. Calvo, S. E., Clauser, K. R. & Mootha, V. K. (2016). MitoCarta2.0: an updated inventory of mammalian mitochondrial proteins. *Nucleic Acids Res* **44**, D1251-7.

16. Carafoli, E. (2003). Historical review: mitochondria and calcium: ups and downs of an unusual relationship. *Trends Biochem Sci* **28**, 175-81.

17. Cavallo, L., Kleinjung, J. & Fraternali, F. (2003). POPS: A fast algorithm for solvent accessible surface areas at atomic and residue level. *Nucleic Acids Res* **31**, 3364-6.

18. Chad, J. E. & Eckert, R. (1984). Calcium domains associated with individual channels can account for anomalous voltage relations of CA-dependent responses. *Biophys J* **45**, 993-9.

19. Chaudhuri, D., Artiga, D. J., Abiria, S. A. & Clapham, D. E. (2016). Mitochondrial calcium uniporter regulator 1 (MCUR1) regulates the calcium threshold for the mitochondrial permeability transition. *Proc Natl Acad Sci U S A* **113**, E1872-80.

20. Clapham, D. E. (2007). Calcium signaling. *Cell* **131**, 1047-58.

21. Clementi, E. & Meldolesi, J. (1996). Pharmacological and functional properties of voltage-independent Ca2+ channels. *Cell Calcium* **19**, 269-79.

22. Costantini, S., Colonna, G. & Facchiano, A. M. (2008). ESBRI: a web server for evaluating salt bridges in proteins. *Bioinformation* **3**, 137-8.

23. Crompton, M., Capano, M. & Carafoli, E. (1976). Respiration-dependent efflux of magnesium ions from heart mitochondria. *Biochem J* **154**, 735-42.

24. Csordas, G., Golenar, T., Seifert, E. L., Kamer, K. J., Sancak, Y., Perocchi, F., Moffat, C., Weaver, D., de la Fuente Perez, S., Bogorad, R., Koteliansky, V., Adijanto, J., Mootha, V. K. & Hajnoczky, G. (2013). MICU1 controls both the threshold and cooperative activation of the mitochondrial Ca(2)(+) uniporter. *Cell Metab* **17**, 976-87.

25. de Brito, O. M. & Scorrano, L. (2008). Mitofusin 2 tethers endoplasmic reticulum to mitochondria. *Nature* **456**, 605-10.

26. De Stefani, D., Patron, M. & Rizzuto, R. (2015). Structure and function of the mitochondrial calcium uniporter complex. *Biochim Biophys Acta* **1853**, 2006-11.

27. De Stefani, D., Raffaello, A., Teardo, E., Szabo, I. & Rizzuto, R. (2011). A forty-kilodalton protein of the inner membrane is the mitochondrial calcium uniporter. *Nature* **476**, 336-40.

28. Deluca, H. F. & Engstrom, G. W. (1961). Calcium uptake by rat kidney mitochondria. *Proc Natl Acad Sci U S A* **47**, 1744-50.

29. Denton, R. M. (2009). Regulation of mitochondrial dehydrogenases by calcium ions. *Biochim Biophys Acta* **1787**, 1309-16.

30. Di Lisa, F., Carpi, A., Giorgio, V. & Bernardi, P. (2011). The mitochondrial permeability transition pore and cyclophilin D in cardioprotection. *Biochim Biophys Acta* **1813**, 1316-22.

31. Dorn, G. W., 2nd & Scorrano, L. (2010). Two close, too close: sarcoplasmic reticulum-mitochondrial crosstalk and cardiomyocyte fate. *Circ Res* **107**, 689-99.

32. Emanuelsson, O., Nielsen, H., Brunak, S. & von Heijne, G. (2000). Predicting subcellular localization of proteins based on their N-terminal amino acid sequence. *J Mol Biol* **300**, 1005-16.

33. Emsley, P., Lohkamp, B., Scott, W. G. & Cowtan, K. (2010). Features and development of Coot. *Acta Crystallogr D Biol Crystallogr* **66**, 486-501.

34. Favaron, M. & Bernardi, P. (1985). Tissue-specific modulation of the mitochondrial calcium uniporter by magnesium ions. *FEBS Lett* **183**, 260-4.

35. Fieni, F., Lee, S. B., Jan, Y. N. & Kirichok, Y. (2012). Activity of the mitochondrial calcium uniporter varies greatly between tissues. *Nat Commun* **3**, 1317.

36. Filipowicz, W., Bhattacharyya, S. N. & Sonenberg, N. (2008). Mechanisms of post-transcriptional regulation by microRNAs: are the answers in sight? *Nat Rev Genet* **9**, 102-14.

37. Foskett, J. K. & Madesh, M. (2014). Regulation of the mitochondrial Ca(2+) uniporter by MICU1 and MICU2. *Biochem Biophys Res Commun* **449**, 377-83.

38. Giacomello, M., Drago, I., Bortolozzi, M., Scorzeto, M., Gianelle, A., Pizzo, P. & Pozzan, T. (2010). Ca2+ hot spots on the mitochondrial surface are generated by Ca2+ mobilization from stores, but not by activation of store-operated Ca2+ channels. *Mol Cell* **38**, 280-90.

39. Giorgi, C., Baldassari, F., Bononi, A., Bonora, M., De Marchi, E., Marchi, S., Missiroli, S., Patergnani, S., Rimessi, A., Suski, J. M., Wieckowski, M. R. & Pinton, P. (2012). Mitochondrial Ca(2+) and apoptosis. *Cell Calcium* **52**, 36-43.

40. Glancy, B. & Balaban, R. S. (2012). Role of mitochondrial Ca2+ in the regulation of cellular energetics. *Biochemistry* **51**, 2959-73.

41. Gout, E., Rebeille, F., Douce, R. & Bligny, R. (2014). Interplay of Mg2+, ADP, and ATP in the cytosol and mitochondria: unravelling the role of Mg2+ in cell respiration. *Proc Natl Acad Sci U S A* **111**, E4560-7.

42. Griffiths, E. J. & Halestrap, A. P. (1993). Protection by Cyclosporin A of ischemia/reperfusion-induced damage in isolated rat hearts. *J Mol Cell Cardiol* **25**, 1461-9.

43. Hajnoczky, G., Csordas, G., Madesh, M. & Pacher, P. (2000a). Control of apoptosis by IP(3) and ryanodine receptor driven calcium signals. *Cell Calcium* **28**, 349-63.

44. Hajnoczky, G., Csordas, G., Madesh, M. & Pacher, P. (2000b). The machinery of local Ca2+ signalling between sarco-endoplasmic reticulum and mitochondria. *J Physiol* **529 Pt 1**, 69-81.

45. Hajnoczky, G., Csordas, G. & Yi, M. (2002). Old players in a new role: mitochondria-associated membranes, VDAC, and ryanodine receptors as contributors to calcium signal propagation from endoplasmic reticulum to the mitochondria. *Cell Calcium* **32**, 363-77.

46. Hajnoczky, G., Robb-Gaspers, L. D., Seitz, M. B. & Thomas, A. P. (1995). Decoding of cytosolic calcium oscillations in the mitochondria. *Cell* **82**, 415-24.

47. Halestrap, A. P. (2009). What is the mitochondrial permeability transition pore? *J Mol Cell Cardiol* **46**, 821-31.

48. Harrington, J. L. & Murphy, E. (2015). The mitochondrial calcium uniporter: mice can live and die without it. *J Mol Cell Cardiol* **78**, 46-53.

49. Hoffman, N. E., Chandramoorthy, H. C., Shamugapriya, S., Zhang, X., Rajan, S., Mallilankaraman, K., Gandhirajan, R. K., Vagnozzi, R. J., Ferrer, L. M., Sreekrishnanilayam, K., Natarajaseenivasan, K., Vallem, S., Force, T., Choi, E. T., Cheung, J. Y. & Madesh, M. (2013). MICU1 motifs define mitochondrial calcium uniporter binding and activity. *Cell Rep* **5**, 1576-88.

50. Holm, L. & Rosenstrom, P. (2010). Dali server: conservation mapping in 3D. *Nucleic Acids Res* **38**, W545-9.

51. Hoth, M. & Penner, R. (1993). Calcium release-activated calcium current in rat mast cells. *J Physiol* **465**, 359-86.

52. Hunter, D. R., Haworth, R. A. & Southard, J. H. (1976). Relationship between configuration, function, and permeability in calcium-treated mitochondria. *J Biol Chem* **251**, 5069-77.

53. Jacobus, W. E., Tiozzo, R., Lugli, G., Lehninger, A. L. & Carafoli, E. (1975). Aspects of energy-linked calcium accumulation by rat heart mitochondria. *J Biol Chem* **250**, 7863-70.

54. Jambrina, E., Alonso, R., Alcalde, M., del Carmen Rodriguez, M., Serrano, A., Martinez, A. C., Garcia-Sancho, J. & Izquierdo, M. (2003). Calcium influx through receptor-operated channel induces mitochondria-triggered paraptotic cell death. *J Biol Chem* **278**, 14134-45.

55. Jiang, D., Zhao, L., Clish, C. B. & Clapham, D. E. (2013). Letm1, the mitochondrial Ca2+/H+ antiporter, is essential for normal glucose metabolism and alters brain function in Wolf-Hirschhorn syndrome. *Proc Natl Acad Sci U S A* **110**, E2249-54.

56. Joiner, M. L., Koval, O. M., Li, J., He, B. J., Allamargot, C., Gao, Z., Luczak, E. D., Hall, D. D., Fink, B. D., Chen, B., Yang, J., Moore, S. A., Scholz, T. D., Strack, S., Mohler, P. J., Sivitz, W. I., Song, L. S. & Anderson, M. E. (2012). CaMKII determines mitochondrial stress responses in heart. *Nature* **491**, 269-73.

57. Juhaszova, M., Wang, S., Zorov, D. B., Nuss, H. B., Gleichmann, M., Mattson, M. P. & Sollott, S. J. (2008). The identity and regulation of the mitochondrial permeability transition pore: where the known meets the unknown. *Ann N Y Acad Sci* **1123**, 197-212.

58. Jung, D. W., Apel, L. & Brierley, G. P. (1990). Matrix free Mg2+ changes with metabolic state in isolated heart mitochondria. *Biochemistry* **29**, 4121-8.

59. Kamer, K. J. & Mootha, V. K. (2014). MICU1 and MICU2 play nonredundant roles in the regulation of the mitochondrial calcium uniporter. *EMBO Rep* **15**, 299-307.

60. Kamer, K. J., Sancak, Y. & Mootha, V. K. (2014). The uniporter: from newly identified parts to function. *Biochem Biophys Res Commun* **449**, 370-2.

61. Kolisek, M., Zsurka, G., Samaj, J., Weghuber, J., Schweyen, R. J. & Schweigel, M. (2003). Mrs2p is an essential component of the major electrophoretic Mg2+ influx system in mitochondria. *EMBO J* **22**, 1235-44.

62. Kovacs-Bogdan, E., Sancak, Y., Kamer, K. J., Plovanich, M., Jambhekar, A., Huber, R. J., Myre, M. A., Blower, M. D. & Mootha, V. K. (2014). Reconstitution of the mitochondrial calcium uniporter in yeast. *Proc Natl Acad Sci U S A* **111**, 8985-90.

63. Kraulis, P. J. (1991). Similarity of protein G and ubiquitin. *Science* **254**, 581-2.

64. Krogh, A., Larsson, B., von Heijne, G. & Sonnhammer, E. L. (2001). Predicting transmembrane protein topology with a hidden Markov model: application to complete genomes. *J Mol Biol* **305**, 567-80.

65. Lee, Y., Min, C. K., Kim, T. G., Song, H. K., Lim, Y., Kim, D., Shin, K., Kang, M., Kang, J. Y., Youn, H. S., Lee, J. G., An, J. Y., Park, K. R., Lim, J. J., Kim, J. H., Kim, J. H., Park, Z. Y., Kim, Y. S., Wang, J., Kim do, H. & Eom, S. H. (2015). Structure and function of the N-terminal domain of the human mitochondrial calcium uniporter. *EMBO Rep* **16**, 1318-33.

66. Lemasters, J. J., Theruvath, T. P., Zhong, Z. & Nieminen, A. L. (2009). Mitochondrial calcium and the permeability transition in cell death. *Biochim Biophys Acta* **1787**, 1395-401.

67. Lupas, A. (1997). Predicting coiled-coil regions in proteins. *Curr Opin Struct Biol* **7**, 388-93.

68. Lupas, A., Van Dyke, M. & Stock, J. (1991). Predicting coiled coils from protein sequences. *Science* **252**, 1162-4.

69. Mak, D. O., McBride, S. & Foskett, J. K. (1998). Inositol 1,4,5-trisphosphate [correction of tris-phosphate] activation of inositol trisphosphate [correction of tris-phosphate] receptor Ca2+ channel by ligand tuning of Ca2+ inhibition. *Proc Natl Acad Sci U S A* **95**, 15821-5.

70. Mallilankaraman, K., Cardenas, C., Doonan, P. J., Chandramoorthy, H. C., Irrinki, K. M., Golenar, T., Csordas, G., Madireddi, P., Yang, J., Muller, M., Miller, R., Kolesar, J. E., Molgo, J., Kaufman, B., Hajnoczky, G., Foskett, J. K. & Madesh, M. (2015). MCUR1 is an essential component of mitochondrial Ca(2+) uptake that regulates cellular metabolism. *Nat Cell Biol* **17**, 953.

71. Mallilankaraman, K., Doonan, P., Cardenas, C., Chandramoorthy, H. C., Muller, M., Miller, R., Hoffman, N. E., Gandhirajan, R. K., Molgo, J., Birnbaum, M. J., Rothberg, B. S., Mak, D. O., Foskett, J. K. & Madesh, M. (2012). MICU1 is an essential gatekeeper for MCU-mediated mitochondrial Ca(2+) uptake that regulates cell survival. *Cell* **151**, 630-44.

72. Marchi, S., Lupini, L., Patergnani, S., Rimessi, A., Missiroli, S., Bonora, M., Bononi, A., Corra, F., Giorgi, C., De Marchi, E., Poletti, F., Gafa, R., Lanza, G., Negrini, M., Rizzuto, R. & Pinton, P. (2013). Downregulation of the mitochondrial calcium uniporter by cancer-related miR-25. *Curr Biol* **23**, 58-63.

73. Marchi, S. & Pinton, P. (2014). The mitochondrial calcium uniporter complex: molecular components, structure and physiopathological implications. *J Physiol* **592**, 829-39.

74. Marsault, R., Murgia, M., Pozzan, T. & Rizzuto, R. (1997). Domains of high Ca2+ beneath the plasma membrane of living A7r5 cells. *EMBO J* **16**, 1575-81.

75. Martell, J. D., Deerinck, T. J., Sancak, Y., Poulos, T. L., Mootha, V. K., Sosinsky, G. E., Ellisman, M. H. & Ting, A. Y. (2012). Engineered ascorbate peroxidase as a genetically encoded reporter for electron microscopy. *Nat Biotechnol* **30**, 1143-8.

76. Matesanz-Isabel, J., Arias-Del-Val, J., Alvarez-Illera, P., Fonteriz, R. I., Montero, M. & Alvarez, J. (2016). Functional roles of MICU1 and MICU2 in mitochondrial Ca uptake. *Biochim Biophys Acta* **1858**, 1110-1117.

77. Meissner, G., Darling, E. & Eveleth, J. (1986). Kinetics of rapid Ca2+ release by sarcoplasmic reticulum. Effects of Ca2+, Mg2+, and adenine nucleotides. *Biochemistry* **25**, 236-44.

78. Meldolesi, J. & Pozzan, T. (1987). Pathways of Ca2+ influx at the plasma membrane: voltage-, receptor-, and second messenger-operated channels. *Exp Cell Res* **171**, 271-83.

79. Moreau, B., Nelson, C. & Parekh, A. B. (2006). Biphasic regulation of mitochondrial Ca2+ uptake by cytosolic Ca2+ concentration. *Curr Biol* **16**, 1672-7.

80. Murphy, E., Pan, X., Nguyen, T., Liu, J., Holmstrom, K. M. & Finkel, T. (2014). Unresolved questions from the analysis of mice lacking MCU expression. *Biochem Biophys Res Commun* **449**, 384-5.

81. Murzin, A. G., Brenner, S. E., Hubbard, T. & Chothia, C. (1995). SCOP: a structural classification of proteins database for the investigation of sequences and structures. *J Mol Biol* **247**, 536-40.

82. Nicholls, D. G. (1978). The regulation of extramitochondrial free calcium ion concentration by rat liver mitochondria. *Biochem J* **176**, 463-74.

83. Novgorodov, S. A., Gudz, T. I., Brierley, G. P. & Pfeiffer, D. R. (1994). Magnesium ion modulates the sensitivity of the mitochondrial permeability transition pore to cyclosporin A and ADP. *Arch Biochem Biophys* **311**, 219-28.

84. O'Neill, R., McCarthy, H. O., Cunningham, E., Montufar, E., Ginebra, M. P., Wilson, D. I., Lennon, A. & Dunne, N. (2016). Extent and mechanism of phase separation during the extrusion of calcium phosphate pastes. *J Mater Sci Mater Med* **27**, 29.

85. Oceandy, D., Stanley, P. J., Cartwright, E. J. & Neyses, L. (2007). The regulatory function of plasma-membrane Ca(2+)-ATPase (PMCA) in the heart. *Biochem Soc Trans* **35**, 927-30.

86. Oh-hora, M. & Rao, A. (2008). Calcium signaling in lymphocytes. *Curr Opin Immunol* **20**, 250-8.

87. Oxenoid, K., Dong, Y., Cao, C., Cui, T., Sancak, Y., Markhard, A. L., Grabarek, Z., Kong, L., Liu, Z., Ouyang, B., Cong, Y., Mootha, V. K. & Chou, J. J. (2016). Architecture of the mitochondrial calcium uniporter. *Nature* **533**, 269-73.

88. Pan, X., Liu, J., Nguyen, T., Liu, C., Sun, J., Teng, Y., Fergusson, M. M., Rovira, II, Allen, M., Springer, D. A., Aponte, A. M., Gucek, M., Balaban, R. S., Murphy, E. & Finkel, T. (2013). The physiological role of mitochondrial calcium revealed by mice lacking the mitochondrial calcium uniporter. *Nat Cell Biol* **15**, 1464-72.

89. Patron, M., Checchetto, V., Raffaello, A., Teardo, E., Vecellio Reane, D., Mantoan, M., Granatiero, V., Szabo, I., De Stefani, D. & Rizzuto, R. (2014). MICU1 and MICU2 finely tune the mitochondrial Ca2+ uniporter by exerting opposite effects on MCU activity. *Mol Cell* **53**, 726-37.

90. Patron, M., Raffaello, A., Granatiero, V., Tosatto, A., Merli, G., De Stefani, D., Wright, L., Pallafacchina, G., Terrin, A., Mammucari, C. & Rizzuto, R. (2013). The mitochondrial calcium uniporter (MCU): molecular identity and physiological roles. *J Biol Chem* **288**, 10750-8.

91. Paupe, V., Prudent, J., Dassa, E. P., Rendon, O. Z. & Shoubridge, E. A. (2015). CCDC90A (MCUR1) is a cytochrome c oxidase assembly factor and not a regulator of the mitochondrial calcium uniporter. *Cell Metab* **21**, 109-16.

92. Pendin, D., Greotti, E. & Pozzan, T. (2014). The elusive importance of being a mitochondrial Ca(2+) uniporter. *Cell Calcium* **55**, 139-45.

93. Perocchi, F., Gohil, V. M., Girgis, H. S., Bao, X. R., McCombs, J. E., Palmer, A. E. & Mootha, V. K. (2010). MICU1 encodes a mitochondrial EF hand protein required for Ca(2+) uptake. *Nature* **467**, 291-6.

94. Pinton, P., Ferrari, D., Rapizzi, E., Di Virgilio, F., Pozzan, T. & Rizzuto, R. (2001). The Ca2+ concentration of the endoplasmic reticulum is a key determinant of ceramide-induced apoptosis: significance for the molecular mechanism of Bcl-2 action. *EMBO J* **20**, 2690-701.

95. Pinton, P., Giorgi, C., Siviero, R., Zecchini, E. & Rizzuto, R. (2008). Calcium and apoptosis: ER-mitochondria Ca2+ transfer in the control of apoptosis. *Oncogene* **27**, 6407-18.

96. Plovanich, M., Bogorad, R. L., Sancak, Y., Kamer, K. J., Strittmatter, L., Li, A. A., Girgis, H. S., Kuchimanchi, S., De Groot, J., Speciner, L., Taneja, N., Oshea, J., Koteliansky, V. & Mootha, V. K. (2013). MICU2, a paralog of MICU1, resides within the mitochondrial uniporter complex to regulate calcium handling. *PLoS One* **8**, e55785.

97. Prentki, M., Janjic, D. & Wollheim, C. B. (1983). The regulation of extramitochondrial steady state free Ca2+ concentration by rat insulinoma mitochondria. *J Biol Chem* **258**, 7597-602.

98. Preston, G. W. & Phillips, D. H. (2016). Quantification of a peptide standard using the intrinsic fluorescence of tyrosine. *Anal Bioanal Chem* **408**, 2187-93.

99. Raffaello, A., De Stefani, D. & Rizzuto, R. (2012). The mitochondrial Ca(2+) uniporter. *Cell Calcium* **52**, 16-21.

100. Raffaello, A., De Stefani, D., Sabbadin, D., Teardo, E., Merli, G., Picard, A., Checchetto, V., Moro, S., Szabo, I. & Rizzuto, R. (2013). The mitochondrial calcium uniporter is a multimer that can include a dominant-negative pore-forming subunit. *EMBO J* **32**, 2362-76.

101. Rissato, S. R., Galhiane, M. S., Souza, A. G. d. & Apon, B. M. (2005). Development of a Supercritical Fluid Extraction method for simultaneous determination of organophosphorus, organohalogen, organonitrogen and pyretroids pesticides in fruit and vegetables and its comparison with a conventional method by GC-ECD and GC-MS. *Journal of the Brazilian Chemical Society* **16**, 1038-1047.

102. Rizzuto, R., Brini, M., Murgia, M. & Pozzan, T. (1993). Microdomains with high Ca2+ close to IP3-sensitive channels that are sensed by neighboring mitochondria. *Science* **262**, 744-7.

103. Rizzuto, R., De Stefani, D., Raffaello, A. & Mammucari, C. (2012). Mitochondria as sensors and regulators of calcium signalling. *Nat Rev Mol Cell Biol* **13**, 566-78.

104. Rizzuto, R., Marchi, S., Bonora, M., Aguiari, P., Bononi, A., De Stefani, D., Giorgi, C., Leo, S., Rimessi, A., Siviero, R., Zecchini, E. & Pinton, P. (2009). Ca(2+) transfer from the ER to mitochondria: when, how and why. *Biochim Biophys Acta* **1787**, 1342-51.

105. Roderick, H. L. & Cook, S. J. (2008). Ca2+ signalling checkpoints in cancer: remodelling Ca2+ for cancer cell proliferation and survival. *Nat Rev Cancer* **8**, 361-75.

106. Romani, A., Marfella, C. & Scarpa, A. (1993). Cell magnesium transport and homeostasis: role of intracellular compartments. *Miner Electrolyte Metab* **19**, 282-9.

107. Rossi, C. S. & Lehninger, A. L. (1964). Stoichiometry of Respiratory Stimulation, Accumulation of Ca++ and Phosphate, and Oxidative Phosphorylation in Rat Liver Mitochondria. *J Biol Chem* **239**, 3971-80.

108. Rudolf, R., Mongillo, M., Magalhaes, P. J. & Pozzan, T. (2004). In vivo monitoring of Ca(2+) uptake into mitochondria of mouse skeletal muscle during contraction. *J Cell Biol* **166**, 527-36.

109. Rutter, G. A., Osbaldeston, N. J., McCormack, J. G. & Denton, R. M. (1990). Measurement of matrix free Mg2+ concentration in rat heart mitochondria by using entrapped fluorescent probes. *Biochem J* **271**, 627-34.

110. Sancak, Y., Markhard, A. L., Kitami, T., Kovacs-Bogdan, E., Kamer, K. J., Udeshi, N. D., Carr, S. A., Chaudhuri, D., Clapham, D. E., Li, A. A., Calvo, S. E., Goldberger, O. & Mootha, V. K. (2013). EMRE is an essential component of the mitochondrial calcium uniporter complex. *Science* **342**, 1379-82.

111. Saris, N. E. & Carafoli, E. (2005). A historical review of cellular calcium handling, with emphasis on mitochondria. *Biochemistry (Mosc)* **70**, 187-94.

112. Saris, N. E., Mervaala, E., Karppanen, H., Khawaja, J. A. & Lewenstam, A. (2000). Magnesium. An update on physiological, clinical and analytical aspects. *Clin Chim Acta* **294**, 1-26.

113. Schindl, R., Weghuber, J., Romanin, C. & Schweyen, R. J. (2007). Mrs2p forms a high conductance Mg2+ selective channel in mitochondria. *Biophys J* **93**, 3872-83.

114. Settimo, L., Donnini, S., Juffer, A. H., Woody, R. W. & Marin, O. (2007). Conformational changes upon calcium binding and phosphorylation in a synthetic fragment of calmodulin. *Biopolymers* **88**, 373-85.

115. Sievers, F. & Higgins, D. G. (2014). Clustal omega. *Curr Protoc Bioinformatics* **48**, 3 13 1-16.

116. Simon, S. M. & Llinas, R. R. (1985). Compartmentalization of the submembrane calcium activity during calcium influx and its significance in transmitter release. *Biophys J* **48**, 485-98.

117. Sonnhammer, E. L., von Heijne, G. & Krogh, A. (1998). A hidden Markov model for predicting transmembrane helices in protein sequences. *Proc Int Conf Intell Syst Mol Biol* **6**, 175-82.

118. Szanda, G., Rajki, A., Gallego-Sandin, S., Garcia-Sancho, J. & Spat, A. (2009). Effect of cytosolic Mg2+ on mitochondrial Ca2+ signaling. *Pflugers Arch* **457**, 941-54.

119. Tadross, M. R., Tsien, R. W. & Yue, D. T. (2013). Ca2+ channel nanodomains boost local Ca2+ amplitude. *Proc Natl Acad Sci U S A* **110**, 15794-9.

120. Territo, P. R., Mootha, V. K., French, S. A. & Balaban, R. S. (2000). Ca(2+) activation of heart mitochondrial oxidative phosphorylation: role of the F(0)/F(1)-ATPase. *Am J Physiol Cell Physiol* **278**, C423-35.

121. Tomar, D., Dong, Z., Shanmughapriya, S., Koch, D. A., Thomas, T., Hoffman, N. E., Timbalia, S. A., Goldman, S. J., Breves, S. L., Corbally, D. P., Nemani, N., Fairweather, J. P., Cutri, A. R., Zhang, X., Song, J., Jana, F., Huang, J., Barrero, C., Rabinowitz, J. P., Luongo, T. S., Schumacher, S. M., Rockman, M. E., Dietrich, A., Merali, S., Caplan, J., Stathopulos, P. B., Ahima, R. S., Cheung, J. Y., Houser, S. R., Koch, W. J., Patel, V., Gohil, V. M., Elrod, J. W., Rajan, S. & Madesh, M. (2016). MCUR1 is a scaffold factor for the MCU complex function and promotes mitochondrial bioenergetics. *Cell Rep* **[In Press]**.

122. Tsai, M. F., Phillips, C. B., Ranaghan, M., Tsai, C. W., Wu, Y., Willliams, C. & Miller, C. (2016). Dual functions of a small regulatory subunit in the mitochondrial calcium uniporter complex. *Elife* **5**.

123. Vais, H., Mallilankaraman, K., Mak, D. O., Hoff, H., Payne, R., Tanis, J. E. & Foskett, J. K. (2016). EMRE Is a Matrix Ca(2+) Sensor that Governs Gatekeeping of the Mitochondrial Ca(2+) Uniporter. *Cell Rep* **14**, 403-10.

124. van Loon, E. P., Little, R., Prehar, S., Bindels, R. J., Cartwright, E. J. & Hoenderop, J. G. (2016). Calcium Extrusion Pump PMCA4: A New Player in Renal Calcium Handling? *PLoS One* **11**, e0153483.

125. Wang, L., Yang, X., Li, S., Wang, Z., Liu, Y., Feng, J., Zhu, Y. & Shen, Y. (2014). Structural and mechanistic insights into MICU1 regulation of mitochondrial calcium uptake. *EMBO J* **33**, 594-604.

126. Wolwer, C. B., Pase, L. B., Russell, S. M. & Humbert, P. O. (2016). Calcium Signaling Is Required for Erythroid Enucleation. *PLoS One* **11**, e0146201.

127. Yamamoto, T., Yamagoshi, R., Harada, K., Kawano, M., Minami, N., Ido, Y., Kuwahara, K., Fujita, A., Ozono, M., Watanabe, A., Yamada, A., Terada, H. & Shinohara, Y. (2016). Analysis of the structure and function of EMRE in a yeast expression system. *Biochim Biophys Acta* **1857**, 831-839.

128. Yu, S. P. & Choi, D. W. (1997). Na(+)-Ca2+ exchange currents in cortical neurons: concomitant forward and reverse operation and effect of glutamate. *Eur J Neurosci* **9**, 1273-81.

129. Yurdakok-Dikmen, B., Kuzukiran, O., Filazi, A. & Kara, E. (2016). Measurement of selected polychlorinated biphenyls (PCBs) in water via ultrasound assisted emulsification-microextraction (USAEME) using low-density organic solvents. *J Water Health* **14**, 214-22.

130. Zoratti, M. & Szabo, I. (1995). The mitochondrial permeability transition. *Biochim Biophys Acta* **1241**, 139-76.

131. Zorov, D. B., Juhaszova, M. & Sollott, S. J. (2014). Mitochondrial reactive oxygen species (ROS) and ROS-induced ROS release. *Physiol Rev* **94**, 909-50.

132. Zsurka, G., Gregan, J. & Schweyen, R. J. (2001). The human mitochondrial Mrs2 protein functionally substitutes for its yeast homologue, a candidate magnesium transporter. *Genomics* **72**, 158-68.

133. Zweifach, A. & Lewis, R. S. (1995). Rapid inactivation of depletion-activated calcium current (ICRAC) due to local calcium feedback. *J Gen Physiol* **105**, 209-26.

Appendices

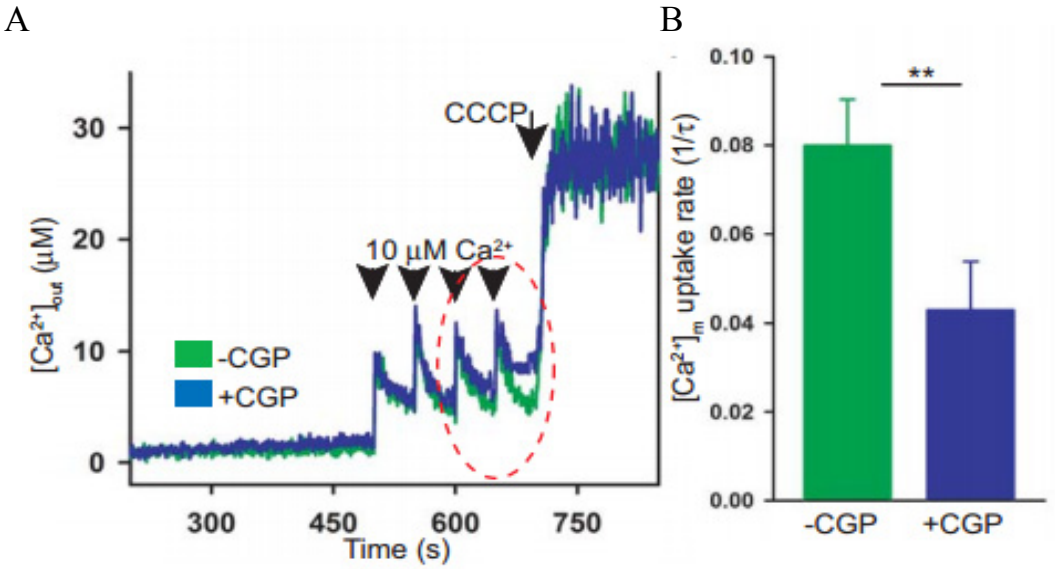

Appendix Figure 1. Ca^{2+}-dependent MCU inactivation in live cells. Digitonin-permeabilized HEK293T cells bathed in intracellular-like solution containing thapsigargin were loaded with the Ca^{2+} indicator dye Fura2FF (1µM), to which pulses of 10 µM extracellular Ca^{2+} were delivered before the addition of the mitochondrial uncoupler CCCP (2 µM) (arrowheads). Changes in bath Ca^{2+} (Ca^{2+}_{out}) were measured in the absence and presence of the NCLX blocker, CGP37157 (10 µM). **(A)** Representative traces of $[Ca^{2+}]_{out}$ from three independent experiments. **(B)** Quantification of $[Ca^{2+}]_m$ uptake rate taken from the reduction in bath Ca^{2+} after 30 µM $[Ca^{2+}]_{out}$ addition. Error bars represent SEM. **P<0.01.

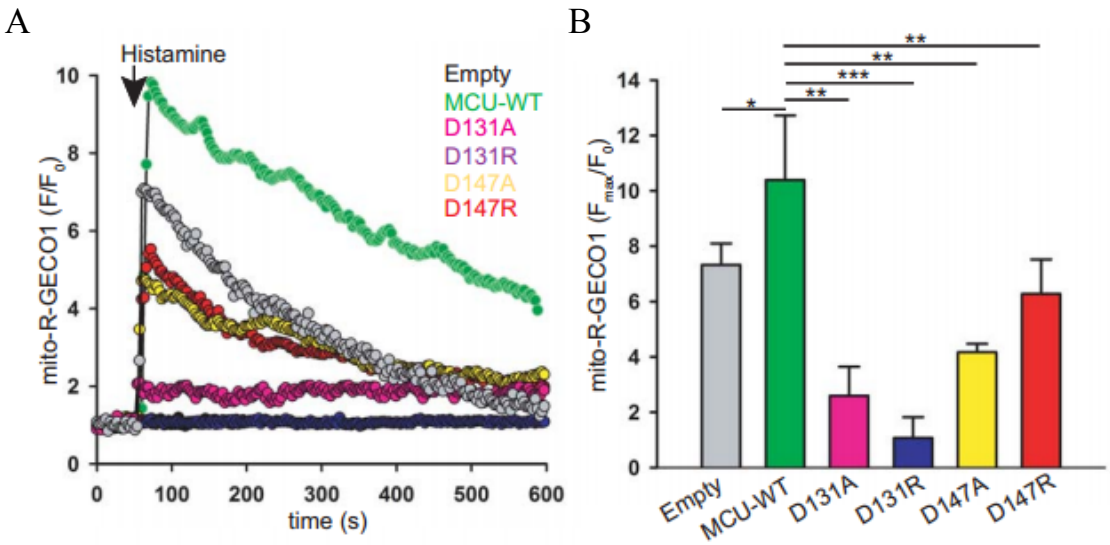

Appendix Figure 2. Live cell MCU functional activity. HeLa cells were transiently transfected with genetically encoded Ca^{2+} sensors (mito-R-GECO1 or cytosolic-R-GECO1), which are mitochondrial and cytosolic Ca^{2+} indicators, respectively, along with empty vector, MCU-WT-GFP, MCU D131A-GFP, MCU D131R-GFP, MCU D147A-GFP, or MCU D147R-GFP. HeLa cells were stimulated with 100 μM histamine after one minute baseline recording. **(A)** Representative mean traces of mito-R-GECO1 fluorescence (f.a.u.) in HeLa cells transfected with empty vector (grey), MCU-WT-GFP (green), MCU D131A-GFP (pink), MCU D131R-GFP (blue), MCU D147A-GFP (yellow), and MCU D147R-GFP (red). **(B)** Quantification of peak mito-R-GECO1 fluorescence (F_{max}/F_0) (mean ± s.e.m). *P <0.05; **P <0.01; ***P <0.001.

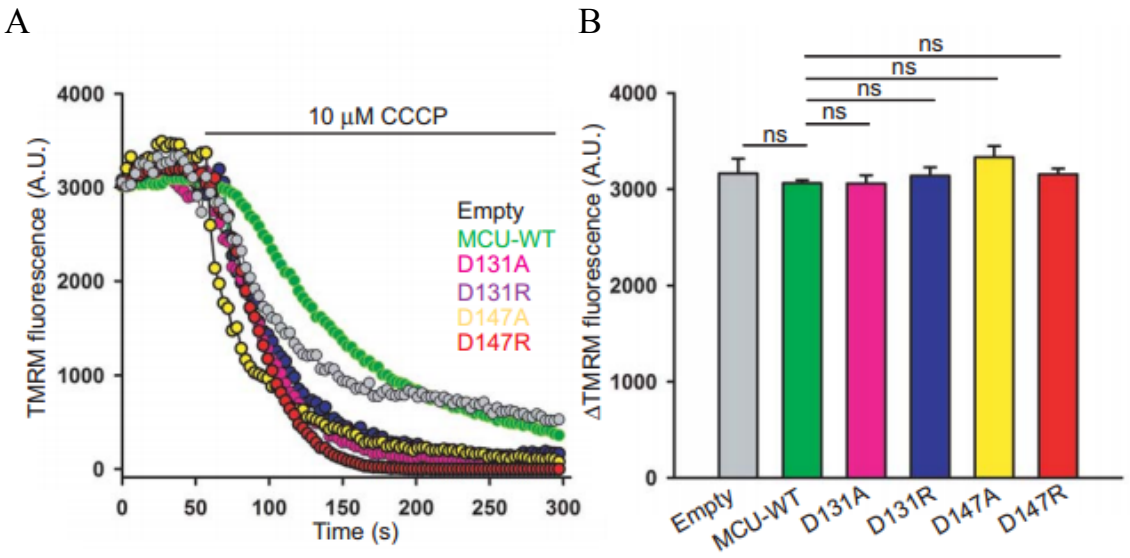

Appendix Figure 3. Mitochondrial membrane potential of HeLa cells. HeLa cells were transiently transfected with genetically encoded Ca^{2+} sensors (mito-R-GECO1 or cytosolic-R-GECO1), which are mitochondrial and cytosolic Ca^{2+} indicators, respectively, along with empty vector, MCU-WT-GFP, MCU D131A-GFP, MCU D131R-GFP, MCU D147A-GFP, or MCU D147R-GFP. **(A)** HeLa cells were stimulated with 100 μM histamine after one minute baseline recording. 48 hours post-transfection, cells were loaded with the mitochondrial membrane potential (DYm) indicator TMRM (50 nM). After baseline recording, the mitochondrial uncoupler CCCP (10 μM) was added. **(B)** Quantification of TMRM fluorescence. (mean ± s.e.m). ns, not significant.

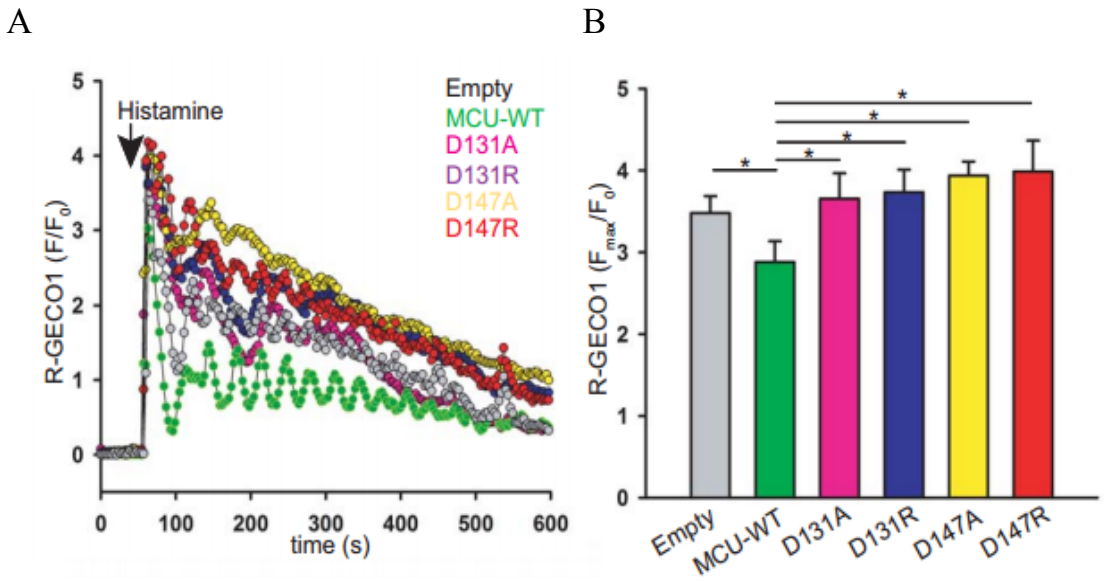

Appendix Figure 4. Live cell MCU functional activity. HeLa cells were transiently transfected with genetically encoded Ca^{2+} sensors (mito-R-GECO1 or cytosolic-R-GECO1), which are mitochondrial and cytosolic Ca^{2+} indicators, respectively, along with empty vector, MCU-WT-GFP, MCU D131A-GFP, MCU D131R-GFP, MCU D147A-GFP, or MCU D147R-GFP. HeLa cells were stimulated with 100 μM histamine after one minute baseline recording. **(A)** Representative mean traces of cytosolic-R-GECO1 fluorescence (f.a.u) in HeLa cells transfected with empty vector (grey), MCU-WT-GFP (green), MCU D131A-GFP (pink), MCU D131R-GFP (blue), MCU D147A-GFP (yellow), and MCU D147R-GFP (red). **(B)** Quantification of cytosolic Ca^{2+} elevation as a function of R-GECO1 fluorescence (F-F0/F0) (mean ± s.e.m). *P <0.05.

Curriculum Vitae

Name: Samuel K. Lee

Post-Secondary Education and Degrees:

Western University
London, Ontario, Canada
Honors Specialization BMSc
2010-2014

Western University
London, Ontario, Canada
MSc- Physiology & Pharmacology
2014-2016

Honors and Awards:

Dean's Honor List
2011-2014

Western Graduate Research Scholarship
2014-2016

Related Work Experience:

Reseach Assistant
2013-2014
Western University

Laboratory Course Assistant
Scientific Method of Biology- 2290F/G
2013-2014
Western University

Teaching Assistant
Physiology 2130
2014-2016
Western University

Publications:

Lee, S.K., Shanmughapriya, S., Mok, M., Dong, Z., Rajan, S., Junop, M.., Muniswamy, M. & Stathopulos, P. (2016). The mitochondrial calcium uniporter is autoregulated by cation binding to the β-grasp-like matrix domain. *Cell Chem Biol.* (In review)

Presentations:

Cardiovascular Journal Club Presentation
Mechanisms behind mitochondrial calcium uniporter function and regulation
2015
Western University

Gowdey Research Day Posted Presentation
Lee, S.K., Mok, M., Junop, M. & Stathopulos, P. 2015. Beta-grasp-like domain structure of the human mitochondrial calcium uniporter (MCU) and its regulation by Ca^{2+} and Mg^{2+}. Western University, London, ON.